

Characterization Tools to Probe Degradation Mechanisms in Organic and Perovskite Solar Cells

Souk Y. Kim, Cyril C. F. Kumachang, and Nutifafa Y. Doumon*

Organic solar cells (OSCs) and perovskite solar cells (PSCs) are promising due to their low cost and potential for renewable solar energy conversion. They are compatible with many substrates and varied deposition techniques, including solution processing. They can be coupled with other solar cell types in tandem and multijunction structures. Despite these great attributes and advancements in power conversion efficiencies over the years, they suffer from severe degradation, leading to low lifetime. In terms of research, their stability studies lag. One reason is the complexity of degradation studies and, sometimes, the lack of adequate tools to do an in-depth probe. Another reason is the lack of comprehensive literature on metrologies' appropriateness for this kind of study. Although there are reviews on stability and improvement in the efficiency of devices, they focus either on the degradation mechanisms or efforts to use specific tools. There is little on comprehensive characterization tools for their degradation studies. Herein, the experimental tools and techniques researchers use in general to probe degradation in OSCs and PSCs are studied. This review is intended as a starting point and a go-to material for current and future researchers and (under-)graduate students interested in stability studies.

1. Introduction

As energy demands increase, renewable and sustainable energy has become a hot research topic in recent decades. Among other emerging technologies, photovoltaics (PV) is considered the

S. Y. Kim, C. C. F. Kumachang, N. Y. Doumon
 Department of Materials Science and Engineering
 The Pennsylvania State University
 University Park, PA 16802, USA
 E-mail: nzd5349@psu.edu

N. Y. Doumon
 Materials Research Institute
 The Pennsylvania State University
 University Park, PA 16802, USA

N. Y. Doumon
 Alliance for Education, Science, Engineering, and Design with Africa
 The Pennsylvania State University
 University Park, PA 16802, USA

 The ORCID identification number(s) for the author(s) of this article can be found under <https://doi.org/10.1002/solr.202300155>.

© 2023 The Authors. Solar RRL published by Wiley-VCH GmbH. This is an open access article under the terms of the Creative Commons Attribution-NonCommercial License, which permits use, distribution and reproduction in any medium, provided the original work is properly cited and is not used for commercial purposes.

DOI: [10.1002/solr.202300155](https://doi.org/10.1002/solr.202300155)

most promising due to the abundance of its energy resources. Organic and perovskite PVs, in particular, have garnered attention as they possess inherent advantages, such as low cost, lightweight, solution processing at low temperatures,^[1,2] and great potential for roll-to-roll manufacturing on flexible substrates.^[3–6] The power conversion efficiency (PCE) of organic and perovskite solar cells (OSCs and PSCs) have reached over 20% and 25%, respectively, at the laboratory level.^[7–9]

OSCs were first developed in 1986 when Tang et al.^[10] demonstrated that an electron donor and acceptor bilayer could produce a photocurrent as a photoactive layer. The first major breakthrough of OSCs featuring the bulk heterojunction (BHJ) structure was a blend of donor and acceptor materials by Heeger et al. in 1995.^[11,12] The second breakthrough began with nonfullerene acceptors as alternatives to improve the limited absorption properties, energy level tunability, and photochemical instability associated with earlier used fullerene derivative acceptors.^[13,14] Due to their better light absorption properties, appropriate molecular tailoring, and easily tunable energy levels with higher open-circuit voltages, this has resulted in a remarkable increase in the efficiencies of single-junction OSCs to nearly 20%. Aside from the advent of new materials, the development of device architecture, such as ternary and tandem solar cells, has considerably contributed to PCE enhancement. A ternary solar cell is a single junction active layer with three different materials for a wide absorption range. It has attracted great interest due to its simple device design without needing multiple-stacked interfacial layers.^[15–18] However, a tandem device has two stacked sub-devices with two active layers absorbing different wavelengths with enhanced voltage and/or current. For instance, the double absorption layers in tandem OSCs enabled higher efficiency of over 20%.^[8,19,20] It serves as a base for developing multijunction devices toward higher efficiency, which is challenging due to the possible interfacial defects from additional interfacial layers.

In contrast to OSCs, PSCs were only introduced slightly over a decade ago. Although Gustav Rose discovered perovskite in 1839, it was only in 2009 that Kojima et al.^[21] reported PSC as a laboratory-scale n-type photovoltaic with nanocrystalline particles self-organized on TiO₂, achieving a PCE of 3.8%. This work heralded the beginning of a new era of photovoltaics based on metal halide perovskite materials. In a follow-up research, Kim et al.^[22] reported a new solid-state mesoscopic solar cell

using spiro-OMeTAD as a hole-transporting layer to address the minute scale lifetime with liquid electrolyte, achieving a PCE of 9.7% in 2012. Later, Grätzel et al.^[23] introduced triple cations mixed halide perovskite with Cs/MA/FA cation to achieve high efficiency of 21.1%. Based on these breakthrough studies, numerous studies have been carried out over the decade toward higher efficiency, producing a smooth film using various deposition methods and chemical compositions^[9,24,25] and reducing interfacial defects and recombination, which enhance charge extraction and transport.^[24,25] This tremendous research rapidly increased the PCE to over 25%.^[26] Furthermore, research on tandem PSCs is currently very active due to the possibility of various device configurations, such as perovskites/perovskite, perovskite/organic, perovskite/CIGS, and perovskite/silicon, leading to PCEs of over 33% for perovskite tandem devices.^[19,27–31]

While the efficiency of OSCs and PSCs has improved a lot, cost and stability remain the challenges to be considered. The degradation mechanism study of both OSCs and PSCs is interesting to understand the stability behavior in both solar cells as they are susceptible to air, change at modest temperatures, and have relatively weak bonds. In addition, most perovskite solar cells contain organic semiconductor contact layers.^[32,33] They are thus susceptible to some additional organic material-specific degradation observed in OSCs. The change in the physical and chemical properties of OSCs and PSCs, which often decrease their performance over time, is called degradation. Degradation usually affects important device parameters such as the short circuit current (J_{sc}), open circuit voltage (V_{oc}), and fill factor (FF); thus, it affects PCE negatively.^[34] Although stability in OSCs and PSCs has received relative attention recently, the reported studies differed from lab to lab. To provide consistency and repeatability in the stability assessment and reporting procedures, researchers established standard aging protocols first for OSCs at the International Summit on Organic PV Stability (ISOS) in 2010^[35] and then for PSCs in 2020.^[36] This 2020 protocol is a necessary expansion on the 2010 protocol with a series of testing methods due to the unique characteristics of PSCs, such as examining intrinsic stability and light-dark cycling that mimics the diurnal cycle. However, despite these considerable efforts of researchers, there is still a huge gap between focus studies on PCE and stability. The relatively low stability of these technologies is one of the main barriers to their future commercialization.^[37–39]

OSCs can suffer from mechanical, electrical, light, temperature, oxygen, and moisture-induced degradation. The degradation at the active layer of OSCs is highly favored by oxygen and light jointly in what is known as photo-oxidation.^[40] The studies have proven that the workhorse acceptor material, [6,6]-phenyl-C₆₁-butyric acid methyl ester (PCBM) reacts with oxygen in the presence of light to produce oxidized PCBM with a lower LUMO level that results in induced traps in the active layer.^[41] Another major part of OSCs where degradation takes place is at the electrodes. The electrodes are greatly responsible for the stability and performance of OSCs since their work function provides optimal charge extraction and the built-in potential of the device. Metals such as aluminum and silver are often used as electrodes in OSCs due to their high conductivity. Unfortunately, they are highly reactive with oxygen and water, producing oxidized layers and barriers that hinder the charge selectivity of the electrodes, thereby reducing the FF and

PCE of OSCs.^[42,43] Perovskite and PSCs suffer similarly from intrinsic and extrinsic stability issues.^[44] The main inherent stability challenges in perovskites and PSCs are band structure, defects, thermodynamic, and phase stabilities. They are also prone to moisture, heat, light, and oxygen stressors.^[44,45] The studies have shown that perovskites and PSCs are intrinsically more stable than other solar cells.^[44] For ABX₃ perovskites, the Goldschmidt tolerance factor, t , given by Equation (1) and later modified by Bartel et al., as shown in Equation (2), is used to predict their structural stability.^[46,47]

$$t = \frac{R_A + R_X}{\sqrt{2}(R_X + R_B)} \quad (1)$$

$$\tau = \frac{R_X}{R_B} - n_A \left(n_A - \frac{\frac{R_A}{R_B}}{\ln\left(\frac{R_A}{R_B}\right)} \right) \quad (2)$$

where R_A , R_B , and R_X are the ionic radii of A, B, and X species of the perovskite crystal structure, respectively, and n_A is the oxidation state of the cation of the species A. According to Goldschmidt, a perovskite will assume a hexagonal or tetragonal structure when $t > 1$, a cubic structure when $0.9 < t < 1$, and an orthorhombic or rhombohedral structure when $0.71 < t < 0.9$. For $t < 0.71$, no perovskite crystal structure is formed.^[44,48,49] Thermodynamically, annealing perovskites at elevated temperatures will crystallize their structure because of the departure from the required tolerance factor due to changes in the ionic radii of the different species.^[50–52] As such, perovskites have serious thermodynamic phase stability problems at elevated temperatures due to defects in their films brought about by annealing at such temperatures.^[49,53] Of the extrinsic factors mentioned earlier, moisture has the highest effect on the performance of PSCs, followed by heat and light.^[44,54] The studies showed that while a small amount of moisture in perovskite films during fabrication improves its quality and favors the formation of larger grain sizes with fewer grain boundaries, exposure to moisture and high relative humidity (RH) for extended periods leads to changes in the perovskite lattice.^[55–66] Considering that OSCs and PSCs operate in direct sunlight with an average temperature^[67] and extremes of about -40°C and $+85^{\circ}\text{C}$ on certain days, durable thermal stability, especially for PSCs, is essential to ensure that they meet the International Electrochemical Commission (IEC 61 215) benchmark.^[68] Degradation in OSCs and PSCs is highly undesirable due to the performance loss of these devices and associated negative environmental impact and health challenges, especially in PSCs with lead (Pb) toxicity. For these and other reasons, degradation studies in these devices have increased within the last decade. Our efforts in this review focus on tools and techniques to study the degradation mechanism in the active layer materials (solution and thin film), parts of, and the whole photovoltaic devices.

Various experimental techniques are used to study the degradation in OSCs and PSCs. These include but are not limited to spectroscopy such as ultraviolet (UV) photoelectron spectroscopy (UPS), Fourier-transform infrared (FTIR) spectroscopy, UV-vis-NIR spectroscopy, etc.; microscopy such as scanning electron microscopy (SEM), high-resolution transmission electron microscopy (HRTEM), atomic force microscopy (AFM), etc.; X-ray characterization such as grazing-incidence wide-angle

X-ray scattering (GIWAXS), nuclear magnetic resonance (NMR), thermogravimetric analysis (TGA), and other methods such as surface analysis, etc.^[53,63–66,69–75] This review focuses on most of these experimental tools and techniques researchers can and have generally explored to probe degradation in OSCs and PSCs. There are many reviews on the stability of these technologies.^[44,76–80] For instance, in perovskite solar cells, the focus is either on the degradation mechanisms or efforts in using specific tools to characterize them,^[81–91] as highlighted by Fenning et al.^[92] in this editorial. However, little can be said about a one-spot comprehensive review of the tools used to monitor and probe OSC and PSC degradation. They have been highlighted sporadically through many studies. A recent review of tools for researching degradation, authored by Meng et al.,^[93] focused mainly on *in situ* experiments on perovskite. Our review is intended as a starting point and go-to material for current and future researchers and (post-)graduate students interested in the stability study of new-generation photovoltaic technologies, especially OSCs and PSCs. It provides a comprehensive summary and discussion on the main characterization tools to monitor and probe degradation mechanisms in general.

2. Standard Degradation Characterization Tools

As the degradation mechanism in these new technologies is a complex phenomenon to study, the metrology to probe the phenomenon keeps evolving. This is partially due to introducing new active layer and/or transport layer materials over the years and to changes in device structures. While this section focuses on standard or *ex situ* characterization tools concerning degradation, Section 3 briefly examines *in situ* characterization tools to probe the same phenomenon. A complete discussion on *in situ* characterization tools is offered by Meng et al.^[93]

2.1. Photosensitive Materials

The tools described in this section are mostly used in degradation studies to monitor changes in thin film and solution of the active layer materials of either OSCs or PSCs. In some cases, they are used to probe interfacial phenomena due to degradation or reaction between some layers of the complete device stack. These instances are also highlighted.

2.1.1. Ultraviolet–Visible–Near Infrared (UV–Vis–NIR) Spectroscopy

UV–vis–NIR spectroscopy is a tool used to measure the absorption, reflection, and transmission spectra of materials. It is one of the fundamental and essential tools used in nearly every field working with light.^[94–96] Thus, it is commonly used to probe the degradation of materials in solution, thin film, or device stack by detecting changes in absorption intensity and peaks induced by degradation agents. When photobleaching or thermal-bleaching in OSC and PSC materials or layers occurs, it can mainly be seen via UV–vis–NIR absorption spectroscopy. For instance, the influence of polyethyleneimine (PEI, an electron transport layer (ETL) on ZnO in inverted OSCs was investigated under shelf and operational conditions by Li et al.^[97] using

UV–vis–NIR spectroscopy. The time evolution of the UV–vis–NIR spectra of Y6 films on various ETLs films, ZnO, PEI, and ZnO:PEI, was measured in a N₂-filled glove box under continuous illumination. Figure 1a depicts the time-evolved absorbance of the Y6 component on ZnO, which steadily diminishes under illumination. Similarly, the absorbance of PEI/Y6 and ZnO:PEI/Y6 is observed. The decay rate of absorption of each film can be calculated. The absorbance peak at \approx 800 nm of the ZnO/Y6 film showed a noticeable decrease of around 56% after 325 h. However, the decay of absorbance of Y6 under air conditions without illumination was negligible for 250 h, as shown in Figure 1b.

Also, Shi et al.^[98] used UV–vis–NIR spectroscopy to investigate the photostability of synthesized Y6 as a function of molecular weight and polydispersity in ambient conditions under 100 mW cm^{−2} illumination for 360 h. Photobleaching of the Y6 materials occurred after a few hours in ambient conditions with drastic change in spectra at higher hours, in contrast to the Y6 results in N₂-filled conditions in Figure 1b and especially in air in Figure 1b insert. Although the difference in absorption of the synthesized Y6 under illumination reveals significant variation compared to the commercial materials, it is not adequately explained in the study. This indicates that the synthesis process as functions of molecular weight and polydispersity can cause a substantial change in the properties of polymers with respect to photobleaching.

UV–vis–NIR spectroscopy is also used to monitor glass transition temperature (T_g) by Qin et al.,^[99] as shown in Figure 1d. The mechanical or thermal stability of BTP(or Y6 family)-based materials was estimated for establishing relations between molecular structure and glass transition temperature T_g . The T_g of NFAs is an important factor in determining the thermal stability of OSCs since the annealing temperature is strongly related to the T_g of the materials. Notably, Zhu et al.^[100] employed *in situ* UV–vis–NIR absorption spectroscopy for the first time to monitor the morphological evolution under deformation in ternary active material films in OSCs to accurately demonstrate the impact of strengthened molecular interaction on stabilizing morphology against deformation. Figure 1e exhibits the loss in absorption intensity of the films due to their decreased thickness during stretching.

UV–vis–NIR spectroscopy has also been used to monitor degradation in perovskite active films and devices, like OSCs.^[101–104] Lanzetta et al.^[105] studied the degradation in ASnI₃ perovskites (with A = 20% phenylethylammonium + 80% formamidinium) in ambient using experimental tools such as spectroscopy and diffraction, combined with ab initio simulation techniques. Figure 1f shows a contour graph indicating the normalized *in situ* absorbance as a function of time and wavelength. It shows a decrease in absorbance, particularly between 660 and 870 nm, close to the two primary optical transitions permitted in these materials. Also, Hang et al.^[102] investigated burn-in stability of PSCs under light soaking and proposed that a small amount of the small molecule bathophenanthroline (Bphen) into [6,6]-phenyl-C61-butyric acid methyl ester (PCBM) can stabilize the C₆₀-cage and improve the stability at the interface of perovskite/SnO₂ ETL. Thus, the absorption of PCBM and PCBM:Bphen films are measured under UV aging. At around 330 nm, the absorption of PCBM was enhanced and blue-shifted

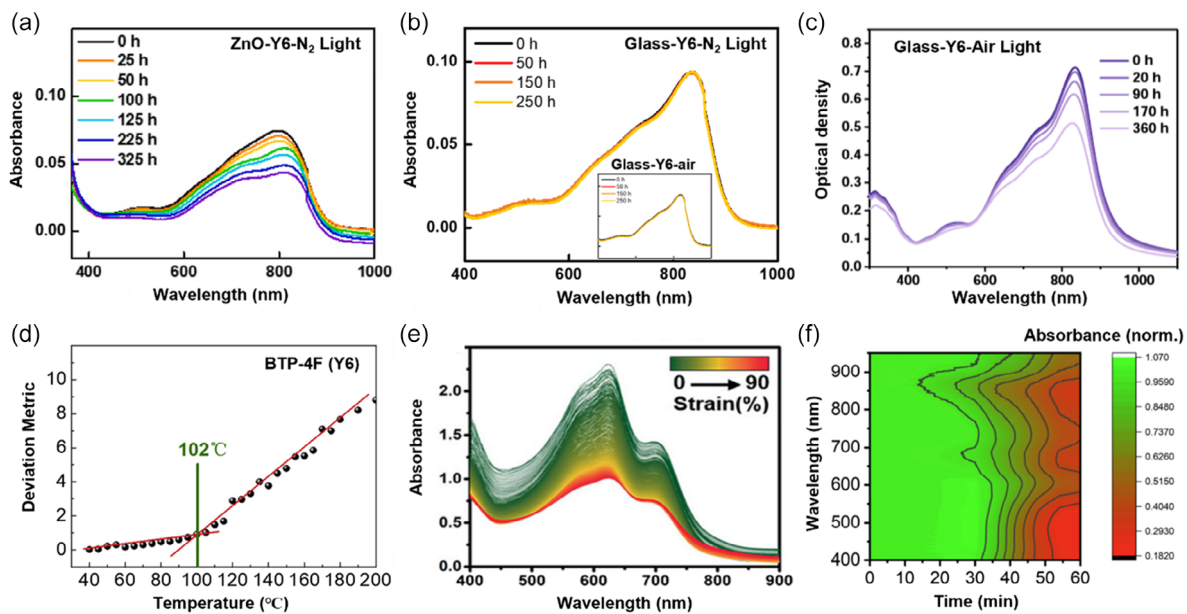


Figure 1. The UV-vis–NIR absorption spectra of a) ZnO/Y6 film in a N₂-filled environment, b) Y6 films in a N₂-filled and air condition under illumination. Reproduced with permission.^[97] Copyright 2021, Elsevier Inc. c) Y6 in air condition under illumination. Reproduced with permission.^[98] Copyright 2020, Wiley-VCH. d) The UV-vis–NIR deviation metric results of Y6. Reproduced with permission.^[99] Copyright 2021, Elsevier Inc. e) In situ UV-vis–NIR absorption spectrum of PBDB-T:PCE10:N2200 during stretching. Reproduced with permission.^[100] Copyright 2021, Wiley-VCH. f) Contour graphs of normalized absorbance of (PEA)_{0.2}(FA)_{0.8}SnI₃. Reproduced with permission.^[105] Copyright 2021, Springer Nature.

after UV illumination for 120 min, while that of PCBM:Bphen film remained unchanged even after UV illumination. Such a result indicates that choice of active layer materials for optimum stability may not be sufficient, and thus, interfacial materials may be crucial to the stability of devices as well.

One cannot underestimate the importance of UV-vis–NIR spectroscopy as a crucial primary, easy-to-use, inexpensive analytical technique to sensitively pinpoint the optical changes caused by degradation in OSCs or PSCs. It is a nondestructive technique that can be used without altering material properties. It covers a wide wavelength range, helping to ascertain early degradation detection due to (photo- or thermal) bleaching and studying the underlying mechanisms. Furthermore, it can be used to probe OSC or PSC pristine or blend materials degradation in solution, helping to determine whether the precursor materials have already undergone degradation in solution before thin film fabrication. For instance, Chen et al.^[106] probed iodine reduction for reproducible and high-performance perovskite solar cells and modules with UV-vis–NIR spectroscopy in the perovskite precursor solution. Introducing benzylhydrazine hydrochloride into degraded precursor solutions as a reducing agent makes it possible to significantly decrease the concentration of harmful I₂ and convert it into I[−], which in turn leads to a substantial reduction in the charge traps induced by I₃[−] in the films. After being exposed to air for 48 h, the solution changed its color to a pale-yellow shade, with a new absorption peak appearing at 365 nm in the absorption spectrum of the solution. This peak can be attributed to the presence of I₃[−], formed by combining I₂ and I[−] ions. Despite all these attributes, the tool has a few disadvantages. There is a lack of specificity of absorption spectra (i.e., overlapping signals from species) in

UV-vis–NIR spectroscopy. It makes distinguishing between different species in the absorption spectrum of measured products challenging. Also, measurement errors could occur due to light scattering by suspended solids in solution or stray lights from the measurement environment or light source transmission. Therefore, a full understanding of how changes in materials may affect photovoltaic properties requires a thorough analysis of multimetrology with additional tools.

2.1.2. Nuclear Magnetic Resonance

Nuclear Magnetic Resonance (NMR) is a powerful materials characterization tool to access important physical, chemical, and structural properties of organic compounds in solution or solid state by observing the quantum mechanical magnetic properties of an atomic nucleus.^[107] Elemental isotopes with magnetic spin ($I = 1/2$), such as ¹H, ¹³C, ¹⁹F, and ³¹P, are commonly used in NMR.^[108] The capabilities of ¹H-NMR make it a suitable technique to study the atomic and molecular structures of OPVs and PSCs precursors in colloidal solution. It is also used to study the geometries and phase transitions of the active layers materials often used as reference materials compared with thin films prepared for applications in optoelectronic devices.^[107] To study degradation in solution, the ¹H-NMR spectra of degraded materials are compared with those of pristine materials in the same solvent. When degradation occurs, there are noticeable changes in the spectra, such as chemical peak shifting, the appearance and/or disappearance of new peaks, and a decrease in peak intensities. Studies of the ¹H-NMR spectra of two dissolved benzol [1,2-b:5-b]dithiophene monomers under

continuous UV light^[109] have shown that proton peaks disappeared after 10 min of exposure for one monomer, while the other shows the appearance of new peaks and a decrease in the intensity of pre-existing peaks.^[110,111]

The ¹H-NMR is also very useful for studying degradation in perovskite solar cells.^[107,112,113] A proper understanding of the intermolecular interactions affecting the stability of PSCs can be gained by applying both solution and solid-state NMR. Solution NMR helps to understand the kinetics happening at the interface between the bulk of the perovskite precursors and the additives used in improving the morphology of the film, not forgetting the interaction at the surface of perovskite nanocrystals and the organic ligands. It also allows us to monitor the stability of the device over time and under different environmental stressors. Meanwhile, solid-state NMR, In contrast, helps study dried samples and powders and provides the basis for correlating perovskite properties with their crystal structure at different phases.^[114,115] This provides insight into the cation dynamics within the perovskite system. Aiello et al.^[107] extensively reviewed the use of the solution and solid-state NMR in understanding the stability of perovskites.

Like UV-vis-NIR spectroscopy, NMR is a nondestructive analytical tool, allowing for repeated measurements on the same sample. Detailed structural information about the molecules involved in the degradation process can be obtained using NMR, one of its main advantages. This makes identifying the degradation pathways and products easier and can inform mitigation strategies for degradation. Since it allows the studying of changes in the molecular structure of a material as it degrades, it may be beneficial for researching the kinetics of degradation over time. However, NMR has a low sensitivity which can restrict its ability to detect degradation products in low concentrations. Due to this sensitivity, using NMR in perovskite solar cells may be of particular concern if the metrology is not improved or adjusted. In addition, the practical use of NMR for routine characterization of solar cell degradation may also be constrained by time and cost. Thus, while NMR can be a valuable tool for understanding the structural alterations during degradation in organic and perovskite solar cells, its accessibility and sensitivity issues should be considered when employing it as a characterization technique.

2.1.3. X-Ray Diffraction

X-ray diffraction (XRD), a nondestructive analysis method based on the constructive interference of monochromatic X-rays, provides precise information on crystallographic structure, chemical composition, and physical characteristics of crystalline materials.^[116] Due to the atomic composition of the substance, each phase of the material generates a distinct diffraction pattern, which helps to determine the type and quantity of the crystalline phase.^[117] Therefore, XRD is a powerful tool to assess whether substances undergo chemical composition and crystal structure degradations.

Crystallinity is one of the most critical factors in enhancing the efficiency and stability of OSCs and PSCs. Therefore, XRD analysis can be used to assess the effect of crystallinity on the degradation of these devices.^[118–120] However, in OSCs, XRD is often

used to analyze interlayers such as crystalline metal oxides. Since the active layer of OSCs is composed of disordered or partially ordered materials, studies related to the crystallinity and chemical structures of OSCs are usually studied via GIWAXS/GISAXS, discussed later. In contrast, XRD is useful for crystalline perovskite films in PSCs. Christians et al.^[65] proposed a degradation mechanism of perovskite solar cells in which a hydrate of MAPbI₃ was formed upon exposure to humid conditions, as shown in Figure 2a. Compared to pristine CH₃NH₃PbI₃ (red pattern), the relative humidity conditions (blue and green patterns) significantly alter the XRD pattern. At low angles, several additional peaks indistinguishable from CH₃NH₃PbI₃ or PbI₂ appear. New peaks are observed at 7.93°, 8.42°, 10.46°, and 16.01°, although there are still peaks at 13.98° and 28.32° attributable to crystalline CH₃NH₃PbI₃ present in the film. No peak was observed at 12.55°, indicating the presence of crystalline PbI₂. However, the peak at 10.46° appears to increase with the time of exposure, which can be attributed to PbI₆ (Purple pattern) as marked in the synthesized (CH₃NH₃)₄PbI₆·H₂O crystals (reaction 3).



Meanwhile, Islam et al.^[121] also investigated the degradation of MAPbI₃ perovskite film based on the time evolution of XRD patterns under humid conditions for 30 days. They suggested that the decomposition of the MAPbI₃ perovskite crystal decomposition led to PbI₂ conversion (001) (See reaction 4), in contrast to reaction 3. Qin et al.^[122] also examined the long-term stability of the perovskite precursor solution through time evolution XRD patterns of the perovskite film made from stored precursor solution over time. The formation of a dominant δ-phase peak at 11.7° in the perovskite stored for a long time (>12 days) indicates that the precursor solution had undergone severe degradation over a protracted aging process. δ-phase is known to affect charge collection and device performance negatively. With an increase in aging time, the diffraction peak of the PbI₂ phase at 12.7° likewise becomes slightly stronger. The studies on formamidine-based PSCs were also conducted through XRD.^[72,79] Similarly, the α-phase of FAPbI₃ perovskite (black picture, Figure 2b) conversion into the hexagonal δ-phase FAPbI₃ phase (yellow) in ambient conditions is observed, with an undesirable high bandgap (~2.48 eV).^[123–125] Figure 2b shows the XRD patterns of FAPbI₃ film after storage under different conditions with corresponding photos.^[126] It also shows that the α-phase transitions to a δ-phase under humid conditions and partially forms PbI₂ after three days under 50% RH. The water-soaked sample shows no peak corresponding to δ-phase. However, all the α- and δ-phases are completely converted to the PbI₂ peak, proven by the evident yellowish color change in the picture. These findings and other related multiple mechanisms for device deterioration under thermal stress, light soaking stress, and humid conditions discovered via XRD, producing different degradation products such as PbI₂, hydrated perovskites, and/or gaseous pollutants, explain why this tool is widely used in stability studies.^[127,128]

One of the advantages of XRD is that it is also a nondestructive characterization tool. It is the fastest and most economical tool to

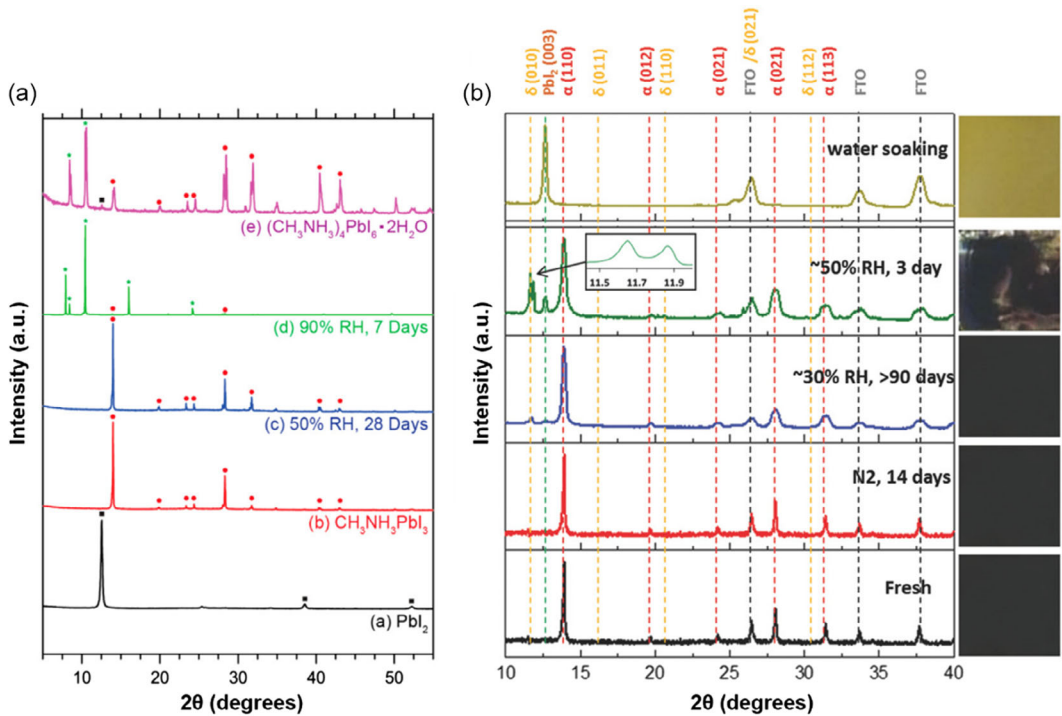


Figure 2. XRD patterns of a) a PbI_2 film, synthesized $(\text{CH}_3\text{NH}_3)_4\text{PbI}_6 \cdot 2\text{H}_2\text{O}$ crystals, and pristine and degraded films $\text{CH}_3\text{NH}_3\text{PbI}_3$ under different conditions. Reproduced with permission.^[65] Copyright 2017, The Royal Society of Chemistry, and b) a $\text{FAPbI}_3/\text{c-TiO}_2/\text{FTO}$ film stored in different environmental conditions over 90 days. Reproduced with permission.^[126] Copyright 2018, Wiley-VCH.

determine structure with relatively easy sample preparation. It allows for a wide variety of samples, such as thin films, bulk materials, or powders, to be studied. It also provides information on crystal structures with both quantitative and qualitative crystallinity and phase composition determination of materials. Thus, it helps find byproducts due to degradation and study the underlying mechanism in the degradation process. However, as mentioned above, XRD has disadvantages in that it is mainly used for crystalline materials, so there are limitations in probing fine details in the complete thin film of OSCs and PSCs as they have amorphous contents/phases. XRD also has limitations in terms of sensitivity. For instance, it has a relatively high detection limit in the order of low wt%, so it cannot detect species in the ppm range.

2.1.4. Photoluminescence and Time-Resolved Photoluminescence

Photoluminescence (PL) is a crucial experimental tool to investigate recombination and losses in bulk and at the interfaces in solar cells. It is based on the measurement of photons emitted by semiconductors due to radiative recombination. There are a few different types of PL.^[87] Our focus is on steady-state PL and TRPL. Steady-state PL is used to study charge transport dynamics within a solar cell. The measured PL peak intensity and its shift as a function of wavelength provide information on electronic structure and recombination processes in the cell. The movement of different charge carriers in the cell may result in quenching or enhancement of the PL over longer timescales (seconds). For instance, in perovskite devices or film, quenching of the PL

intensity may signalize recombination, while its shift may indicate a change in the bandgap. Thus, PL can be used to monitor these changes that may arise from degradation stressors in OSCs and PSCs, for instance, by identifying the limiting interface and components of solar cells.^[129,130] TRPL, also called transient PL, measures the PL decay rate and provides more detailed information about the charge carrier kinetics and/or recombination on a shorter timescale (micro- to picoseconds).^[131–133] While steady-state PL mostly depends on radiative recombination, the decay rate in TRPL can provide information about nonradiative recombination in bulk and the interfaces. Thus, the key recombination rate constants of Auger, bimolecular, trap-assisted recombination can be derived.^[134,135] The TRPL decay is fitted with a biexponential model (see Equation (5)), providing two extracted values of charge carriers' lifetime: the radiative and nonradiative lifetimes.^[136]

$$Y = A_1 \exp\left(-\frac{t}{\tau_1}\right) + A_2 \exp\left(-\frac{t}{\tau_2}\right) + \gamma_0 \quad (5)$$

where A_1 and A_2 are the amplitudes, and τ_1 and τ_2 are the radiative and nonradiative lifetimes, also referred to as the fast and slow recombination lifetimes, respectively. Lifetime values depend on many other parameters, such as illumination conditions, recombination coefficients, doping of the absorber material, charge extraction, carrier mobilities, and trap density, which also influence each other. In general, the shape of the TRPL decay depends on the radiative and nonradiative recombination rates of the photogenerated charge carriers. The

nonradiative recombination rate, which primarily affects the slope of the long tail and has a linear dependence on the photo-generated charge carriers, can be adjusted by the capture and emission rates of the charge carriers.^[137]

Duan et al.^[138] investigated the burn-in thermal degradation of nonfullerene-based OSCs. Figure 3a shows normalized steady-state PL spectra of fresh and degraded devices with and without air. An increase in PL peak intensity is observed for devices degraded in the air at around 750 nm and for degraded devices without air at about 920 nm. This increase in PL intensity of degraded devices reveals higher charge carrier recombination caused by undissociated exciton in the active layer, consequently negatively affecting the device performance during burn-in. The charge carrier's lifetime of fresh and aged devices is also determined using TRPL, as shown in Figure 3b. The lifetime was calculated using a biexponential decay model (consisting of fast and slow decay regimes). After 5 h of degradation, the fast carrier lifetime increased from 0.089 to 0.127 ns without air and 0.135 ns with air. Slow carrier lifetime was increased from 1.048 to 2.226 without air and 2.330 with air. Figure 3c shows the charge carrier lifetime in fresh and degraded PM6:N3-based OSCs using TRPL.^[139] Devices were degraded under 1 sun illumination and 85 °C for 5 h. After the 5 h burn-in degradation, both fast and slow decay lifetimes increased from 0.108 to 0.114 ns and 0.940 to 1.038 ns, respectively. This result indicates that the degraded device has a less efficient energy transfer process, explained as Förster resonance energy transfer (FRET).^[139] FRET provides an alternative nonradiative pathway between the donor and acceptor. As a result, the

increased carrier lifetime in the degraded devices indicates less efficient charge carrier extraction. In other words, faster PL decay means that charges are efficiently extracted before recombination.^[87,140]

However, it should be noted that a fast PL decay can also be attributed to increased charge recombination due to trap states in a sample.^[137,141,142] Figure 3d shows the PL intensity of perovskite film modified with PFTS (H,1H,2H,2H-perfluorooctyl trichlorosilane). The PL intensity increased after 16 days of exposure in 70% RH condition, which implies suppressed charge recombination in the modified perovskite film. Further investigation on charge carrier kinetics was conducted using TRPL. Figure 3e shows the TRPL spectra of PSCs with different treatment times in PFTS vapor (from 1 to 120 min) to verify the passivation effect of PFTS.^[143] The biexponential fitted carrier lifetime showed a gradual increase in the slow lifetime from 102.97 to 329.56 ns as the fresh sample was treated under PFTS vapor from 0 to 20 min. This prolonged lifetime was attributed to the trap state passivation by the hydrolysable PFTS, reducing charge recombination at surface and grain boundaries. Figure 3f shows the TRPL measurement of aged control and PFTS-10 samples under the same condition as in Figure 3d. During film aging in humidity, the average lifetime of the control film decreased from 41.02 to 6.65 ns, while the average lifetime of PFTS-10 film increased from 165.55 to 759.78 ns, an outcome that is consistent with the PL result. It suggests that the hydrolyzed PFTS could lead to further hydrolysis by forming electrophilic Si-OH bonds with penetrated moisture, passivating the flaws in the grain boundaries.

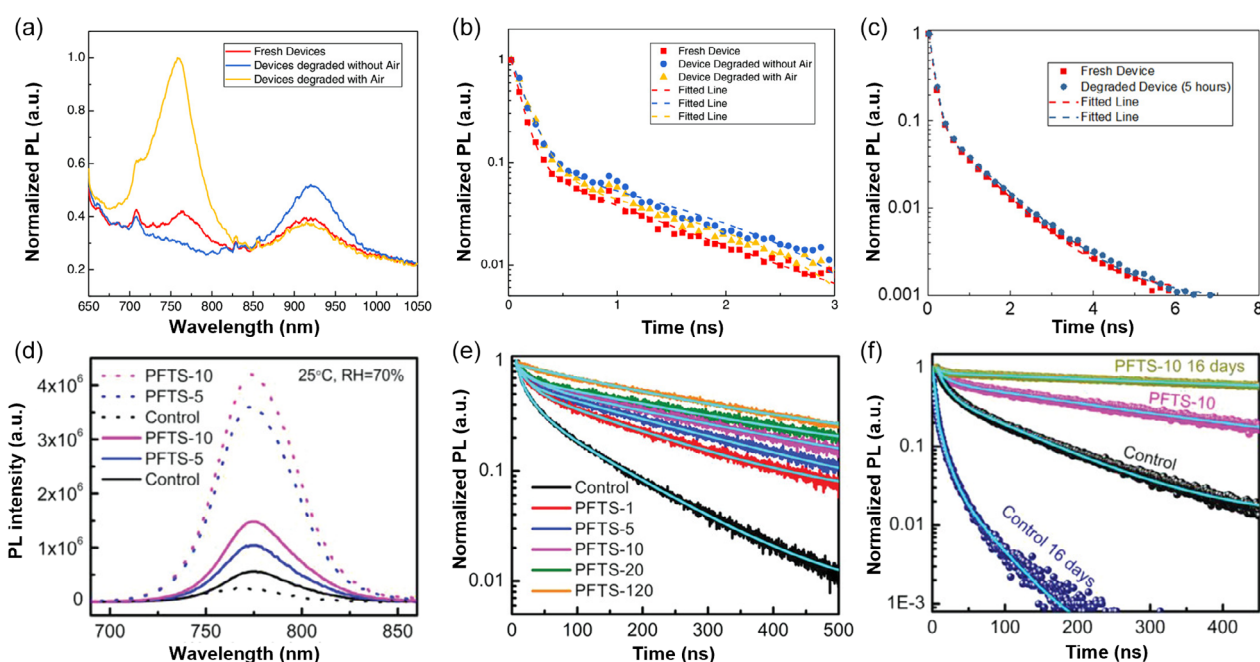


Figure 3. a) Steady-state PL and b) TRPL of fresh and degraded devices without and with air, with their fitted lines, and excited at 532 nm wavelength. Reproduced with permission.^[138] Copyright 2020, Wiley-VCH. c) TRPL spectrum of fresh and degraded PM6:N3 film on top of ITO/ZnO under 532 nm light excitation. Reproduced with permission.^[139] Copyright 2021, Wiley-VCH. d) Steady-state PL of perovskite film after aging 16 days in 70% RH and e) TRPL of perovskite film treated in PFTS vapors under vacuum for 1 to 120 min (denoted as PFTS-1 to 120), and f) perovskite film (PFTS-10) after aging 16 days in 70% RH. Reproduced with permission.^[143] Copyright 2020, Wiley-VCH.

Both PL and TRPL are nondestructive techniques; thus, they are good tools for monitoring changes in photoexcitation kinetics in materials and devices during degradation without altering the sample properties. PL is a relatively straightforward technique. TRPL provides more detailed information about the kinetics of carrier recombination and lifetime, while the interpretation can be more complicated depending on the sample conditions. PL and TRPL can be used as complementary characterization tools for probing degradation mechanisms. A third complementary tool in this space is transient absorption spectroscopy, discussed in the next section.

2.1.5. Transient Absorption Spectroscopy

Transient absorption spectroscopy (TAS) measures change in the absorbance and transmittance across nanosecond to femtosecond timescales after excitation by incident light, like in time-resolved measurements. While the luminescence of material is monitored in TRPL, the difference in absorbance before and after the pump is monitored in TAS. Unlike TRPL, which requires the molecules to be luminous to be measured, TAS has no such restriction.

Charge generation processes in fresh and degraded films of D:A materials can be investigated by ultrafast femtosecond TAS. Weu et al.^[119] examined the environmental stability of

OSCs consisting of the small molecule donor DRCN5T and fullerene acceptor PC₇₀BM. The kinetics of DRCN5T and PC₇₀BM can be seen in Figure 4a,b. Excitons are produced within 80 fs following a 700 nm pump pulse excitation and recombined within 300 ps. With over 9 hours of degradation, no change in the exciton dynamics was observed. A pump pulse at 350 nm produced excitons in the clean PC₇₀BM material. However, the exciton lifetime is significantly decreased from 50 to 7 ps after continuous oxygen and light exposure for 7 h, indicating degradation of PC₇₀BM due to oxygen and light. In a second study, Weu et al.^[144] also utilized femtosecond TAS to investigate charge-generation processes in the degradation of OSCs, as shown in Figure 4e. The exciton lifetime decreased under degradation conditions. Therefore, most photodegradation is considered to occur within 15 minutes of degradation due to oxygen and light exposure. Similarly, TAS was also used to understand the photostability of OSCs by Yi et al.^[145] Figure 4c,d shows the exciton dissociation dynamics monitoring the evolution of charge transfer (CT) features at D:A interfaces in PTB7-Th:O-IDTBR and PffBT4T-2OD:O-IDTBR blends, respectively. The difference of CT exciton features as a function of time was negligible in PTB7-Th:O-IDTBR film before and after light degradation retaining a lifetime of 30 ps. In contrast, the CT exciton dynamics of the PffBT4T-2OD:O-IDTBR film decreased from 60 to 5 ps after one-hour illumination, which indicates more efficient CT exciton dissociation, consistent with the

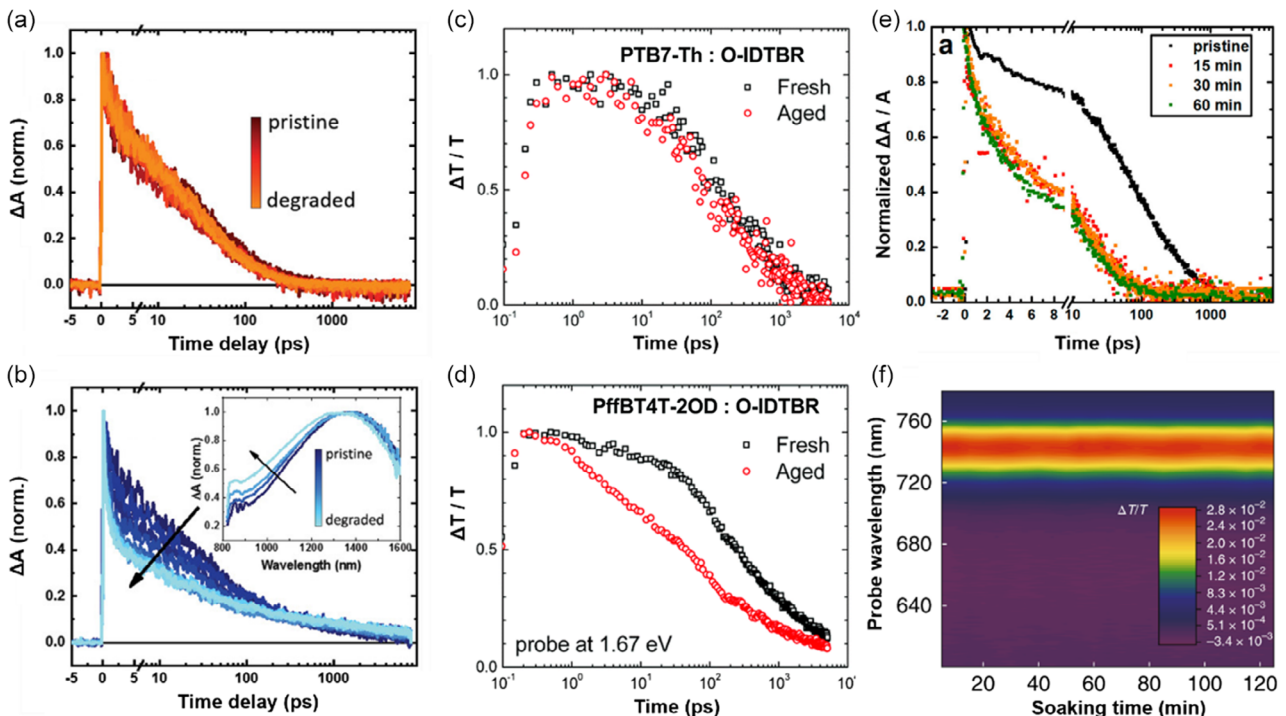


Figure 4. TAS for the neat materials in the studied blend. a) Kinetics of DRCN5T excitons upon degradation for 9 h. b) Kinetics of PC₇₀BM excitons upon degradation for 7 h. Reproduced with permission.^[119] Copyright 2019, Wiley-VCH. TA spectra at 10 ps of c) PTB7-Th:O-IDTBR and d) PffBT4T-2OD:O-IDTBR fresh and degraded thin films under one sunlight illumination for 45 h. Reproduced with permission.^[145] Copyright 2020, The Royal Society of Chemistry. e) Exciton and charge dynamics in PffBT4T-2OD:PC₇₁BM films at different stages of oxygen degradation in light: decrease in exciton lifetime after degradation in oxygen and light. Reproduced with permission.^[144] Copyright 2019, American Chemical Society. f) TAS (100–120 ps average) of the perovskite active layer with illumination time under vacuum (3.4 × 10⁻³ Pa). The color bar represents the change in the transmission of the broadband probe pulse. Reproduced with permission.^[146] Copyright 2021, Springer Nature Limited.

slightly increased J_{SC} in PffBT4T-2OD: O-IDTBR-based device under illumination.

Meanwhile, Guo et al.^[146] investigated the stability of PSCs under one sun illumination in vacuum and nitrogen conditions. They presented the evolution of TAS with a color band map. Figure 4f shows the probe wavelength as a function of soaking time in the perovskite active film under vacuum and light illumination for 120 min. The color bar shows the change in the transmission of broadband probe pulse when a pump pulse photoexcites the sample. There were no changes in the transmission, while a 20% decrease in V_{OC} was observed for the devices. Thus, the V_{OC} decrease was not due to changes in the band alignment. The investigated TAS mapping points to a negligible effect of illumination on radiative, nonradiative relaxation, and vibrational relaxations of the perovskite film.

It appears TAS enables the investigation of the charge carrier dynamics during device stability studies, which is indispensable to improving the inherent degradation in solar cells. In principle, TAS provides similar information to TRPL by measuring the time-resolved properties of the material. Both tools are nondestructive and can measure charge carrier kinetics. While TRPL provides kinetic information such as charge carrier lifetime and recombination by measuring the decay of PL intensity, TAS gives information about carrier dynamics that explain both kinetics of charge carrier generation and recombination and their pathway, such as defects states, by measuring the changes in electronic state distribution of the absorption spectrum over time. Therefore, comprehensive measurements using both tools can be critical analytical methods to study the degradation mechanisms in OSCs and PSCs. Both tools share a common weakness: the difficulty in analyzing complex data and the insufficient spatial information available to evaluate degradation in the samples.

2.1.6. Atomic Force Microscopy (AFM)/Conductive AFM (c-AFM)

Thin film characterization is crucial for correlating crystal size to the photovoltaic response. Atomic force microscopy (AFM) enables high-resolution surface mapping of thin film structures in three dimensions and provides insight into the microstructure of devices. In addition, (Photo-)conductive AFM (c-AFM) measures electrical and morphological features of the photoactive layer under illumination. This allows for pinpointing the locations where defects occur on the surface of the photoactive film along the topography and monitoring performance variations across the entire device. In contrast, the conventional AFM only provides topography images.^[147–149] c-AFM can therefore support further research in improving the efficiency and stability of OSCs and PSCs. In a nutshell, (c)-AFM can be used to observe drastic changes in morphology or electrical responses under degradation stressors.

The air effect in the burn-in of thermally degraded nonfullerene OSCs is investigated by Duan et al.^[138] They show that the excessive degradation in the exciton dissociation process with air is primarily caused by air-induced phase separation. The obtained AFM images and calculated roughness (RMS) values are shown in Figure 5a–c. The roughness of the degraded active layer in or without air is higher than that of the fresh active layer,

indicating an enhanced aggregation tendency inside the active layer. Furthermore, the AFM image of the degraded active layer in air displays a fiber-like shape with increased domain size, indicating a significant phase separation.

Ma et al.^[150] investigated facet-dependent degradation of PSCs. When PSCs are exposed to moisture, the (100) facet, which is the most common facet found in perovskite thin films, is reported to limit the overall stability of the perovskite and exhibit a rapid phase shift to δ -phase, whereas the (111) facet is substantially more resistant to moisture-driven degradation.^[150] As seen in Figure 5d–f, the authors use AFM to evaluate changes in surface morphology and electrical characteristics during facet degradation in PSCs. They exposed a fresh sample with smooth (100) and (111) facets to ambient air with relative humidity (RH) of 30–40% for 72 h. The AFM image of the degraded sample is represented in Figure 5e. In contrast to the lateral (100) facet, the triangular (111) facet degraded differently. The (100) facets, in particular, reveal newly formed crystals that can be seen as tiny swellings (yellow rectangles), while the (111) facets are almost impervious to degradation. Figure 5f shows the (100) facets degraded significantly more than the (111) facets after being exposed to ambient air for 200 h. As a result, they suggest that the (100) facets are inherently unstable and can easily undergo a phase transition to δ -phase when exposed to moisture.

In brief, AFM is a powerful tool for analyzing surface topography and mechanical properties. This is important for studying degradation because it can provide high spatial resolution images of defects, voids, or pinholes caused by degradation, typically at scales of a few nanometers. In particular, c-AFM shows the electrical properties corresponding to the topography, which can compensate for the weakness of other tools mentioned above. However, AFM has disadvantages like slow scan speed and limited depth information, such as internal structure, since it is only a surface analysis tool. Yet, it is one of the most important and widely used analytical tools for morphology studies.

2.1.7. Grazing Incidence Small/Wide Angle X-ray Scattering

Unlike bulk film, the measurement of a thin film can be difficult using X-ray techniques such as small-angle X-ray scattering (SAXS) and wide-angle X-ray scattering (WAXS). The X-ray penetration length is limited due to its low thickness. Thus, SAXS and WAXS are generally less suitable for thin films. As such, reflection is used instead of transmission to address this problem at an incident angle much lower than 90°. As a result, the beam follows a noticeably extended path inside the thin layer, leading to the introduction of the grazing-incidence technique.^[151] Grazing-incidence small-angle X-ray scattering (GISAXS) is a useful tool for examining the morphology and structure of materials with domain size, phase separation, and purity. Grazing-incidence wide-angle X-ray scattering (GIWAXS) can be obtained by extending GISAXS. However, GIWAXS uses an area detector without collimation, which works up to a scattering angle of about 30°. Semicrystalline polymer films, including conjugated polymers, are studied with GIWAXS to investigate crystallinity, crystal orientation, and size.^[152,153]

In a thermal stability study of quaternary OSCs conducted by Zhang et al.,^[141] the morphology evolution of multicomponent

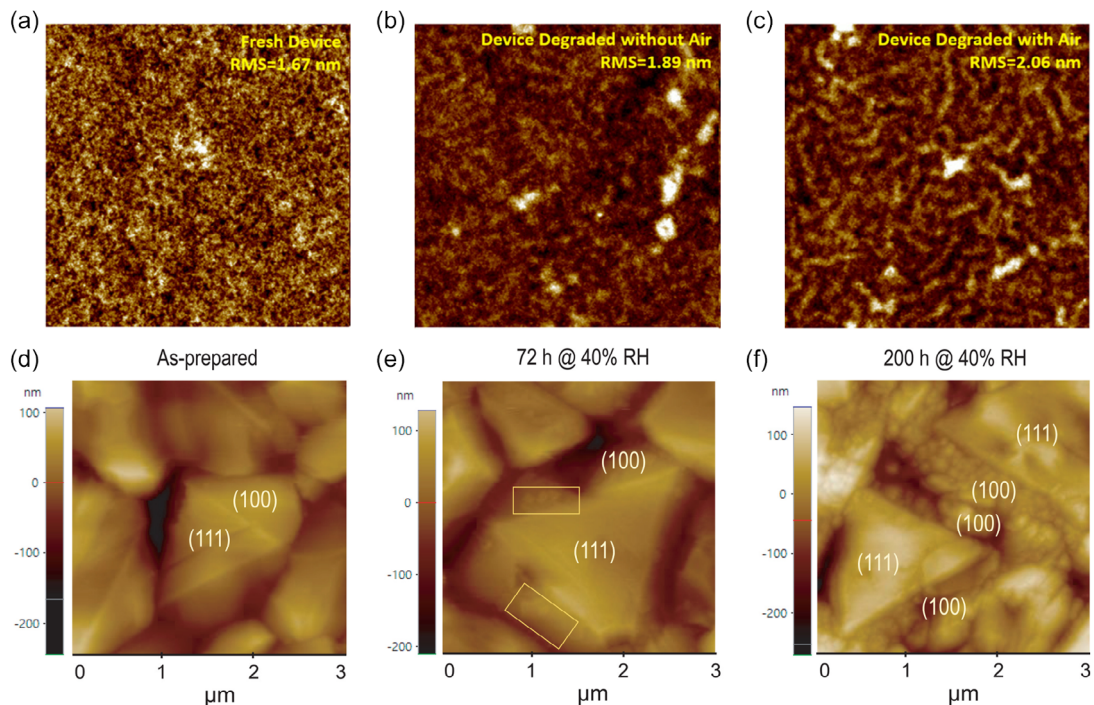


Figure 5. AFM images with the RMS value of a) the fresh device, b) the thermally degraded device without air, and c) thermally degraded with air c) of PTB7-th:IEICO-4 film on ITO/ZnO surface. Reproduced with permission.^[138] Copyright 2020, Wiley-VCH. AFM images of FAPbI₃ perovskite thin films of d) the fresh sample, e) the sample degraded under 30–40% RH for 72 hours, and f) the sample degraded under 30–40% RH for 200 h. The (100) and (111) facets are marked on the images; the yellow rectangles in (e) indicate the degraded parts on the (100) facet with swellings. Reproduced with permission.^[150] Copyright 2023, American Association for the Advancement of Science.

blends was studied through GIWAXS analysis to verify the proposed underlying correlation mechanisms between intermolecular electron-phonon coupling and photocarrier trapping for BHJ and layer by layer-type binary and quaternary systems. In Figure 6a–c, the primary orientation is determined to be face-on as stronger (010) π – π stacking peaks are observed in the out-of-plane direction compared to the in-plane direction. As shown in Figure 6d,e, the intensity of the scattering needs to be measured to quantify the orientation distribution. Both (010) d-spacing and (010) crystalline coherence lengths are represented in Figure 6f. Following thermal aging at 85 °C for 100 h, a substantial crystallinity reduction of the aged binary blends can be identified by the declining intensity of (010) π – π stacking peaks. In contrast, the quaternary systems exhibit comparatively constant crystallinity with π – π interactions even after thermal age treatment. The reduced crystallinity with π – π interactions in the binary blend may hinder charge transport and photovoltaic performance in their devices.

A thermally induced decrease in crystallinity of PSCs is also observed through GIWAXS alongside scanning electron microscope (SEM) images by Perini et al.^[142] Details of this particular study can be found in the literature. As such, GIWAXS and GISAXS provide detailed information on thin film molecular orientation and crystallinity. They enable the study of crystal growth and phase transitions. GIWAXS is also a nondestructive measurement and is useful for studying thin films of a wide range of materials, including polymers, metals, ceramics, and semiconductors. However, it requires a synchrotron radiation source.

This means extra careful planning, timing, and possibly getting beamtime via proposals. Thus, it is worth mentioning that both techniques are often used in conjunction with other analytical tools, including XPS, SEM, and AFM, for a comprehensive study and to have an in-depth understanding of the investigated phenomenon. It is essential to mention here that a newly developed complementary technique to GIWAXS and GISAXS in the X-ray scattering family is the polarized resonant soft X-ray scattering (P-RSoXS).^[154,155] P-RSoXS is a molecular scale structure measurement tool for soft materials, mainly used to probe organic electronic devices.

2.1.8. Scanning Electron Microscope

Scanning electron microscope (SEM) is one of the most used characterization techniques in the study of materials due to its ability to reveal the morphology/microstructures of material with high spatial resolution up to 1.2 nm.^[156] It is because a beam of highly energetic electrons (usually in the range 0.1–50 keV) is incident on the material. The incident beam interacts with the sample producing backscattered electrons, secondary electrons, photons, and X-rays, as well as the excitation of phonons under certain conditions. The images of these different processes can be captured using suitable detectors since the incident electron beam is usually scanned in the X-Y plane. For most SEM instruments, the secondary electron detector records the topography of the sample under investigation with magnification ranging from

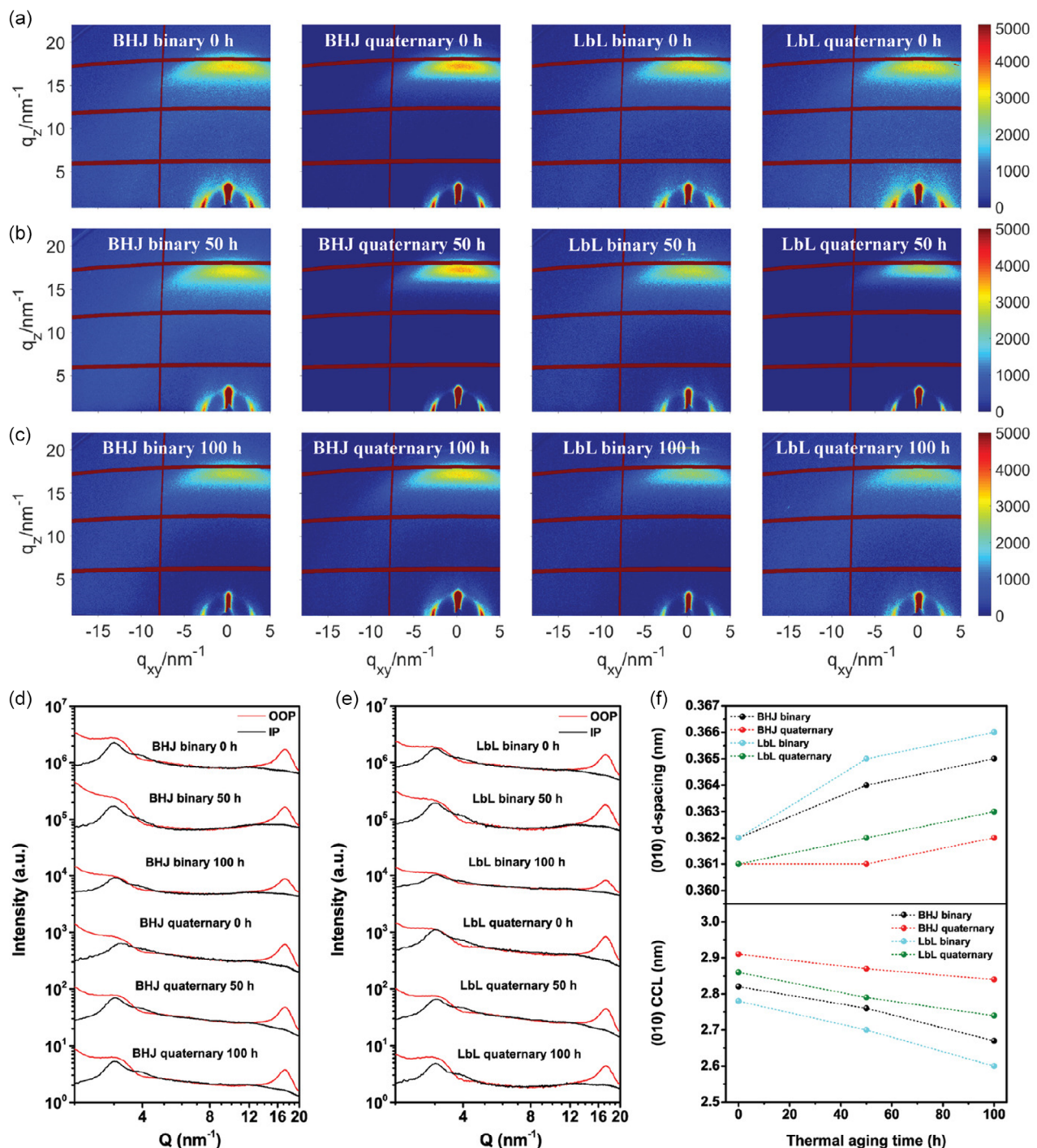


Figure 6. 2D GIWAXS patterns for a–c) BHJ-type binary, BHJ-type quaternary, LbL-type binary, and LbL-type quaternary blends against annealing time at 85 °C. The corresponding out-of-plane and in-plane line cuts of d) BHJ-type and e) LbL-type blends against annealing time at 85 °C. f) The d-spacing and crystalline coherence length (CCL) of (010) π – π stacking peaks for BHJ-type and LbL-type blends against annealing time at 85 °C. Reproduced with permission.^[141] Copyright 2021, Wiley-VCH.

10× to 500 000× and a resolution between 1 and 2 nm.^[156] The use of other detectors, such as EDX, can reveal information regarding properties like the composition, phase changes, electrical, optical, and thermal behavior of the sample. SEM can help in revealing the degradation mechanisms in OSCs and

PSCs.^[157–159] Priyanka et al.^[160] used SEM to experimentally study the degradation mechanisms in PSC under different degradation factors.

Figure 7a shows the SEM image for the fresh sample, which revealed no pinholes or deformation. When exposed to

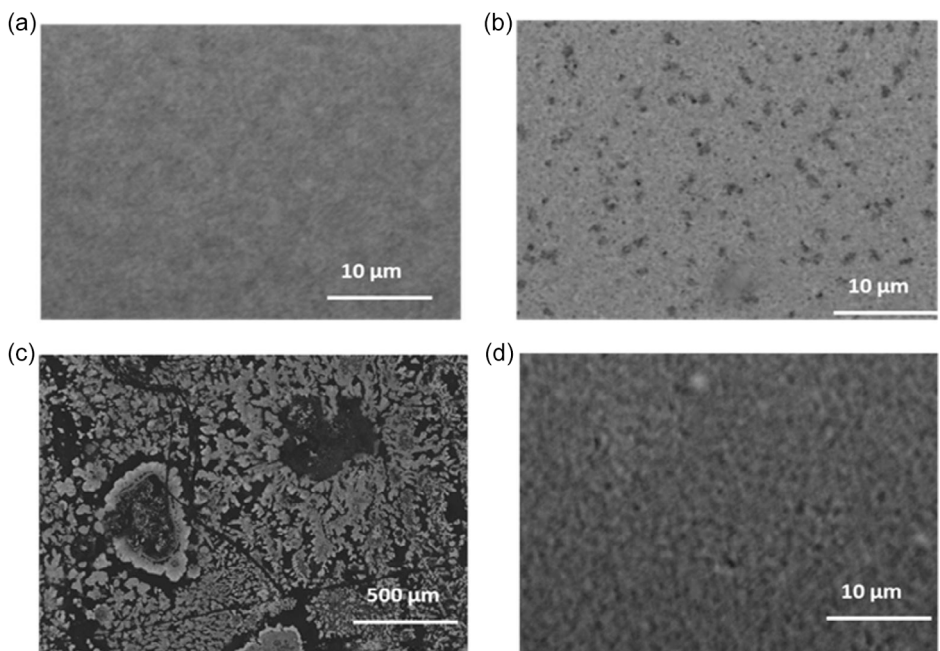


Figure 7. SEM images of a) fresh sample, b) sample degraded under continuous light exposure without any extrinsic stress, c) with humidity and oxygen, and d) with UV. Reproduced with permission.^[160] Copyright 2019, Elsevier Inc.

continuous illumination without additional factors, pinholes of about one micrometer can be observed, as shown in Figure 7b. With illumination in the presence of humidity and oxygen, the film experienced severe degradation (see Figure 7c), suggesting that humidity and oxygen drastically affect the stability of PSCs leading to enlarged pinholes and/or voids present in their films. This observation confirmed what Song et al.^[161,162] and Juarez-Perez et al.^[161,162] showed earlier. Humidity and oxygen cause MAPbI_3 PSCs to decompose into MAI and PbI_2 with the possibility of further decomposition into Pb and Iodine. In Figure 7d, the film exposed to UV light showed a larger density of small pinholes. These results illustrate how one or more factors affect degradation in the absorber layers of PSCs.

In the case of OSCs, Glen et al.^[163] used cross-sectional TEM and SEM to study the degradation of aluminum/calcium cathodes in organic solar cells when exposed to air. The exposure resulted in the formation of voids at the aluminum/calcium interface and large bubble-like protrusions on the surface of the device. They also noticed that water ingress into the device was through the edges, not the pinholes and defects in the aluminum film.^[163] Figure 8 shows the SEM images of the early-stage degradation in their devices measured after every hour for 4 h. The first row shows small-grained devices, while the second shows large ones.

The use of SEM to investigate the degradation mechanisms in OSCs and PSCs can reveal helpful information unique to the tool. One of the advantages of the tool is the ability to obtain high-resolution images of the nanoscale morphology of the sample that can be used to understand the degradation mechanism and the damage done to the cell. Especially, cross-section SEM can reveal deamination, void, or defects due to degradation stressors, which otherwise may not be present or significant in the

fresh sample. SEM can be used to map the distribution of the sample's elements to locate defects and the formation of impurities. It can also offer early detection of details on the sample, which can lead to failures, such as cracks, voids, and other flaws that could affect the performance of the solar cell. Meanwhile, the disadvantages of this technique include its inability to probe beyond the surface of the sample into the bulk of the devices, which may not be sufficient to obtain complete information on the degradation mechanisms. Also, the sample preparation procedure for this technique requires diligence and a high level of expertise to be sure that comprehensive and reliable information can be obtained. The high vacuum requirement can also be a barrier since it differs from the operating conditions of OSCs and PSCs. Considering some of its limitations, SEM is highly recommended to be used with other characterization techniques, such as EDS, to get a complete story of the thin film or device.

2.1.9. Transmission Electron Microscope

First developed in 1931 by German scientists Max Knoll and Ernst Ruska, the transmission electron microscope (TEM) is an instrument used to study the structure, crystallinity, morphology, and stress of tiny specimens (usually at the micro and nano-scale order).^[164] The magnification and resolution of images obtained through TEM analysis are usually higher when compared with images obtained from light and/or scanning electron microscopy. For TEM analysis, an electron gun with a tungsten filament, often located at the top of the instrument, emits a beam of electrons in a vacuum chamber. This electron beam is accelerated down the column of the instrument as a narrow beam with the help of an electromagnetic field. After passing through the small specimen, the electrons hit a phosphor screen to

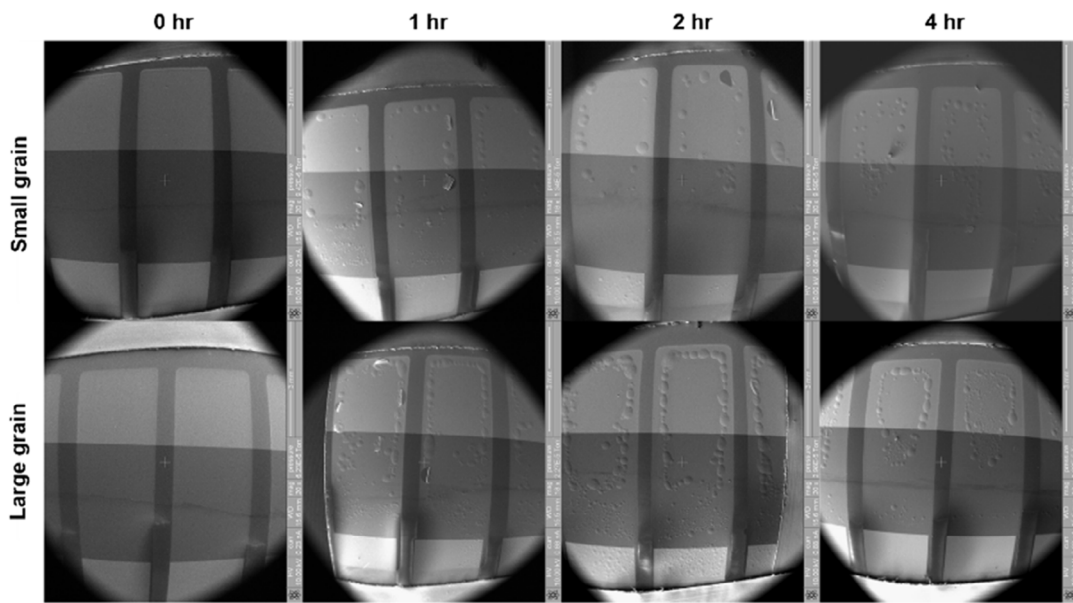


Figure 8. SEM Images showing the early stages of degradation. The top row shows small-grained devices, while the bottom row shows large-grained devices. The columns show devices aged for 0, 1, 2, and 4 h. Bubbles effects are seen moving from the edge of the cathode stripes. Reproduced with permission.^[163] Copyright 2015, Elsevier Inc.

produce an image with the sample's information. A bright image indicates low-density regions in the sample where electrons could pass through easily. In contrast, a dark image represents regions of higher density within the sample where only a few electrons could easily pass through.^[165]

TEM can be used to study the degradation mechanism in OSCs and PSCs since they undergo structural and morphological changes during degradation.^[90,166] However, TEM imaging of PSCs is a little tricky. It must be carefully conducted since PSCs are beam-sensitive and can undergo unwarranted degradation during high-voltage TEM analysis.^[90] Li et al.^[167] employed a cryoelectron microscopy (Cryo-EM) technique to circumvent this difficulty in studying the degradation mechanisms and atomic structure of organic-inorganic halide PSCs. Figure 9a shows that when MAPbI_3 nanowires were exposed to an electron beam of approximately $500\text{ e}\text{\AA}^{-2}$ (about the conditions for standard TEM measurements), the perovskite decomposed into PbI_2 (Figure 9b). They drop-casted fresh or UV/moisture-exposed perovskite nanowires onto a quantifoil TEM grid using cryo-EM in a nitrogen glovebox. They immediately submerged and froze the samples in liquid nitrogen inside the glovebox. The cryo-EM images of the samples in Figure 9c,e depict the smooth surfaces of the nanowires. Figure 9d,f are the atomic level resolution images of MAPbI_3 and MAPbBr_3 taken with electron doses of ≈ 12 and $46 \text{ e}\text{\AA}^{-2}$, respectively.

In fact, Cryo-EM is not that new as a technique. It was developed in the early 1980s as a high-resolution method for studying samples cooled to cryogenic temperatures, such as small biological complexes. Usually, the structure of the biological specimens is preserved using a vitreous ice environment. An aqueous sample solution is applied to a grid mesh and submerged in liquid ethane or liquid ethane and propane mixture to freeze it.^[139] This helps preserve the structure from being damaged by the

beam. Similarly, due to the nitrogen-freezing of the perovskite samples, one can avoid beam damage, as depicted in Figure 9c,e in contrast to standard TEM in Figure 9a. The advantage of TEM is the high-resolution images of the internal structure of the sample it provides. These images can reveal the degradation mechanism and the nanoscale damage done to the cells. Like SEM, TEM can map the distribution of elements in a sample, which can be used to locate defects and the formation of impurities. As understanding the electronic properties of the solar cell is crucial for elucidating performance and degradation mechanisms, imaging with TEM may reveal the sample's crystal structure, which is useful in studying how defects such as dislocations and grain boundaries form and impact the devices in general. As a downside, TEM requires tiny samples, which may not represent the cells or size used in functional devices.

2.1.10. Energy-Dispersive X-Ray Spectroscopy

Energy-dispersive X-ray spectroscopy (EDS or EDX) is a complementary characterization technique to SEM or TEM to determine and quantify the chemical elements in a material. EDS elemental mapping is obtained by coupling an electron microscope with an EDS detector.^[165] In an SEM or TEM, the material absorbs energy and dissipates it through the ejection of core-shell electrons. An outer-shell electron with higher energy takes the place of the ejected core-shell electron, thereby releasing an X-ray, the difference in energy, with a spectrum characteristic of the atom's origin.^[168] The peaks' position in the spectrum shows the chemical elements present in the bulk material, while the peak intensities indicate the concentrations of each element. EDS can monitor changes in elemental composition in both OSCs and PSCs due to degradation over time.

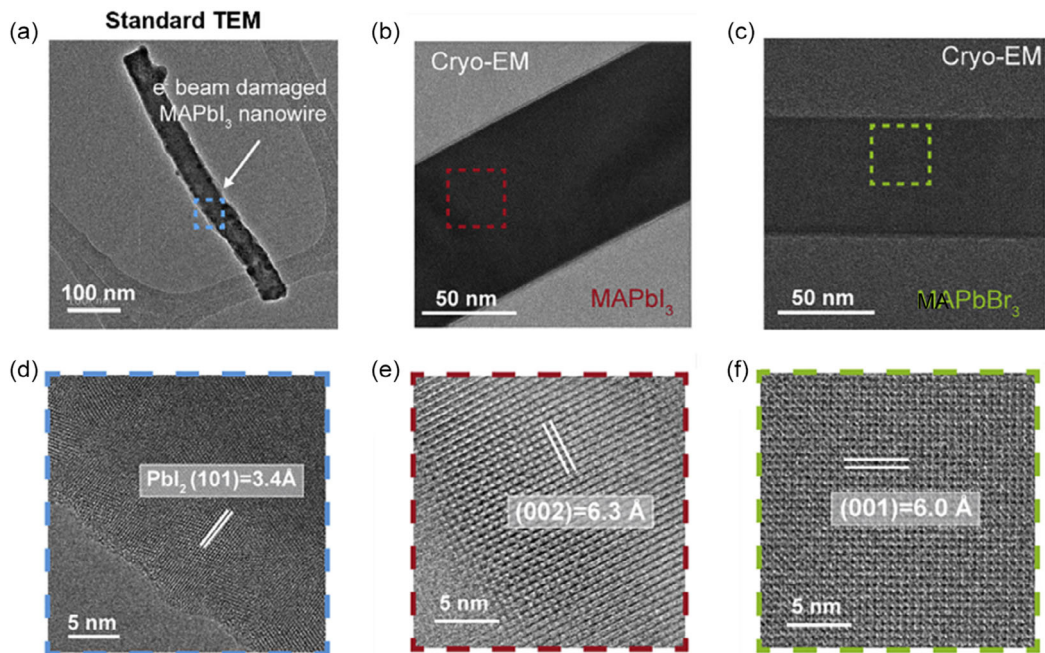


Figure 9. Using Cryo-EM to preserve and stabilize perovskites for TEM imaging. a) Standard TEM imaging, b) decomposed MAPbI_3 nanowires from standard TEM, c) Cryo-EM of MAPbI_3 , d) atomic-level resolution of MAPbI_3 Cryo-EM, e) Cryo-EM of MAPbBr_3 , and f) atomic level resolution of MAPbBr_3 Cryo-EM. Reproduced with permission.^[167] Copyright 2016, Macmillan Publishers Limited.

Divitini et al.^[169] combined in situ scanning transmission electron microscopy (STEM) with EDS to confirm the degradation caused by heat-activated ion migration in PSCs by examining FTO/compact TiO_2 /mesoporous $\text{TiO}_2/\text{MAPbI}_3$ /spiro-MeOTAD/Au. Information regarding the morphological changes with spatial resolution at the nanometer scale level was obtained from STEM. At the same time, the EDS provided insight into the elemental compositional changes within the device at different temperatures. The sample showed relatively

minimal changes before temperatures reached 150 °C. Degradation in the perovskite layer began at 175 °C with the migration of iodide ions into the spiro-OMeTAD layer. Iodide diffusion became clearer at temperatures higher than 175 °C. Morphological changes became very noticeable in the perovskite layer as well. In **Figure 10**, high-angle annular dark-field (HAADF) images and EDS maps provide clear evidence of perovskite decomposition at 225 °C, and the MAPI_3 had completely decomposed before 250 °C.

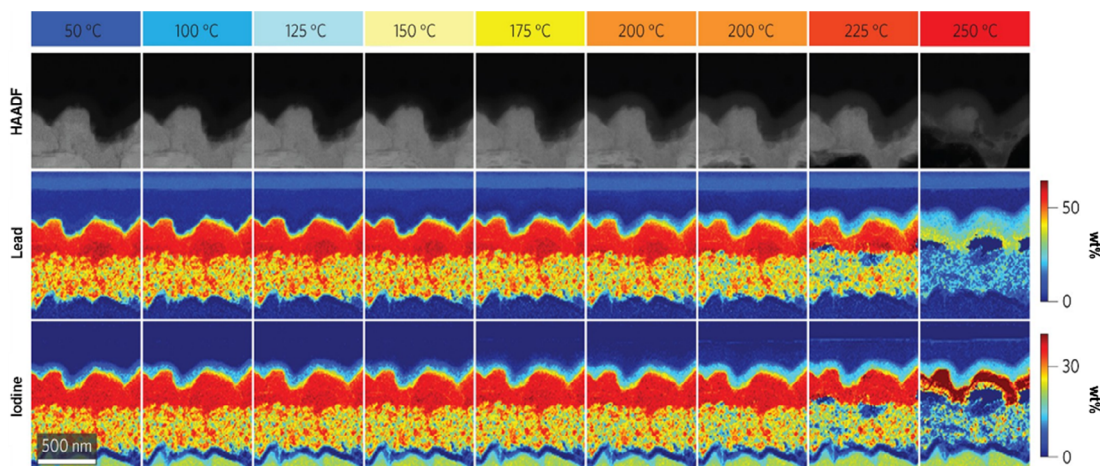


Figure 10. Heat-induced ion migration. Iodine and lead HAADF images and EDS elemental maps for FTO/compact TiO_2 /mesoporous $\text{TiO}_2/\text{MAPbI}_3$ /spiro-OMeTAD/Au at different temperatures with heating steps of 30 min to 175 °C and 15 min from 200 °C due to the faster sample dynamics. Diffusion of iodine into the HTM is visible at low temperatures, and Lead migration is triggered at higher temperatures (≈ 175 °C). Reproduced with permission.^[169] Copyright 2021, Elsevier Inc.

Two major advantages of EDS are its nondestructive nature and its ability to deliver details about a material's elemental composition. This can be useful in recognizing degradation products and following their mechanisms over time. However, the technique is only for surface analysis. It has a relatively low sensitivity, which may restrict its ability to detect low concentrations of elements, particularly when analyzing thin layers or small areas. It also fails to detect elements with low atomic numbers. It is also necessary to carefully prepare the sample for analysis, which can be challenging for some samples, such as those with rough or irregular surfaces. The accuracy of the results may also be compromised by surface contamination or damage during the analysis.

2.1.11. X-Ray Photoelectron Spectroscopy

X-ray photoelectron spectroscopy, commonly called XPS, is used to study the surfaces of materials and/or devices, usually in the 1–10 nm range (three atomic layers thick).^[170] XPS is also known as electron spectroscopy for chemical analysis (ESCA). A sample surface is irradiated with a beam of X-rays, and the kinetic energies of electrons emitted from the surface are measured. A photoelectron spectrum is obtained by counting the electrons ejected over a range of kinetic energies. Except for hydrogen, all other surface elements can be identified and quantified by analyzing the energies and intensities of the photoelectron peaks.^[171] Surface characterization of materials and/or devices is fundamental as surfaces link the external environment and the bulk of the material or device. As such, how surfaces are engineered can significantly influence factors such as adhesion, wettability, corrosion rate, contact potential, catalytic action, and failure modes.

XPS is a very convenient tool for studying the photochemical and thermal degradation mechanisms in OSCs and PSCs at the atomic and electronic levels. It can accurately examine the local bonds between constituent atoms and the density of occupied states. Kettle et al.^[172] used XPS to study the chemical degradation of the PTB7 polymer. They found that the rapid photo-degradation of the polymer, especially under illumination in air, is strongly related to changes in the chemical structure of the polymer. More precisely, the XPS spectra revealed that the relative C–C intensity witnessed an initial decrease due to the loss of the alkoxy side chains within the polymer. This is followed by a drastic increase in oxygen-bonded constituents level (i.e., C–O at approximately 286.5 eV and C(=O)O at 289.2 eV), indicating the formation of COOH and OH groups and oxidation of S. Their XPS results confirmed that the use of processing additives reduces the chemical stability of the polymer and also gave a clue on how to improve the design of the molecule to achieve higher stability.^[173]

In PSCs, Zhidkov et al.^[174] combined XPS with density functional theory (DFT) to study the degradation processes in APbX₃ hybrid halide perovskites using I[−] and Br[−] as the X-site anion and CH₃NH₃⁺, (CH(NH₂)₂)⁺, and Cs⁺ as the A-site cations. Unlike most XPS studies where only core level measurements are used, they used the entire XPS spectra (core level, survey, and valence band). This enabled them to understand the electronic structure and chemical bonding more accurately

in the perovskite materials. Heat and light soaking affect the stability of the APbX₃ hybrid halide perovskites leading to the formation of degradation by-products such as PbX₂, which can be best monitored by employing high-energy resolved XPS. In this study, the researchers also probed the spectra of lead (Pb 4f) electrons emitted from the 4f orbital, iodine (I 3d) electrons from the 3 d orbital, and the valence band. Finally, by substituting the A-site cation from CH₃NH₃⁺ to (CH(NH₂)₂)⁺ and Cs⁺, they gradually increased the resistance of PSC to stress factors such as heat and light.^[174] Figure 11 shows that in addition to causing changes in Pb-X chemical bonding, the formation of PbX₂ phases is accompanied by changes in the I:Pb ratio, clearly visible in XPS survey spectra.^[174] These changes can also be seen in the Pb 4f (Figure 11a), I 3d (Figure 11b), Br 3d core level (Figure 11c), and valence band XPS spectra (Figure 11d). Compared to CH₃NH₃PbX₃, the intensity maxima of PbX₂'s XPS Pb 4f, I 3d, and Br 3d spectra are found at higher binding energies. Therefore, these spectra make it simple to identify whether the PbX₂ decay product is fully or partially formed. According to the DFT calculations, iodine 5p states predominate at the top of the valence band of CH₃NH₃PbI₃ and CH₃NH₃PbI₃. The decrease of the I:Pb and Br:Pb ratios associated with the loss of univalent cations and PbX₂-formation is seen in XPS valence band spectra normalized to Pb 5d states, as shown in Figure 11c, which is supported by the DFT calculations of CH₃NH₃PbI₃ and CH₃NH₃PbBr₃.

XPS can offer valuable details about the chemical and elemental composition of the surface of organic and perovskite materials. The ability of XPS to provide chemical and elemental information about the surface of the material being studied is one of its key advantages. Thus, it is an excellent tool for identifying degradation byproducts and comprehending the degradation mechanisms. XPS can also analyze conducting and non-conducting materials, which is useful for studying degradation in perovskite solar cells since they typically have nonconductive layers. Furthermore, since XPS is a nondestructive method, it enables repeated measurements on the same sample, which makes it useful for examining degradation over time. Utilizing XPS to examine solar cell degradation, however, also has some drawbacks. The analysis's generally shallow depth constrains the ability to study degradation across the bulk of the material. This can be especially problematic for thick films or multilayer structures. XPS analysis can be costly and time-consuming due to specialized tools and knowledge requirements. Furthermore, XPS calls for a high vacuum environment, which may not be suitable for some materials, such as those that are vacuum-sensitive or prone to outgassing. Alternative techniques, such as FTIR or Raman spectroscopy, may provide complementary information about the surface chemistry of these materials. Therefore, it is important to consider the advantages and limitations of each technique and choose the most appropriate one for the specific research question.

2.1.12. Fourier Transform Infrared (FTIR) or IR Spectroscopy

Fourier Transform Infrared (FTIR) spectroscopy uses infrared (IR) radiations incident on the material under investigation. Some incident radiation is absorbed, while others are

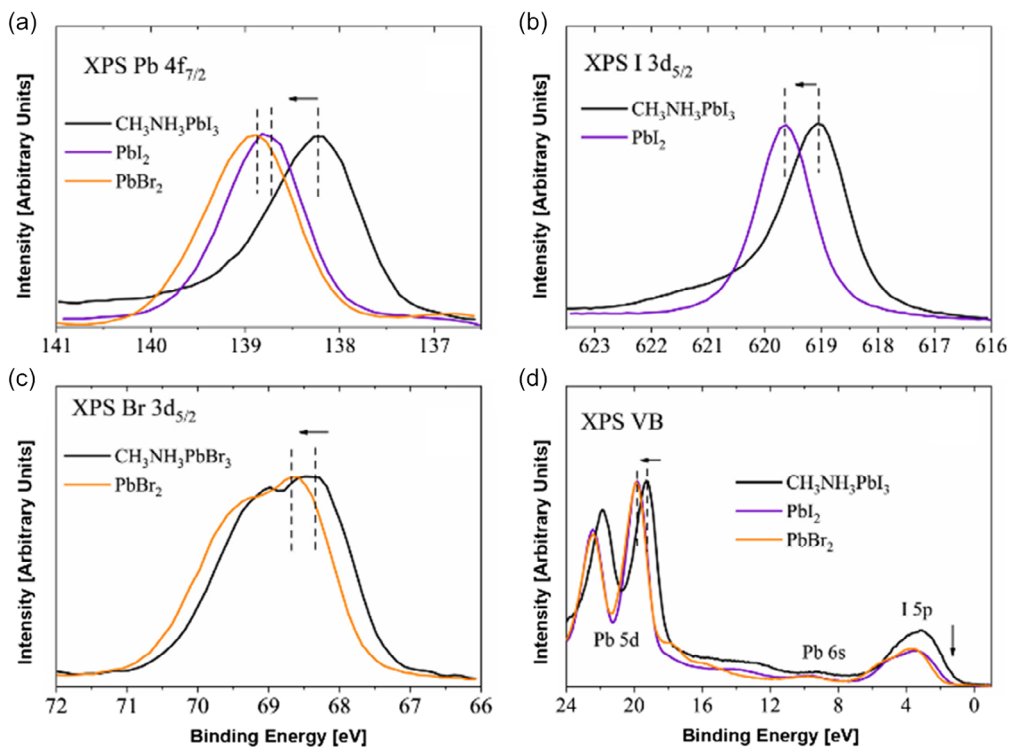


Figure 11. a) XPS Pb 4f, b) I 3d, c) Br 3d, and d) VB spectra of $\text{CH}_3\text{NH}_3\text{PbI}_3$, PbI_2 , and PbBr_2 . Reproduced with permission.^[174] Copyright 2021, Elsevier Inc.

transmitted through the sample and collected at the detector. The spectrum produced is often referred to as the molecular fingerprint of the sample. It contains peaks representing the bonds within the molecules of the material and, by extension, its chemical structure. FTIR spectroscopy is a handy tool to obtain structural insight (functional groups, bond stretching, and bond deformation) into a material since it generates spectra with well-defined patterns.

Due to the potency of this technique, Shah et al.^[175] used it to study the degradation pathways in OSCs. They identified atomistic and vibrational mode changes in OSCs during degradation in the presence and absence of light, oxygen, or ambient air. Using the low bandgap polymer PTB7 films and its PTB7:PCBM blend, they found a significant increase in the absorption at 1727 cm^{-1} , attributed to the increase in C=O modes. They also observed a broad increase at 3240 cm^{-1} , attributed to the hydroxyl (OH) groups of the polymer chain. In the absence of oxygen and moisture, the light-induced degradation of OSCs did not show any significant changes in their IR active modes, similar to films exposed to ambient air in the dark. However, after light soaking, they observed small changes in P3HT:PCBM blends around 2500 cm^{-1} due to the locally induced H-motion arrangements.

Many studies have also used FTIR to study the structure and functional groups of perovskites.^[176–178] Recently, Darkhan et al.^[179] studied the degradation of the perovskite thin film ($\text{CH}_3\text{NH}_3\text{PbI}_{3-x}\text{Cl}_x$) in the presence of different stressors using FTIR and SEM. **Figure 12** shows the FTIR spectra of the freshly prepared samples versus degraded ones either in air (Figure 12a),

by irradiation (Figure 12b), or in a nitrogen atmosphere (Figure 12c). They found stressor-dependent degradation of the functional perovskite layer. The strongest vibrational modes, which correspond to the symmetric and asymmetric N-H stretching modes (associated with NH_3^+), were seen in the fresh perovskite thin film at frequencies of 3132 and 3179 cm^{-1} .^[179] The fresh films did not exhibit any feature, pointing to O-H stretching vibrations in the 3400 – 3700 cm^{-1} that would suggest the presence of a functional hydroxyl group (hydrates, hydroxide, and water).^[179] The perovskite film was exposed to $50 \pm 5\%$ RH. When exposed to the atmosphere, the N-H stretching mode shifts toward higher frequencies, and the NH_3^+ band widens (as shown by the blue curve of Figure 12a). The N-H vibrational peak at 3200 cm^{-1} expanded and shifted simultaneously, suggesting a hydration-induced degradation of the perovskite film. New absorption peaks at 1660 and 1497 cm^{-1} appeared, indicating another sensitive aspect of the hydration process. N-H and O-H bonds were bent in the dominant peak at 1660 cm^{-1} , while O-H and N-H bonds were stretched in the dominant peak at 1497 cm^{-1} . Peaks at 910 and 1248 cm^{-1} (CH_3NH_3^+ rock) shifted to 935 cm^{-1} and 1255 cm^{-1} , respectively. Also, the peak at 961 cm^{-1} (C-N stretch) shifted to 990 cm^{-1} due to the destruction of the crystalline structure.^[179] The deprotonation of CH_3NH_3^+ , caused by hydration, forms new chemical bonds within the perovskite crystal structure. In a nitrogen environment, the chemical bonds of the crystal structure are maintained. However, due to hydration, the NH_3^+ band expands in the ambient atmosphere, shifting toward higher frequencies in the N-H stretching mode. Finally, they showed that the stability and

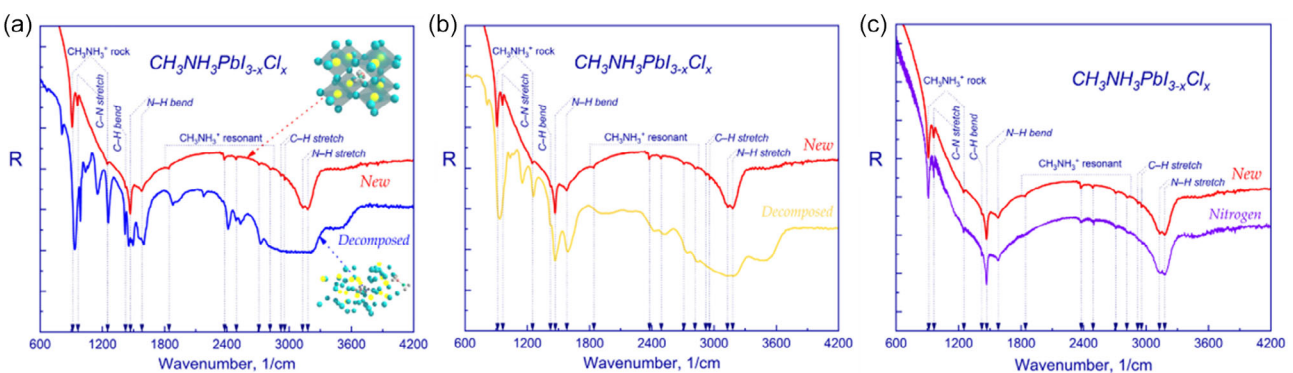


Figure 12. FTIR spectra of $\text{CH}_3\text{NH}_3\text{PbI}_{3-x}\text{Cl}_x$ single crystal samples: a) as-cast (red) and degraded (blue) perovskite film, b) as-cast (red) and exposed to illumination (yellow), and c) as-cast (red) and exposed to nitrogen (purple). Reproduced with permission.^[179] Copyright 2023, MDPI.

efficiency of PSCs can be adversely affected by the dissociation of water molecules in the presence of sunlight.

FTIR is nondestructive, making it useful for tracking degradation over time. Its ability to detect functional groups within the material is one of the main advantages of FTIR. This is crucial in recognizing degradation byproducts and understanding their mechanisms. Furthermore, FTIR is a fast and affordable tool, which makes it a viable option for routinely characterizing solar cell degradation. However, this technique has the disadvantage of being limited by depth profiling and has low sensitivity, making it challenging to detect low levels of degradation byproducts.

2.2. Devices

The next sections described tools mainly used to monitor changes in the device parameters of OSCs and PSCs due to degradation agents. The devices are primarily full solar cell stack or charge carrier-selective devices for probing degradation phenomena, charge transport dynamics, recombination dynamics, charge carrier density, generation, extraction, etc. the structure of OSCs or PSCs is usually a photoactive layer sandwiched between two electrodes with transport/interfacial layers before each electrode. Since the devices are primarily full cell stacks, the interfacial properties between the active layer and electrodes are important in limiting or exacerbating the degradation.^[180–182] Therefore, the interfacial layers, such as the electron transport layer (ETL) and hole transport layer (HTL), play an important role in terms of energy level alignment, defects passivation, and improvement in charge carrier extractions.^[181,183–186] Various strategies are introduced to improve device stability, such as carbon-based perovskite solar cells and cross-linkable organic ligands.^[187,188] Most tools mentioned in this article can be utilized to study the impacts of interfacial engineering by adding or changing the materials^[97,104,189,190] on degradation and stability. Some of these studies on device stack are mentioned above. Others are discussed in the rest of the sections.

2.2.1. J-V Characteristics: Performance of PV Parameters over Time

The current density–voltage (*J*–*V*) characteristic is a straightforward but effective tool for assessing the performance of solar

cells.^[92] The power conversion efficiency (PCE) is determined by measuring J_{SC} , V_{OC} , and FF. These parameters can be monitored over time to investigate stability and degradation mechanisms. It can provide preliminary information on which parameter limits efficiency, leading to follow-up experiments to better understand the various degradation mechanisms. The lifetime of a solar cell can be obtained from the decay curve of its PCE over time. As mentioned earlier, protocols to study and test stability were established in the scientific community for both OSCs and PSCs.^[31,35] A typical degradation curve has two parts: a fast nonlinear decay region called burn-in and a slow-extending degradation regime.^[191,192] The burn-in regime can be considered a major contributor to the lifetime. In general, the lifetime of solar cells is reported using T_{80} , which is the time for PCE to reduce 80% of the initial value.^[191,192]

Several studies have shown different OSC and PSC stability curves over the years.^[33,193,194] Usually, they show a shape as described above (a burn-in and slow-extending degradation regimes). Xiaoyan Du et al.^[195] investigated the stability of OSCs based on nonfullerene acceptors (IT-4F) with different donor materials (PBDB-T, PM6, and PM7), and the *J*–*V* characteristics are shown in Figure 13. The devices were kept under dry nitrogen with oxygen and water levels below 0.5 ppm and under white LEDs illumination. In Figure 13a, the PBDB-T-based device shows less change in the *J*–*V* curve for 1,450 h, while the *J*–*V* curve of PM6-and PM7-based devices in Figure 13b,c indicates relatively drastic changes, particularly in FF. Figure 13 d shows each parameter of all three devices as a function of time. Interestingly, J_{SC} and V_{OC} are fairly stable in all three devices. However, the burn-in loss in the FF is the primary cause of the degradation in PCE. While the stabilized FF of PBDB-T-based devices remained above 90% after 1,400 h illumination, the FF of both PM6- and PM7-based devices decreased continuously to about 80%. T_{80} is estimated to be less than 1,300 h for PM6- and PM7-based solar cells, which is significantly less than that of PBDB-T-based devices (estimated to be over 11 000 h). PSCs show similar degradation behavior curves as OSCs. However, much better lifetimes have generally been reported for thousands of hours to days and months.^[196,197]

Huang et al.^[198] studied new fluorinated fullerene materials as an ETL to improve the photostability of PSCs. They reported robust unencapsulated devices with a 1920 h lifetime under

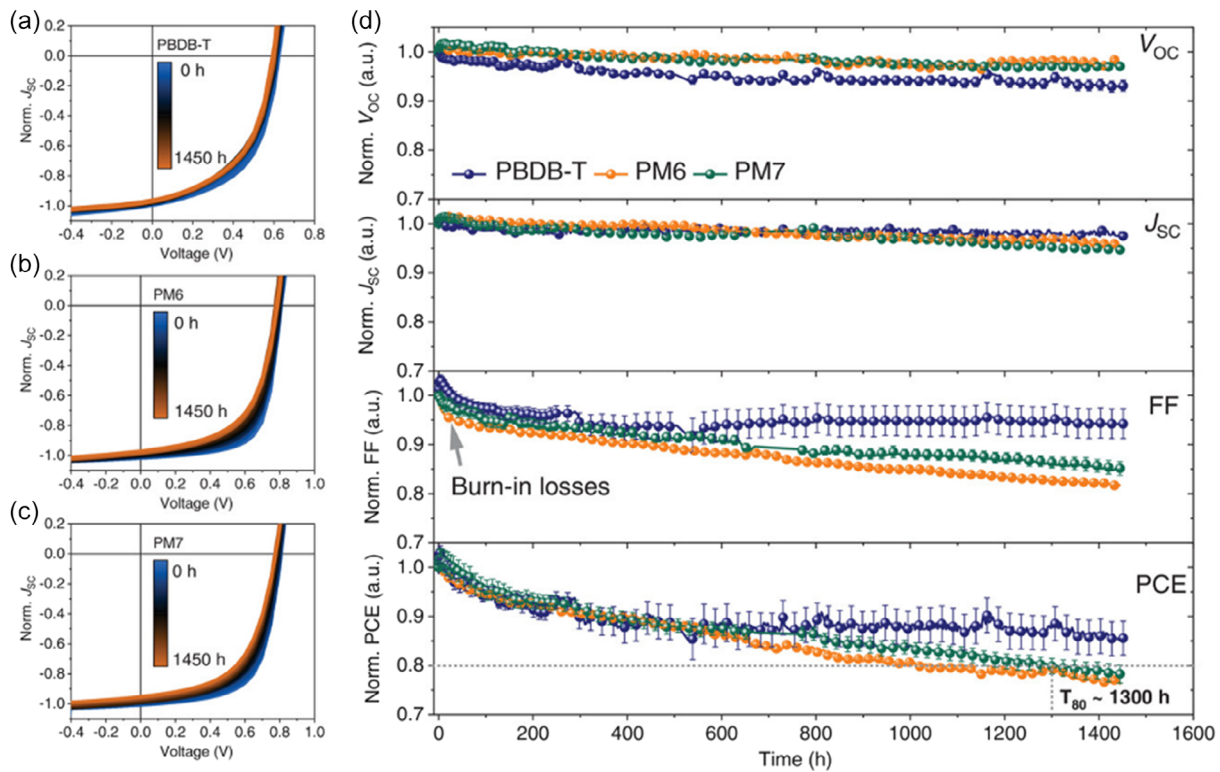


Figure 13. Photostability of PBDB-T, PM6, and PM7 blended with IT-4F devices under continuous LED illumination and room temperature. a–c) Recorded current-voltage curves and d) PV parameters against time. Lifetime (T_{80}) for PM6- and PM7-based solar cells. Reproduced with permission.^[195] Copyright 2020, Wiley-VCH.

constant illumination. Furthermore, a thermal stability test was conducted in the inert condition with different temperatures. The T_{80} lifetime of the CsFAMA-based device was estimated to be over 1050 h at 80 °C, 2323 h at 75 °C, and 3919 h at 65 °C, respectively. As a result, they estimated the lifetime of the encapsulated device would approach 10 years. Thus, each J - V stability curve encompasses its properties or characteristics. They help approximate the underlying degradation mechanism/cause and inform further investigations into specific stability study directions.

2.2.2. J - V Characteristics: V_{oc} , J_{sc} Light Intensity Dependence

Light intensity-dependent studies in both OSCs and PSCs could reveal the recombination dynamics in solar cells, such as radiative or nonradiative recombination. The ideality factor derived from the dependence of V_{oc} on the light intensity is used to assess the recombination losses in solar cells. The slope of the V_{oc} versus different illumination intensities, nKT/q , is a characteristic feature of the recombination mechanisms.^[199] The presence of more traps in the system is indicated by a higher dependence of V_{oc} on light intensity. Therefore, if $1 < n < 2$, trap-state-induced nonradiative recombination is dominant, whereas $n \sim 1$ means radiative bimolecular recombination is dominant. The slope associated with the J_{sc} versus light intensity (as in $J \sim I^\alpha$) curve can also be used to estimate the degree of

radiative recombination.^[200] The α value ≈ 1 is identical to suppressed radiative recombination.^[200]

Zhao et al.^[201] studied the recombination mechanisms in PM6:Y6-based OSC devices through the light intensity dependence of the J_{sc} and V_{oc} . The α values of devices after 1 h illumination compared to the fresh sample decreased, as shown in Figure 14a.^[201] The results reveal that photo-degradation increases radiative recombination in aged PM6:Y6-based devices. Figure 14b shows the V_{oc} light intensity-dependent analysis. If radiative recombination governs, the parameter n reflects the presence of trap states across the active layer or at the device interfaces, with a slope close to kT/q (thus, $n = 1$). After 1 h of illumination, the n values of the fresh and degraded devices without a filter and those with UV or B filters increased. The V_{oc} of the device with the B filter is less light intensity dependent. Given that the effect of the blue filter is significant, it is clear that short-wavelength lighting stimulates nonradiative recombination in the device.

Mahapatra et al.^[202] investigated the electrical characteristics of MAPBi₃-based PSCs with aging time. The devices were stored under ambient conditions with 20% of RH in the dark for 94 h. Light-dependent photovoltaic parameters were measured to study the charge extraction and recombination, as shown in Figure 14c,d. Slope values of α decreased from 0.95 to 0.91 after 94 h of storage, indicating that the charge extraction of devices reduced with radiative recombination. Figure 14d shows that the light intensity dependence of V_{OC} and the ideality factor

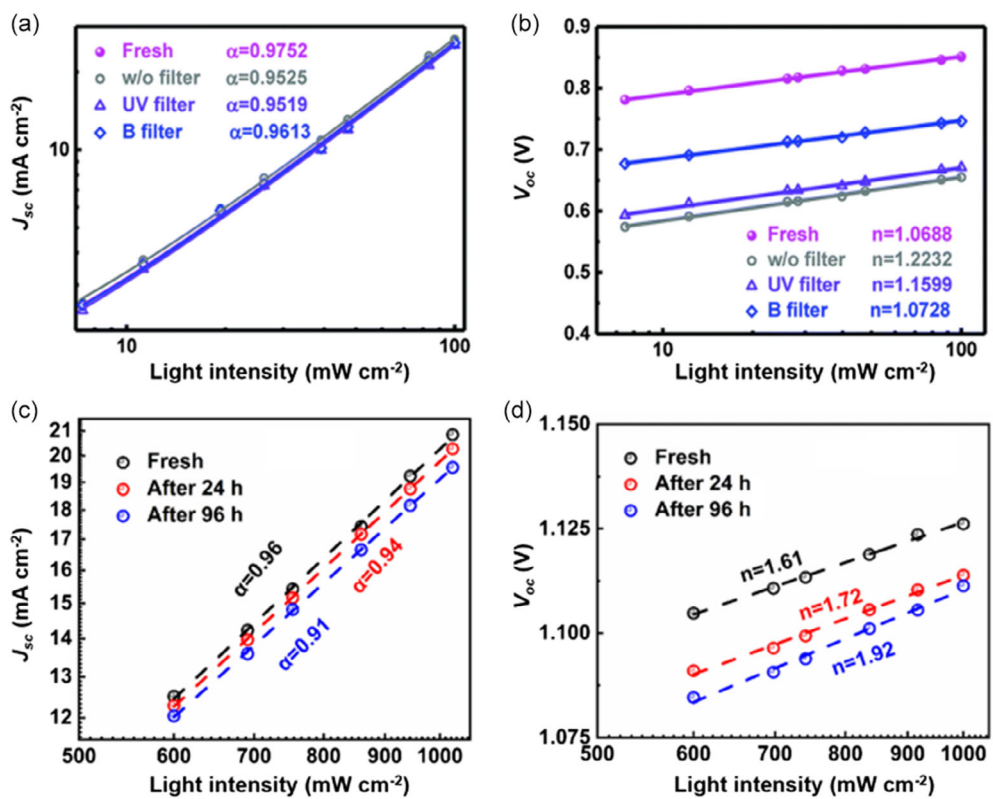


Figure 14. Light intensity dependence of a) J_{sc} and b) V_{oc} of both the fresh OSC devices and the degraded devices without a filter, with a UV filter, or with B(blue) filter under 1 h of illumination. Reproduced with permission.^[201] Copyright 2021, The Royal Society of Chemistry. c) J_{sc} and d) V_{oc} of PSC devices stored under ambient conditions for 96 h with reverse scanning in the investigated devices. Reproduced with permission.^[202] Copyright 2020, MDPI.

(n) for each device were calculated as 1.61, 1.72, and 1.92 for the fresh and aged devices for 24 and 96 h, respectively. The ideality factor increased nearly to 2 as the devices degraded, demonstrating that trap-assisted recombination became dominant in the aged device. As a result, the device performance degraded from 17.32% to 14.97% after 96 h storage, significantly affected by the decrease of the FF.

Light intensity dependence V_{oc} and J_{sc} is a simple and fast measurement technique that informs about factors limiting device performance, such as series resistance, shunt resistance, and recombination losses. However, it does not provide detailed information about the underlying fundamental mechanisms for such factors. This means it is often used with tools such as TR-PL, TAS, XPS, FTIR, NMR, etc., to elucidate either degradation stressor-induced chemical, physical, or electronic mechanisms.

2.2.3. J-V Characteristics: Space-Charge-Limited Currents

The space-charge-limited currents (SCLCs) technique is a powerful technique that has proven invaluable in determining the steady-state mobility of organic semiconductors.^[203] SCLCs are observed in devices that inject only electrons or holes into a semiconductor, known as electron- or hole-only devices. In such devices, the accumulation of space charges restricts the maximum current that can be allowed electrostatically. In this regime, the current is dominated by charge carriers injected

from the contacts, and the J-V becomes quadratic. The current only depends on mobility and not anymore on charge carrier density. Thus, the mobility can be estimated from a simple J-V measurement. For assessing better-performing devices and also changes in mobilities due to degradation stressors, the notion of the ratio of mobilities (μ_e/μ_h , or μ_e/μ_h , or simply μ_{max}/μ_{min}) can be introduced. This notion gives an idea of charge carrier balance in the cells. A ratio of 1 means balanced charge carriers, while a ratio >1 indicates an imbalance of charge carriers in the cells. This signature can be used to assess changes in mobilities due to degradation.

Yang et al.^[204] studied the thermal stability of OSCs as a function of the active layer thickness. The charge carrier mobilities in fresh and aged films of three different thicknesses were plotted using SCLCs by fitting the J-V characteristics of electron- and hole-only devices to the Mott-Gurney equation (Equation (6)). Based on the characteristics of the materials and devices, the Murgatroyd equation (Equation (7), i.e., modified Mott-Gurney) is used. The hole and electron mobilities of the relevant fresh and aged blends were evaluated using the J-V characteristics of single-carrier devices. Based on the fitting to the experimental results, the electron mobilities (μ_e) and hole mobilities (μ_h) of fresh and aged films are calculated for different blend thicknesses from 30 to 150 nm. The mobilities of the aged thick devices (active layer thickness of 110 and 150 nm) decreased compared to those of the fresh devices. In contrast,

the mobility of the aged devices with a low thickness of 30 nm increased after 150 °C continuous heating. As a result, they proposed that thermal stability increases gradually as the active layer thickness decreases.

$$J_{SCL} = \frac{9}{8} \epsilon_0 \epsilon_r \mu \frac{V^2}{L^3} \quad (6)$$

$$J_{SCL} = \frac{9}{8} \epsilon_0 \epsilon_r \mu \exp\left(\frac{0.89x\beta\sqrt{V_{in}}}{\sqrt{L}}\right) \frac{V^2}{L^3} \quad (7)$$

Though lowering the μ_e and μ_h in the device may indicate degradation, it does not provide a mechanistic understanding. Using the notion of the ratio of mobilities μ_{max}/μ_{min} gives a clearer picture. For example, some studies used the μ_{max}/μ_{min} to demonstrate an imbalance in charge mobilities upon degradation, reflected in the observed fast degradation in the FF of the devices, linked to the increase in recombination to extraction rate.^[205,206]

There has been an erroneous interpretation of SCLC data for PSCs, especially in the interpretation of the curves themselves and determining the density of trap states from the trap-filled limited voltage (V_{TFL}) over the years, as depicted in Figure 15a–e.^[207–211] This is because hybrid perovskites possess electric and ionic conduction properties, requiring a different understanding than conventional semiconductors. The presence of these mobile ion species has the potential to significantly influence total electronic current injection, transport, and extraction, thereby leading to an over(under)-estimation of the phenomena using the traditional characteristics. Several studies that focus on measuring space-charge-limited currents (SCLCs) in perovskite single crystals and thin films overlook the impact of factors such

as mobile ions, permittivity, and temperature on the behavior of the current–voltage curve.^[203,212]

However, hybrid perovskites exhibit electric and ionic conduction properties, so the interpretation must differ from conventional semiconductors. Therefore, pulsed SCLC measurements proposed by Duijnste et al.^[213,214] must be considered when characterizing the SCLCs.^[213,214] Figure 15f shows the J – V curve from the SCLC measurement of a MAPbBr₃ single crystal, which makes strong hysteresis between the forward and reverse scans. Next, Le Corre et al.^[212] demonstrated that ion movement strongly affects current in the SCLCs analysis when studying perovskites. Figure 15g shows a simulation of a 160 μ m thick perovskite single crystal with trapping and mobile ions to gain insight into how the ions affect the current. A steady-state scan simulation is performed, with ions having time to redistribute at every voltage step. This is followed by simulations of the extreme cases of infinitely fast forward and reverse scans pre-biased at 0 and 200 V, respectively. The ion distributions throughout the device are calculated at pre-bias and kept fixed for all subsequent voltage steps in these scans. As a result, while no significant difference exists between the forward and steady-state scans, a significant hysteresis can be seen for the forward and reverse scans. This result seeks to correct the erroneous interpretation of the SCLC experimental curve and determination of the V_{TFL} for PSC-based electron-only or hole-only diodes. A recent study by Sun et al.^[215] showed the beginning of this new understanding as depicted in Figure 15h. SCLC is a relatively simple and easy-to-perform experiment with the standard J – V characterization tool, which can provide valuable information about charge carrier mobility and the density of states in devices. Therefore, it can be used to determine the carrier lifetime and diffusion

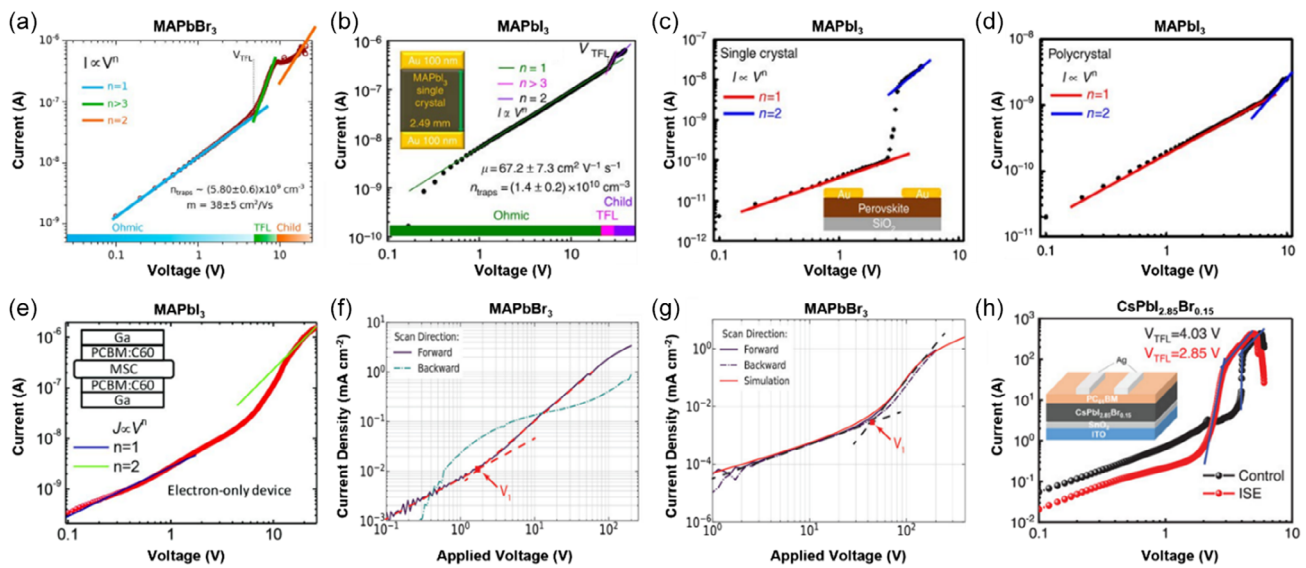


Figure 15. The dark J – V characteristics of perovskite-based devices. a) MAPbBr₃ (at 300 K). Reproduced with permission.^[207] Copyright 2015, American Association for the Advancement of Science. b) MAPbI₃. Reproduced with permission.^[208] Copyright 2015, Macmillan Publishers Limited. c) Single crystal MAPbI₃, d) polycrystal MAPbI₃. Reproduced with permission.^[209] Copyright 2017, Springer Nature. e) MAPbI₃. Reproduced with permission.^[210] Copyright 2015, American Association for the Advancement of Science. f) The forward and reverse J – V scan of a MAPbBr₃ perovskite single crystal showing strong hysteresis. Reproduced with permission.^[213] Copyright 2020, American Chemical Society. g) Pulsed SCLC J – V curves of a 160 μ m thick MAPbBr₃ perovskite single crystal with the corresponding drift-diffusion fit. Reproduced with permission.^[212] Copyright 2021, American Chemical Society. h) Electron-only device of CsPbI_{2.85}Br_{0.15}. Reproduced with permission.^[215] Copyright 2023, Wiley-VCH.

length, which are crucial parameters in solar cells. However, it does not provide specific information about the effect of defects or impurities and may cause sample degradation due to high electric fields.

2.2.4. External Quantum Efficiency

The external quantum efficiency (EQE) of a device is the number of electrons extracted from the solar cell under operating conditions divided by the number of photons incident on the solar cell. It is also referred to as incident photon-to-current efficiency (IPCE). In an ideal solar cell, every photon would generate an electron-hole pair, and all these carriers would move toward the depletion region, where they will be separated and collected. EQE is typically used to accurately calculate the integrated current of a solar cell to ascertain the J_{sc} from the $J-V$ characteristic rather than to monitor degradation. It is relatively simple and easy to perform, requiring only basic equipment and materials. It serves as a reliability measure of the measured J_{sc} . If the difference between the current density calculated from the EQE and J_{sc} is more than 5%, then the J_{sc} from the $J-V$ characteristics loses credibility. However, when it comes to monitoring degradation, EQE can be particularly effective in analyzing the current degradation mechanism. However, EQE measurements can be affected by various experimental factors, including the spectral response of the light source, the angle of incidence of the light, and any misalignment in the measurement setup.

Figure 16a shows the EQE spectrum as a function of wavelength to illustrate the air effect in the burn-in thermal degradation of OSCs, as illustrated under the AFM section.^[138] The EQE of the degraded device with air clearly shows a more severe reduction in the spectrum and peak intensities, consistent with a lower J_{sc} of the degraded device in the air from the $J-V$ characterization measurement. In addition, the change in absorbance of the aged devices was small. At the same time, EQE showed degradation in the current, indicating that the degradation is

related more to charge generation and extraction than absorption. The EQE absorption tails are shown in Figure 16b. This tail was described as the Urbach tail and used to determine the Urbach energy using the following equation

$$EQE(E) \propto \alpha(E) \propto \exp\left(\frac{E}{E_U}\right) \quad (8)$$

where α , E , and E_U are the light-absorbing coefficient, photon energy, and estimated Urbach energy, respectively. The UE indicates the energetic disorder at the D:A interface. The UEs of the devices were determined, and the degraded device has a higher energetic disordered active layer due to the burn-in. They concluded that the decrease in EQE is due to poor energy transfer, described by the influence of the higher energetic disorder in the active layer with higher trap states and, thus, charge carrier recombination.

Song et al.^[216] showed some exciting results on the degradation of PSCs combining EQE and laser beam-induced current imaging (LBIC). Figure 16c depicts the hydration–dehydration cycles. The decrease in EQE observed in $80 \pm 5\%$ RH within the first hour can be recovered entirely in dry air conditions within 3 h. Four different stages are introduced, three of which denote the reversible states even after the device decay, and the fourth stage represents an irreversible state. The first and second stages were explained as being determined by the charge carrier recombination and hole mobility at interfaces between the interfacial layer and perovskite film. The third and fourth stages were due to the reactions between water and the perovskite material and the subsequent reactions and phase transformations. Figure 16d depicts LBIC EQE maps of a hydrated perovskite device upon dry air purging. The EQE spectrum recovers with time under dry conditions. As a result, the hydration–dehydration cycle can be repeated several times without significant loss of the current generation. However, excessive exposure times or higher H_2O vapor pressures could cause irreversible damage as it enters the fourth stage.

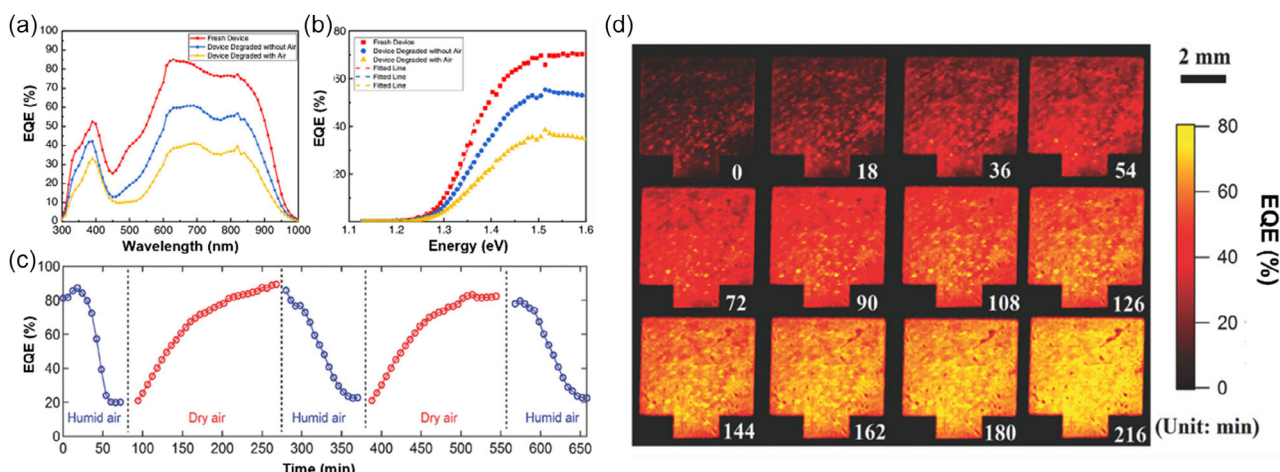


Figure 16. a) EQE spectra as a function of wavelength, and b) EQE spectrum tail versus the incident photoenergy for the fresh and + degraded device without air and the degraded device with air. Reproduced with permission.^[138] Copyright 2020, American Chemical Society. c) LBIC EQE maps of a hydrated perovskite device while purging with dry air. d) Areal average EQE (at 532 nm) of the perovskite device during hydration-dehydration cycles. Reproduced with permission.^[216] Copyright 2016, Wiley-VCH.

2.2.5. Impedance Spectroscopy

Impedance spectroscopy is a versatile materials characterization technique that monitors electrical and electrochemical processes in materials. It is also used in the profiling of electrochemical and solid-state devices. A small sinusoidal signal is used in impedance spectroscopy to probe a material. The sample's response to the stimulus is measured as a function of frequency. Depending on the probed characteristic features, the device can either dissipate or store the electrical excitation energy. The difference in the dynamics or relaxation processes can easily be spotted if the relaxation time (τ) is unique. τ is the time the device takes to reach equilibrium after excitation. The resulting information from the measurement can be extracted and processed using equivalent circuit models (ECM).^[217] For impedance spectroscopy studies on perovskite materials and PSCs, Guerrero et al.^[218] recently published a detailed review, including different data analysis methods, which we believe can be very helpful.

Several studies have explored the use of this technique to study the electrochemical processes in OSCs. Osorio et al.^[219] analyzed the degradation of encapsulated and unencapsulated ITO/TiO₂/PTB7:PC₇₀BM/V₂O₅/Ag cells under ambient conditions. Figure 17 shows the Cole–Cole plots of the encapsulated (a–c) and unencapsulated (d–f) devices under AM1.5 illumination at different bias voltages. They analyzed the spectra using

resistive/capacitive equivalent circuits. The solid curves represent the best fit for each measurement. They found that the contact layers are the most sensitive layers inside the device. The typical arc or semicircular shape for impedance spectroscopy spectra is observed in the plots. Deviations from the perfect semicircular shape of an RC circuit suggest the presence of different RC species in the spectra. The average radius of the arcs for the unencapsulated devices also increased faster with increasing storage time, indicating that unencapsulated devices attained higher impedance values than encapsulated devices over time. Notably, the radii of both devices decreased with an increase in the applied bias voltage, suggesting that charge extraction is somewhat efficient in both devices.

One of the major advantages of impedance spectroscopy is its ability to provide the necessary information about the electronic and ionic transport properties of devices. This helps us understand how degradation affects charge transport and recombination in these devices. Like most characterization tools above, this tool is nondestructive, allowing repeated measurements on the same sample. However, the somewhat complex nature of the technique requires specialized tools and knowledge. The frequency range, measurement conditions, and physical properties of the solar cell are just a few examples of the many variables that can affect the impedance spectra, making it sometimes difficult to obtain and interpret the results. Another disadvantage is the need for careful sample preparation for analysis since the

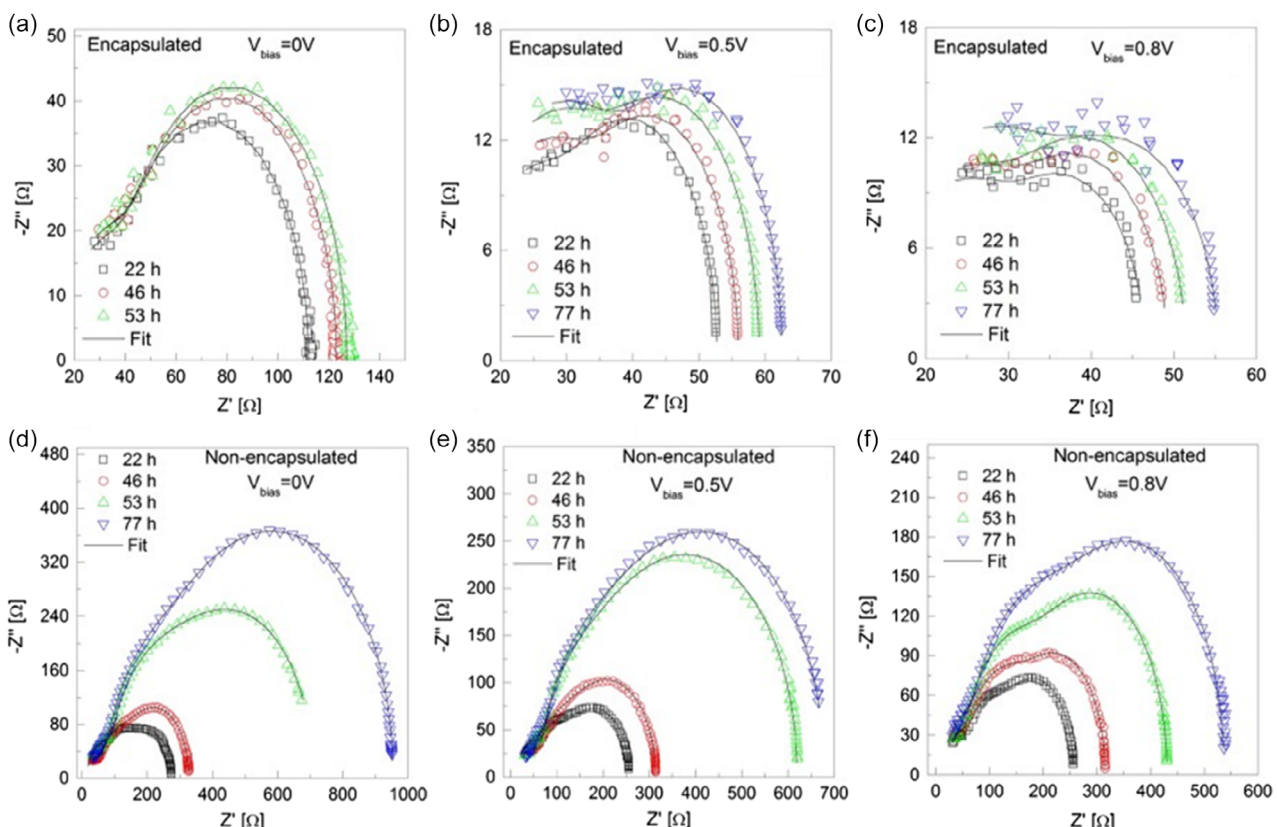


Figure 17. a–c) Cole–Cole plots of the encapsulated and d–f) unencapsulated OSCs taken at three different V_{bias} : a,d) 0 V, b,e) 0.5 V, and c,f) 0.8 V. The experimental data were fitted using the 3RC circuit model (solid lines). Reproduced with permission.^[219] Copyright 2017, The American Chemical Society.

interface between the solar cells and the electrodes can significantly impact the results. Additionally, variables like temperature, humidity, and light exposure can influence impedance spectroscopy measurements, a challenge for comparing results obtained under different conditions.

2.2.6. Cyclic Voltammetry

Cyclic voltammetry (CV) is a valuable technique for studying electrochemical and oxidation processes in molecular samples. This technique is also helpful in studying electron transfer-initiated chemical reactions, including catalysis.^[220] A key advantage of CV is its relatively simple instrumentation and use as a nondestructive tool to probe the energetics and kinetics of electron transfer reactions in OSCs and PSCs. The information obtained from CV provides insight into the effects of degradation on the electron transfer processes within the devices. However, CV response is often affected by the scan rate, the presence of other electroactive species, and the potential range. This makes the interpretation of the results difficult. Additionally, one needs to be careful in measurement as the quality of the surface of the electrode significantly impacts the results. Thus, sample preparation for analysis must be done diligently. Yang et al.^[221] investigated the electrochemistry of $\text{CH}_3\text{NH}_3\text{PbI}_3$ in an organic electrolyte by CV. They discovered that the oxidation of iodide ions and the reduction of lead ions within the perovskite crystal cause the degradation of the material. A phase change is initiated in the perovskite's crystal structure due to this electrochemical reduction, which joins forces with the reduction in the conduction band to reduce lead ions to metallic lead further. The valence band of $\text{CH}_3\text{NH}_3\text{PbI}_3$ and the iodide ions lose electrons. The perovskite's electrochemical reactions produce iodine, which diffuses into the organic electrolyte. They proved that $\text{CH}_3\text{NH}_3\text{PbI}_3$ is a highly reactive electrochemical compound. As a result, stability can be increased if suitable methods for limiting the irreversible phase changes brought on by the oxidation of lead ions are used.^[205]

Kerner et al.^[222] also used CV to examine the chemical reactivity at the methylammonium lead triiodide/gold interface (MAPbI_3/Au). They demonstrated that indium tin oxide

(ITO)/ MAPbI_3/Au reaction peaks indicate that the electrochemical stability is between -0.5 and 0.9 V. They noticed hysteresis, irreversible electrochemical peaks, switchable perovskite diode polarity, and permanent degradation at higher voltages. When low leakage current devices are subjected to cyclic voltammetry (CV) measurements, Figure 18 demonstrates that an electrochemical current peak appears when the bias voltage rises above a threshold of less than -0.5 V or greater than $+0.9$ V. The electrochemical stability window of this device, based on the threshold voltages in Figures 18a,b, is between -0.5 and 0.9 V, significantly lower than the voltages frequently used to describe lateral devices. If the device is within this window, the CV characterization is stable at a scan rate of 1 mV s^{-1} for more than 10 h. However, when the voltage range is extended to much more negative voltages (i.e., -1.2 V) than the negative electrochemical threshold voltage and to only very slight positive biases (i.e., $+1.0$ V), the device degrades quickly. The main reaction/degradation mechanisms at voltage are inferred to be I_2 , I_3 , and Au^+ formations. CV is a valuable tool for studying the redox behavior of OSCs and PSCs. However, its limitations, in terms of its sensitivity to electrode preparation and measurement conditions, should be considered when deploying it to probe degradation mechanisms in these devices.

2.2.7. Kelvin Probe Force Microscopy

Also commonly referred to as surface potential microscopy, the KPFM is another electrochemical characterization technique just like Cyclic voltammetry (CV) used to characterize the surface potential of nanometer-size materials. There are two modes of operation for Kelvin probe force microscopy (KPFM): amplitude-modulated KPFM and frequency-modulated KPFM. Its principle of operation closely follows that of the atomic force microscope (AFM). However, it only operates in noncontact mode.^[223] This mode of operation is beneficial in the characterization of OSCs and PSCs. It is established that water, oxygen, illumination, and electron beam irradiation cause degradation in these devices. KPFM can simultaneously identify the work function of a sample at the nanometer scale and visualize the sample topography. The sample's composition, electronic state,

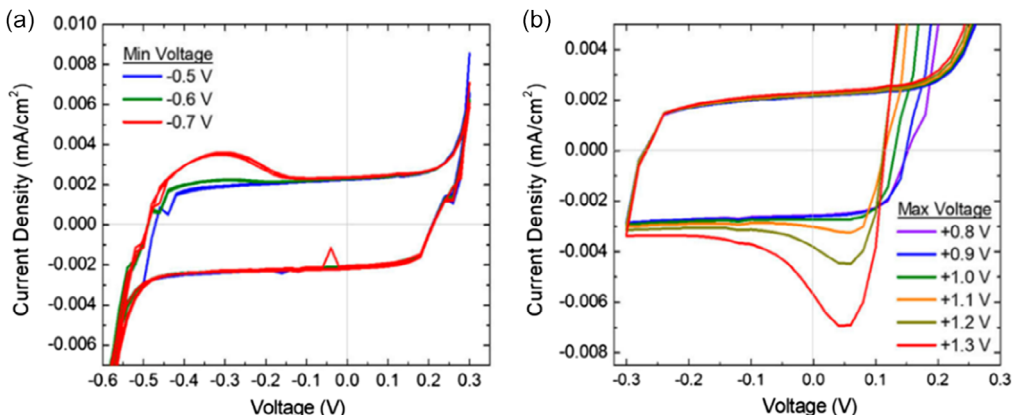


Figure 18. Cyclic voltammetry of ITO/ MAPbI_3/Au peaks showing the a) negative and b) positive threshold at a scan rate of 100 mV s^{-1} . Reproduced with permission.^[242] Copyright 2019, AIP Publications.

energy band-bending, charge trapping, and surface reconstruction can all be studied more easily. These properties relate to the device's contact potential difference (CPD) and surface photovoltage. The relationship shown below allows for the CPD to be determined.

$$CPD = \frac{\phi_{\text{tip}} - \phi_{\text{sample}}}{e} \quad (9)$$

where ϕ_{tip} is the work function of the probe's tip, ϕ_{sample} is the work function of the sample, and e is the electronic charge.^[222]

In perovskite and Cu(In, Ga)Se₂ solar cells, Lanzoni et al.^[224] investigated the impact of environmental factors on grain boundary bending using KPFM in various operating modes. They demonstrated how the work function of typical solar cell absorbers, such as Cu(In,Ga)Se₂ and CH₃NH₃PbI₃, is vulnerable to measurement artifacts at grain boundaries when measured with amplitude-modulation KPFM, by far the most common KPFM measurement mode. The cantilever-sample distance fluctuating on flawed samples is the primary cause of this. Due to the polycrystalline nature of the absorbers, frequency modulation KPFM measurements on nonair-exposed Cu(In,Ga)Se and perovskite absorbers show that the amount of band bending measured at the GB is negligible and facet-related contrast predominates the electronic landscape of the semiconductor surface.

To precisely elaborate the crucial role of grain boundaries in mixed perovskite materials ((CH(NH₂)₂PbI₃)_{0.85}(CH₃NH₃PbBr₃)_{0.15}), Yun et al.^[225] used KPFM to identify the local surface potential redistribution due to ion migration, which has an impact on the performance of perovskite solar cells. The CPD in the same region changes under different bias voltages, as depicted in Figure 19a. Figure 19d,e shows that a positive bias

has a smaller effect on CPD change than a negative bias. One could hypothesize that ion migration is responsible for the 720 s of recovery time following removing the bias voltage. Furthermore, as shown in Figure 19b,c, grain boundaries exhibit a more severe change in CPD under large bias than grain interiors, suggesting that grain boundaries are the main channels for ion migration. To learn more about how grain boundaries affect ion migration, KPFM detects the CPD mapping images. According to Figure 19f, a built-in potential brought on by the distinct work functions of TiO₂ and perovskite could separate photo-generated hole-electron pairs under illumination. In the meantime, the clear CPD mapping and outline agree with the earlier discovery that grain boundaries are important for ion migration, indicating band bending close to the grain boundary. Iodine vacancies appear in the conduction band (n-type), and MA and Pb vacancies appear in the valence band (p-type) as a result of ion migration. Meanwhile, the bright CPD mapping and obvious outline are in good agreement with the earlier finding that grain boundaries play a crucial role in ion migration. Iodine vacancies appear in the conduction band (n-type), and MA and Pb vacancies appear in the valence band (p-type) as a result of ion migration, indicating band bending close to the grain boundary. It is important to mention that Kang et al.^[226] reviewed KPFM for characterizing PSCs. The review includes a detailed explanation of the background, working principle, and application of KPFM.

KPFM has major advantages, namely, 1) its ability to probe the local work function and CPD of OSCs and PSCs, leading to an understanding of charge transport and recombination processes within these devices; 2) its high spatial resolution, making it possible to obtain details about the nanoscale electronic properties of OSCs and PSCs, and in part facilitating the understanding of

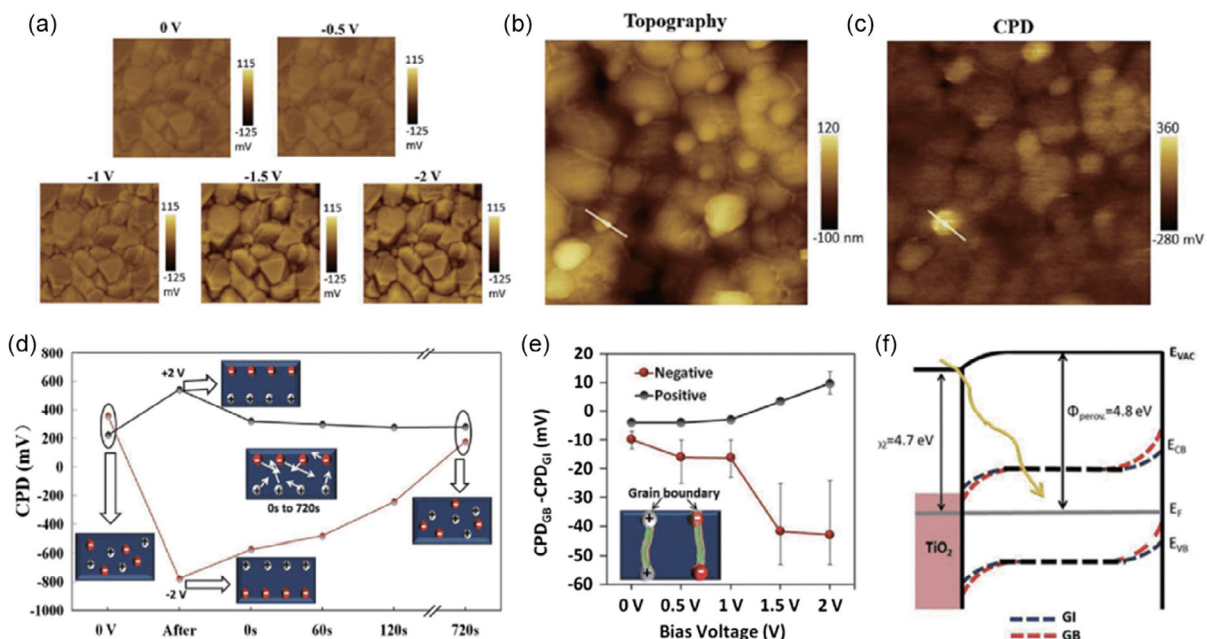


Figure 19. a) Average CPD images under different biases, b,c) topography and CPD mapping under -7 V bias voltage, d) time-dependent average CPD, e) plot of the differences between CPD within the grain interior and at the grain boundary under negative and positive bias voltage, and f) energy band diagram of perovskite and perovskite/TiO₂ interface. Reproduced with permission.^[226] Copyright 2019, Science China Press and Springer Nature.

how degradation affects the local electronic properties of these devices. A significant challenge to KPFM as a characterization tool is the impact of temperature and humidity on the measurements, making it sensitive to measurement conditions. Thus, it is usually used as a supporting tool. Hu et al.^[227] combined KPFM with UV-vis-NIR spectroscopy to monitor the effect of aqueous polyethylenimine (a-PEI) modification in significantly enhancing the stability of nonfullerene OSCs. They investigated ZnO ETL-induced decomposition of nonfullerene acceptors under illumination. They reported an a-PEI-modified ZnO surface that potentially enhances the stability of nonfullerene acceptor-based OSCs. After 8 h of UV illumination, the absorption intensity of the Y6 film on ZnO ETL decreased by 21%, while that of Y6 on ZnO/a-PEI was only reduced by 8%. The latter structure shows superior illumination stability compared to the former. The authors then used KPFM as a function of time to characterize the changes in the work function of ETL films on the ITO substrates with and without UV illumination under ambient conditions for a little over an hour. The work function of both ZnO and ZnO/a-PEI ETLs similarly decreased under 30 min UV illumination. However, after illumination, the work function of the ZnO/a-PEI rapidly recovered compared to pristine ZnO ETL film because of the reabsorption of oxygen. The combined observation led to the conclusion that the photodecomposition of NF acceptor-Y6 by ZnO is suppressed by aqueous PEI modification.

2.2.8. Transient Photovoltaic

Transient photovoltaic (TPV) is a common technique for charge carrier lifetimes in thin-film solar cells such as organic, dye-sensitized, and perovskite solar cells. Given that lifetime frequently depends on the incident light intensity, its applicability to understanding the innate characteristics of a photoactive material or device has been disputed.^[228] To ascertain the photogenerated charge carrier density, the recombination rate constant, and its order, TPV measurements are frequently combined with charge extraction (CE) measurements to extract detailed data on recombination dynamics.^[229] In TPV studies, the test device is initially held and illuminated steadily at open circuit. An additional weak and/or short light pulse is applied to the device, and the resulting voltage transient over a large load resistance is measured. This is done to investigate the recombination lifetime of the excess charge carriers, or the carriers introduced into the device due to the steady-state light bias. In TPV studies, the test device is initially held and steadily illuminated at an open circuit. The device is subjected to an additional light pulse that is weak and/or brief, and the voltage transient that results from a high load resistance is measured.^[230]

Pockett et al.^[231] used TPV and impedance spectroscopy to study the degradation of nonfullerene acceptor OSCs interlayers. The results from their work are presented in Figure 20. For fresh and degraded cells, the charge density, n , was plotted as a function of V_{oc} , as shown in Figure 20a. For fresh cells, they found a good agreement between the calculated charge densities for each interlayer-containing device. However, the control device showed a lower V_{oc} despite having a comparable charge density. This is in line with the theory that the interlayers reduce the metal's work

function, causing an energetic shift at the electrode. All devices show increased charge density for a given V_{oc} due to interlayer degradation. It is a sign of an increase in trap density, probably due to photo-oxidation of the active layer materials or by reactions triggered close to the interface. We can evaluate how an interlayer might deter this specific degradation route thanks to the variation in the magnitude of the increase that depends on the interlayer. At a V_{oc} of 0.55 V, the interlayer-free device experienced the most significant increase in trap density, with a charge density increase of over 20 times. This suggests that the absence of an interlayer, which serves as a buffer against Al diffusion and oxygen/moisture ingress, causes the active layer to be most severely impacted. When the small amplitude laser pulse perturbed them, all devices displayed single exponential TPV decays. Figure 20b displays the carrier lifetimes as a function of charge density. These lifetimes are indicated by the time constants obtained by fitting single exponential functions to these decay curves. These results agree with the increased trap formation observed with carrier lifetime extension for a given carrier density. Thus, charges are held in these traps for a specific period before their release and another chance to combine. As a result, these traps are probably shallow traps without recombination centers. The V_{oc} of the degraded devices did not increase with the longer carrier lifetime. Degraded devices do not experience an increase in V_{oc} due to the longer carrier lifetime since a much higher charge density is now required to achieve the same Fermi-level splitting as in new devices. There is some variation in the carrier lifetime versus V_{oc} trend lines. However, the overall lifetimes are similar for all devices, especially when the intensity is close to 1 sun, proving that the interlayer properties do not significantly affect recombination kinetics. Since this process also slows down recombination, the increased trap density might affect the FF of the devices, one of the main losses brought on by degradation. However, it might not result in appreciable charge losses.

The validity of TPV to study OSCs has recently been questioned due to discrepancies in carrier lifetime values often reported for this type of device. Azzouzi et al.^[228] have explored ways of overcoming this and proposed using transient photocharge as a new technique for fullerene and nonfullerene OSCs.

In considering tools for materials and device degradation studies (as summarized in Table 1) in a broader range, for either looking at parts of or the whole device, it is also important to consider tools for monitoring solution stability as one of the most significant advantages of OSCs and PSCs is solution processability. Solution processing could potentially enable cost-effective mass production and large-scale processing technology. Additional considerations must include tools for studying and decoupling the role of the ETL, HTL, interfacial dipoles, optical spacers, and plasmons that allow charge carriers to be extracted at the electrodes in the overall degradation/stability analysis from the main absorber materials. The article genuinely attempts to discuss many tools used to characterize and understand degradation mechanisms in OSCs and PSCs. While we may not cover every tool possible in the discussion above, we did touch on most standard tools or techniques employed. Before briefly discussing *in situ* characterization tools, we end this part with a few highlights of studies that have combined tools to probe different parts

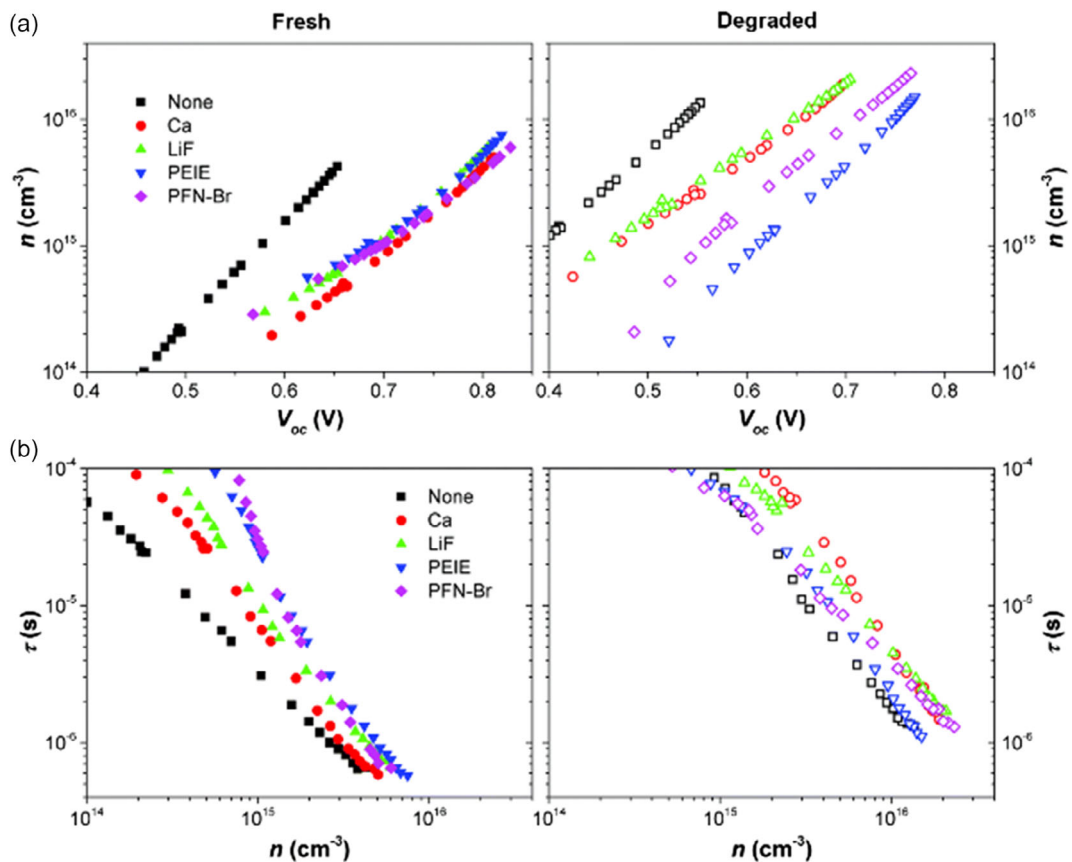


Figure 20. a) Charge density, n , as a function of V_{oc} for fresh and degraded cells and b) recombination lifetime as a function of charge density. Reproduced with permission.^[23] Copyright 2020, Wiley-VCH.

of the devices. For instance, analytic tools such as but not limited to ultraviolet photoelectron spectroscopy (UPS), KPFM, XPS, time-of-flight secondary ion mass spectroscopy (ToF-SIMS), and cyclic voltammetry can be used to monitor any change in the work function and energy levels between layers to investigate interfacial degradation.

Rivkin et al.^[232] compared the environmental stability of conventional devices with bathocuproine (BCP) as the hole-blocking layer (HBL) for methylammonium lead iodide (MAPbI_3) PSCs that use inorganic ZnO nanoparticle-based HBLs. ZnO and BCP devices were degraded under steady illumination in an inert environment for 14 h. The Ag electrodes were then removed via a tape and analyzed using XPS to investigate whether the ZnO HBL effectively blocked iodide ions migration. Even though both types of devices exhibit comparable initial PV performance based on their J - V measurements, the BCP devices showed a distinct and strong I 3d signal, demonstrating that iodide ions have reacted with the electrode. In contrast, the ZnO devices do not exhibit such evidence. This proves that a ZnO HBL effectively prevents iodide ions from migrating into a metal electrode on the time scale of the degradation experiment, most likely because the layer is denser than a BCP. However, the degradation dynamics of both devices were remarkably similar, indicating that preventing ion-induced electrode degradation has no positive impact on the operational stability of these cells.

Lee et al.^[233] suggested a solution-processed spinel CuCo_2O_4 as an efficient hole transport layer for PSCs with minimal hysteresis. Using characterizations techniques such as XPS, UV-vis-NIR spectroscopy, AFM, and J - V , they revealed that the sol-gel processed CuCo_2O_4 has well-matched energy levels, high electrical conductivity, high optical transparency, and efficient hole transport capability to the perovskite layer. The negligible hysteresis resulted in a highly stable and reliable PV performance using the HTL. These findings indicate the potential of solution-processed CuCo_2O_4 as a novel HTL for efficient and stable PSCs.

In a different study, Islam et al.^[121] examined detailed changes in physical properties in relation to the degradation of PSC films and devices fabricated in the ambient using screen-printed candle soot carbon and Ag electrodes. They explored this relationship using XRD, field emission SEM, EDX, PL, UV-vis-NIR spectroscopy, and J - V measurement techniques. They found that the decomposition of PSC films reduced the performance of the devices in three ways: 1) a reduction in charge extraction efficiency brought about by the ion accumulation that creates a space charge region; 2) defects redistribution in the perovskite layer, as detected by PL analysis, which affects carrier recombination; and 3); the electrode's chemical reaction with the selective layers (ETL and HTL). These phenomena may lead to lower shunt resistance and high series resistance, resulting in decreased FF and

Table 1. Some characterization tools and how they can be used to probe degradation in OSC and PSC materials and devices.

Tool	Parameters	Purpose	OSCs	PSCs	Ref.
UV-vis-NIR	Transmittance/absorbance/reflectance	For monitoring degradation due to (photo/thermal-induced or agents) bleaching of the active layer materials	✓	✓	[97-100,104,189,227,243]
NMR	Chemical peak shift/Chemical peak position	For monitoring degradation due to heat or light, or moisture in the liquid or solid state of pristine and/or blended active layer materials based on the measuring quantum mechanical properties of atomic nuclei reflected in the decrease in peak intensity, appearance, and disappearance of peaks	✓	✓	[107-109,113]
XRD	Crystallinity/crystallite size	For monitoring degradation due to microstructural changes of the thin film (i.e., presence of PbI_2 peaks in perovskites) /chemical composition/crystal structure	limited usage	✓	[65,119-122,127,244-246]
TRPL	Intensity and decay rate of photoluminescence	For monitoring changes in recombination and photoexcitation dynamics due to environmental stressors (Recombination coefficient/Carrier lifetime)	✓	✓	[119,137-139,141-143,190]
TAS	Difference in absorbance	For monitoring changes in charge carrier dynamics, exciton kinetics due to degradation as reflected in charge generation process/recombination/carrier lifetime	✓	✓	[119,144,145]
AFM/ c-AFM	Topography amplitude phase	For monitoring degradation due to morphological changes of the active layer materials using surface morphology or electrical characteristics (domain size and shape, Roughness changes, and phase segregations)	✓	✓	[138,147,148,150,201]
GIWAXS/ GISAXS	Film molecular structure, crystallinity, morphology	For monitoring degradation due to molecular structure and crystallinity changes of the active layer materials (domain size, phase separation, purity, crystallinity crystal orientation)	✓	✓	[141,142,152,153]
SEM	Morphology and microstructures	For evaluating degradation due to morphological microstructure changes of the perovskite layer (the presence of pinholes or voids in degraded samples can be seen)	limited usage	✓	[160-163]
TEM	Nanostructure, morphology, and stress	For monitoring with high precision, the degradation due to nanostructural changes of the active layer materials	✓	✓	[90,165,166,195]
EDS	Elemental/chemical composition or proportion	For monitoring the percentage loss of elements and new elements present due to degradation or original elemental proportion changes	limited usage	✓	[165,169]
XPS	Local bonding of constituent atoms and density of occupied states	For monitoring degradation due to chemical structure changes of the active layer materials (composition, concentration, and distribution of elements and residues)	✓	✓	[172-174]
FTIR or IR	Functional groups, bond stretching, and bond deformation	For monitoring degradation due to chemical structure changes of the active layer materials (identification of signature bonds: decrease, increase, the appearance of peaks)	✓	✓	[175-179]
Impedance Spectroscopy	Electrical and electrochemical processes—charge extraction and dynamics	For evaluating changes in resistive and capacitive behavior of the devices (change in series and shunt resistance)/probe interrelation between impurities and stability of devices	✓	✓	[217-219]
CV	Chemical reactivity—oxidation/reduction processes	For identifying oxidation/reduction by-products and stoichiometry, and phase change in degraded sample	✓	✓	[220,221,242]

Table 1. Continued.

Tool	Parameters	Purpose	OSCs	PSCs	Ref.
KPFM	Work function, sample topography, and surface photovoltaic	For identifying changes in electronic state, energy band-bending, charge trapping, and surface reconstruction due to degradation agents	✓	✓	[222,223,226]
J-V	V_{OC} , J_{SC} , FF	For monitoring the decay rate of each parameter/device lifetime (T_{80})	✓	✓	[33,191,195,197]
Light intensity dependence	Ideality factor (n)/Power factor (α)	For monitoring the slope of J_{SC} , V_{OC} as a function of light intensity for changes in charge recombination dynamics	✓	✓	[200-202,247]
SCLC	J-V curve of electron- and hole-only devices	For monitoring changes in space charge carrier density, charge carrier mobilities, trap densities in the devices	✓	limited usage	[201,203,204,206]
IPCE or EQE	EQE as a function of wavelength	For monitoring changes in EQE peaks intensity (calculated integrated current)	✓	✓	[138,216]
TPV	Charge carrier lifetime, photogenerated charge carrier density, and recombination dynamics	For measuring induced voltage transient and changes in carrier lifetime, and slow recombination rate for degraded samples.	✓	✓	[228,230,231]

V_{OC} . The chemical reactions at the mentioned interfaces may result in poor interfacial junction quality, leading to poor performance over time.

Our last highlight is a report by Hang et al.^[102] about stabilizing fullerene for burn-in-free PSCs with ultraviolet preconditioning. They combined UPS with SEM, XRD, and XPS for device characterization to achieve their objectives. UPS was used to measure the changes in the work function of the studied PCBM ETL films: PCBM:Bphen and pristine PCBM. The work function of PCBM:Bphen was lower (4.29 eV) compared to the pristine PCBM (4.33 eV), in agreement with their observed improvement of electron concentration and conductivities in the PCBM:Bphen layer. After illumination, the work function of PCBM increases from 4.33 to 4.47 eV. In comparison, that of PCBM:Bphen increases minimally from 4.29 to 4.33 eV, with stabilized device performance for PCBM:Bphen ETL-based devices. After 24 h UV illumination, the samples were imaged. SEM images revealed a severe degradation of the perovskite film on SnO_2 ($\text{SnO}_2/\text{Perovskite}$) due to the photocatalytic effect of the metal oxide. With XRD, they show PbI_2 and metallic lead products are formed in $\text{SnO}_2/\text{perovskite}$ film after illumination. In contrast, the PCBM ETL ($\text{SnO}_2/\text{PCBM}/\text{Perovskite}$) film degradation was negligible. Using XPS spectra before and after illumination, they demonstrated that using the Bphen additive stabilizes the SnO_2/PCBM interlayer even more and thus eliminates the formation of PbI_2 and the burn-in effect.

For a comprehensive degradation study, many characterization tools come into play to elucidate different aspects of the complexity of the degradation mechanisms and pathways and provide insights into mitigation paths to adopt.

3. In Situ Characterization Tools

While our focus has been on ex situ characterization techniques to study the degradation mechanisms in OSCs and PSCs, in situ characterizations can also be deployed for the same purpose.

These in situ techniques are of interest and are particularly helpful because they can provide real-time information on the chemical and structural changes at different degradation stages. Ex situ techniques can only be employed to obtain information from the final byproducts of degradation. Combining ex situ with in situ techniques will provide a more robust approach to studying the degradation mechanisms in OSCs and PSCs under different intrinsic and extrinsic stressors and/or operating conditions.^[234] The existing in situ techniques can be broadly categorized into three major groups: in situ electron microscopy (EM), in situ X-ray-assisted (XRA), and in situ optoelectronic characterizations.^[93]

In situ EM techniques primarily include SEM and TEM, regarded as one of the best tools for studying microstructures of materials due to their high resolution and 3D image capabilities.^[235] Using in situ EM, it is possible to dynamically and precisely monitor changes in the surface morphology and microstructure of OSCs and PSCs as they degrade under various stressors.^[236] Multiple reactions are triggered in OSCs and PSCs due to external stimuli, eventually resulting in degradation. Studying these reactions and degradation mechanisms under different environmental factors is crucial to finding a solution to their instability. In situ EM is a powerful method for studying the real-time degradation of these devices under light, heat, and bias.

In situ XRA techniques include XRD, XPS, GIWAX, and GISANS. These techniques can be used to understand the crystal structure and orientation, chemical makeup, and morphology of OSCs and PSCs. Compared to EM techniques, X-rays have the unique advantage of penetrating most atmospheres and materials. For this reason, it is easy to use an X-ray source for in situ characterization to track how OSC and PSC material and film change in the presence of moisture, heat, stress, light, and electronic bias. Thus, in situ XRA techniques are commonly used to track the chemical, structural, and morphological changes of materials, films, and devices from formation to degradation.

In situ optoelectronic techniques are commonly used for carrier dynamics studies during degradation in both (OSCs and

PSCs) and ion migration in PSCs under different stressors. These techniques include *in situ* PL, c-AFM, KPFM, Electroluminescence (EL), and Light Beam Induced Current (LBIC).^[237]

Some instances where these *in situ* techniques have been used to probe degradation in OSCs and PSCs are briefly highlighted here. However, in the case of PSCs, Meng et al.^[94] and Babbe et al.^[238] offer a comprehensive discussion. One particular example we would like to highlight using PSCs is the work of Ma et al.,^[239] where *in situ* KPFM and c-AFM were used to investigate temperature-dependent electrical properties. Using *in situ* KPFM, they examined the local morphological changes of MAPbI₃ film as a function of temperature (30–80 °C). They kept the image field constant while calculating the average contact potential difference (CPD) of the MAPbI₃ square scanning area to assess the temperature-dependent Fermi level shifts. They discovered that the CPD of the films decreased with increased temperature. Their study successfully confirmed that thermal stress causes phase transformation in PSCs, consistent with the decrease in the photocurrent. *In situ* c-AFM was used to understand the distribution of this photocurrent with illumination over the temperature range. This helped to understand the carrier transport and recombination in PSC films. It was observed that the photocurrent decreased as the temperature increased. The carriers were nearly constant because the impurity was fully ionized. The intrinsic excitation was not significant at this temperature range. Thus, the shifted-down Fermi level led to a decrease in CPD, photocurrent, and built-in field. Combining these two *in situ* techniques, they could investigate the evolution of carrier dynamics and migration during the heat- and light-induced degradation processes and were able to understand the degradation mechanisms in PSCs effectively.

For OSCs, Silvestri et al.^[240] investigated the microstructural and morphological characteristics of the layers of PTB7/PC₇₁BM in OSCs with Ca/Al cathodes using *in situ* energy dispersive X-ray diffraction (EDXD) and high-resolution X-ray diffraction (HR-EDXD). They effectively and successfully identify aging routes in bulk and interfacial structural properties. Specifically, they used the *in situ* EDXD to demonstrate how illumination affects the polymer component and causes a decrease in crystallinity. Generosi et al.^[238] also used a unique *in situ* energy dispersive X-ray reflectivity (ED-XRR) methodology to examine Wells–Dawson polyoxometalate (K₆P₂W₁₈O₆₂) as a hole transporting layer in OSCs. They repeatedly found that K₆P₂W₁₈O₆₂ thin films make ideal candidates for the OSC device interface because they have excellent bulk and interface properties and superior optical and morphological stability under prolonged illumination. They demonstrated how the high reproducibility of measurements allows monitoring aging processes over several hours when they studied K₆P₂W₁₈O₆₂ with a home-made setup combining ED-XRR and AFM with an incorporated light source.

Both *in situ* EM and X-ray techniques can characterize heat, moisture, light, and bias-induced and dynamic degradation processes in OSCs and PSCs. Still, the process must always be complemented with other techniques: *in situ* EM combined with EDX or *in situ* X-ray combined with J–V. In contrast, *in situ* optoelectronic methods can directly characterize the evolution of carrier dynamics and ion movements during the degradation

process. These *in situ* optoelectronic characterizations are widely used techniques to directly investigate the carrier dynamics and recombination kinetics and the internal electrochemical potential of free charge carriers within complete devices, the single absorber layer, or transport layers.

4. Outlook and Future Challenges

OSCs and PSCs are technologies of great interest to the scientific community and society due to their potential to revolutionize energy use. However, they face major challenges:

Improving the stability and performance of OSCs and PSCs has been one primary concern for researchers and manufacturers, especially as the quest for abundant clean energy continues to rise. While there has been tremendous advancement in materials characterization techniques, there are known limitations for current metrology for studying degradation in these devices.

One obvious limitation is the beam-sensitive nature of perovskite materials, making their characterization with traditional techniques such as TEM, SEM, XRD, and other irradiation techniques difficult. To overcome this limitation, future metrology or studies on degradation with such techniques should explore lower beam intensities while seeking better ways of characterizing or improving the techniques. If this is not done, chances are that the reported degradation mechanisms may not be accurately represented as caused by degradation stressors, making understanding degradation difficult and, by extension, improvement for better performance and stability.

Just like in the case of TPV, the accuracy of some techniques is in doubt as there exist discrepancies in the values or data they provide. As such, new metrologies should be explored in future research to ensure that methods of choice can arrive at similar outcomes with different instruments and similar environmental conditions.

Finally, there are concerns about the toxicity of OSCs due to used solvents in their processing and PSCs due to lead content. Developing environmentally friendly solvents (green solvents) and lead-free perovskite materials will also be a meaningful direction. Transferring the lab-scale technology to large-scale module processing while maintaining efficiency and stability will further challenge these technologies. With it comes the issue of reduced efficiency, reliability, and other instability and failure modes at larger scales.^[241] Therefore, the underlying degradation mechanism must be understood by monitoring the degradation factors. It is more important to know the principles of each method and the meaning of the obtained values.

5. Conclusion

OSCs and PSCs have shown great promise for the future photovoltaic market because of their low-temperature and low-cost processing and the potential for roll-to-roll manufacturing on flexible substrates. Although laboratory-scale devices have shown significant efficiency improvements, a substantial gap exists between efficiency and stability. Clearly, this discrepancy is a considerable obstacle to commercializing these technologies. Thus, a better understanding of the underlying degradation mechanisms

of active layer materials and devices to improve stability has already proven its worth. Regarding lessons from previous studies, analytical tools for monitoring the degradation mechanism play a vital role in understanding the degradation mechanism, thus improving overall stability. Considering the lessons learned from previous studies, such as the need to consider the ionic properties of perovskite films when interpreting data in some cases, such as SCLC, a precise understanding of these novel materials and devices using analytical tools will play an important role in elucidating the degradation mechanism, and thereby improve overall stability. This review has provided the basic information of several tools used to monitor the degradation of organic and perovskite materials and devices and an understanding of how they have been used over the years. We believe device stability can be significantly improved by understanding how each tool can be used and applying them jointly for in-depth analysis.

Acknowledgements

S.Y.K. and C.C.F.K. contributed equally to this work. The authors want to acknowledge initial input from Dr. Ivy M. Asuo of The Pennsylvania State University.

Conflict of Interest

The authors declare no conflict of interest.

Keywords

degradation mechanisms, durability, organic solar cells, perovskite solar cells, stability, tools, techniques

Received: February 28, 2023

Revised: April 19, 2023

Published online: May 23, 2023

- [1] Z. Song, C. L. McElvany, A. B. Phillips, I. Celik, P. W. Krantz, S. C. Watthage, G. K. Liyanage, D. Apul, M. J. Heben, *Energy Environ. Sci.* **2017**, *10*, 1297.
- [2] M. Cai, Y. Wu, H. Chen, X. Yang, Y. Qiang, L. Han, *Adv. Sci.* **2017**, *4*, 1600269.
- [3] H. Zhang, J. Cheng, F. Lin, H. He, J. Mao, K. S. Wong, A. K.-Y. Jen, W. C. Choy, *ACS Nano* **2016**, *10*, 1503.
- [4] H. Zhang, J. Cheng, D. Li, F. Lin, J. Mao, C. Liang, A. K.-Y. Jen, M. Grätzel, W. C. Choy, *Adv. Mater.* **2017**, *29*, 1604695.
- [5] K. Hwang, Y.-S. Jung, Y.-J. Heo, F. H. Scholes, S. E. Watkins, J. Subbiah, D. J. Jones, D.-Y. Kim, D. Vak, *Adv. Mater.* **2015**, *27*, 1241.
- [6] A. Mei, X. Li, L. Liu, Z. Ku, T. Liu, Y. Rong, M. Xu, M. Hu, J. Chen, Y. Yang, *Science* **2014**, *345*, 295.
- [7] Y. Cui, H. Yao, L. Hong, T. Zhang, Y. Tang, B. Lin, K. Xian, B. Gao, C. An, P. Bi, *Nat. Sci. Rev.* **2020**, *7*, 1239.
- [8] J. Wang, Z. Zheng, Y. Zu, Y. Wang, X. Liu, S. Zhang, M. Zhang, J. Hou, *Adv. Mater.* **2021**, *33*, 2102787.
- [9] J. J. Yoo, G. Seo, M. R. Chua, T. G. Park, Y. Lu, F. Rotermund, Y.-K. Kim, C. S. Moon, N. J. Jeon, J.-P. Correa-Baena, V. Bulović, S. S. Shin, M. G. Bawendi, J. Seo, *Nature* **2021**, *590*, 587.
- [10] C. W. Tang, *Appl. Phys. Lett.* **1986**, *48*, 183.
- [11] J. J. M. Halls, C. A. Walsh, N. C. Greenham, E. A. Marseglia, R. H. Friend, S. C. Moratti, A. B. Holmes, *Nature* **1995**, *376*, 498.
- [12] G. Yu, J. Gao, J. C. Hummelen, F. Wudl, A. J. Heeger, *Science* **1995**, *270*, 1789.
- [13] S. Holliday, R. S. Ashraf, A. Wadsworth, D. Baran, S. A. Yousaf, C. B. Nielsen, C.-H. Tan, S. D. Dimitrov, Z. Shang, N. Gasparini, *Nat. Commun.* **2016**, *7*, 1.
- [14] P. Cheng, G. Li, X. Zhan, Y. Yang, *Nat. Photonics* **2018**, *12*, 131.
- [15] N. Y. Doumon, L. Yang, F. Rosei, *Nano Energy* **2022**, *94*, 106915.
- [16] N. Y. Doumon, F. V. Houard, J. Dong, P. Christodoulis, M. V. Dryzhov, G. Portale, L. J. A. Koster, *J. Mater. Chem. C* **2019**, *7*, 5104.
- [17] N. Gasparini, A. Salleo, I. McCulloch, D. Baran, *Nat. Rev. Mater.* **2019**, *4*, 229.
- [18] T. Upreti, Y. Wang, F. Gao, M. Kemerink, *Solar RRL* **2022**, 2200450.
- [19] X. Gu, X. Lai, Y. Zhang, T. Wang, W. L. Tan, C. R. McNeill, Q. Liu, P. Sonar, F. He, W. Li, C. Shan, A. K. K. Kyaw, *Adv. Sci.* **2022**, *9*, 2200445.
- [20] Z. Zheng, J. Wang, P. Bi, J. Ren, Y. Wang, Y. Yang, X. Liu, S. Zhang, J. Hou, *Joule* **2022**, *6*, 171.
- [21] A. Kojima, K. Teshima, Y. Shirai, T. Miyasaka, *J. Am. Chem. Soc.* **2009**, *131*, 6050.
- [22] H.-S. Kim, C.-R. Lee, J.-H. Im, K.-B. Lee, T. Moehl, A. Marchioro, S.-J. Moon, R. Humphry-Baker, J.-H. Yum, J. E. Moser, M. Grätzel, N.-G. Park, *Sci. Rep.* **2012**, *2*, 591.
- [23] M. Saliba, T. Matsui, J.-Y. Seo, K. Domanski, J.-P. Correa-Baena, M. K. Nazeeruddin, S. M. Zakeeruddin, W. Tress, A. Abate, A. Hagfeldt, M. Grätzel, *Energy Environ. Sci.* **2016**, *9*, 1989.
- [24] H. Min, D. Y. Lee, J. Kim, G. Kim, K. S. Lee, J. Kim, M. J. Paik, Y. K. Kim, K. S. Kim, M. G. Kim, T. J. Shin, S. Il Seok, *Nature* **2021**, *598*, 444.
- [25] M. J. Paik, J. W. Yoo, J. Park, E. Noh, H. Kim, S.-G. Ji, Y. Y. Kim, S. I. Seok, *ACS Energy Lett.* **2022**, *7*, 1864.
- [26] Interactive Best Research-Cell Efficiency Chart, **2023**, <https://www.nrel.gov/pv/interactive-cell-efficiency.html> (accessed: February 2023).
- [27] G. Shankar, P. Kumar, B. Pradhan, *Mater. Today Sustain.* **2022**, *20*, 100241.
- [28] A. Al-Ashouri, E. Köhnen, B. Li, A. Magomedov, H. Hempel, P. Caprioglio, J. A. Márquez, A. B. Morales Vilches, E. Kasparavicius, J. A. Smith, N. Phung, D. Menzel, M. Grischek, L. Kegelmann, D. Skroblin, C. Gollwitzer, T. Malinauskas, M. Jošt, G. Matič, B. Rech, R. Schlatmann, M. Topič, L. Korte, A. Abate, B. Stannowski, D. Neher, M. Stolterfoht, T. Unold, V. Getautis, S. Albrecht, *Science* **2020**, *370*, 1300.
- [29] E. Köhnen, P. Wagner, F. Lang, A. Cruz, B. Li, M. Roß, M. Jošt, A. B. Morales-Vilches, M. Topič, M. Stolterfoht, D. Neher, L. Korte, B. Rech, R. Schlatmann, B. Stannowski, S. Albrecht, *Sol. RRL* **2021**, *5*, 2100244.
- [30] A. Guchhait, H. A. Dewi, S. W. Leow, H. Wang, G. Han, F. B. Suhaimi, S. Mhaisalkar, L. H. Wong, N. Mathews, *ACS Energy Lett.* **2017**, *2*, 807.
- [31] M. Jošt, E. Köhnen, A. Al-Ashouri, T. Bertram, Š. Tomšič, A. Magomedov, E. Kasparavicius, T. Kodalle, B. Lipovšek, V. Getautis, *ACS Energy Lett.* **2022**, *7*, 1298.
- [32] M. Jørgensen, K. Norrman, S. A. Gevorgyan, T. Tromholt, B. Andreasen, F. C. Krebs, *Adv. Mater.* **2012**, *24*, 580.
- [33] W. R. Mateker, M. D. McGhee, *Adv. Mater.* **2017**, *29*, 1603940.
- [34] K. Norrman, N. B. Larsen, F. C. Krebs, *Sol. Energy Mater. Sol. Cells* **2006**, *90*, 2793.
- [35] M. O. Reese, S. A. Gevorgyan, M. Jørgensen, E. Bundgaard, S. R. Kurtz, D. S. Ginley, D. C. Olson, M. T. Lloyd, P. Morville, E. A. Katz, A. Elschner, O. Haillant, T. R. Currier, V. Shrotriya,

- M. Hermenau, M. Riede, K. R. Kirov, G. Trimmel, T. Rath, O. Inganäs, F. Zhang, M. Andersson, K. Tvingstedt, M. Lira-Cantu, D. Laird, C. McGuiness, S. (Jimmy) Gowrisanker, M. Pannone, M. Xiao, J. Hauch, et al., *Sol. Energy Mater. Sol. Cells* **2011**, *95*, 1253.
- [36] M. V. Khenkin, E. A. Katz, A. Abate, G. Bardizza, J. J. Berry, C. Brabec, F. Brunetti, V. Bulović, Q. Burlingame, A. Di Carlo, R. Cheacharoen, Y. B. Cheng, A. Colsmann, S. Cros, K. Domanski, M. Dusza, C. J. Fell, S. R. Forrest, Y. Galagan, D. Di Girolamo, M. Grätzel, A. Hagfeldt, E. von Hauff, H. Hoppe, J. Kettle, H. Köbler, M. S. Leite, S. (Frank) Liu, Y. L. Loo, J. M. Luther, *Nat. Energy*, **2020**, *5*, 35.
- [37] H. Kang, G. Kim, J. Kim, S. Kwon, H. Kim, K. Lee, *Adv. Mater.* **2016**, *28*, 7821.
- [38] B. Li, W. Zhang, *Commun. Mater.* **2022**, *3*, 65.
- [39] Y. Cheng, L. Ding, *Energy Environ. Sci.* **2021**, *14*, 3233.
- [40] M. Hermenau, M. Riede, K. Leo, S. A. Gevorgyan, F. C. Krebs, K. Norrman, *Sol. Energy Mater. Sol. Cells* **2011**, *95*, 1268.
- [41] M. O. Reese, A. M. Nardes, B. L. Rupert, R. E. Larsen, D. C. Olson, M. T. Lloyd, S. E. Shaheen, D. S. Ginley, G. Rumbles, N. Kopidakis, *Adv. Funct. Mater.* **2010**, *20*, 3476.
- [42] J. Huang, P. F. Miller, J. C. de Mello, A. J. de Mello, D. D. C. Bradley, *Synth. Metals* **2003**, *139*, 569.
- [43] A. Manor, E. A. Katz, T. Tromholt, F. C. Krebs, *Adv. Energy Mater.* **2011**, *1*, 836.
- [44] S. Mazumdar, Y. Zhao, X. Zhang, *Front. Electron.* **2021**, *2*, 712785.
- [45] J. A. McLeod, L. Liu, *J. Phys. Chem. Lett.* **2018**, *9*, 2411.
- [46] Z. Li, M. Yang, J.-S. Park, S.-H. Wei, J. J. Berry, K. Zhu, *Chem. Mater.* **2016**, *28*, 284.
- [47] C. J. Bartel, C. Sutton, B. R. Goldsmith, R. Ouyang, C. B. Musgrave, L. M. Ghiringhelli, M. Scheffler, *Sci. Adv.* **2019**, *5*, eaav0693.
- [48] W.-J. Yin, T. Shi, Y. Yan, *Appl. Phys. Lett.* **2014**, *104*, 063903.
- [49] X. Ma, L. Yang, K. Lei, S. Zheng, C. Chen, H. Song, *Nano Energy* **2020**, *78*, 105354.
- [50] A. Amat, E. Mosconi, E. Ronca, C. Quarti, P. Umari, Md.K. Nazeeruddin, M. Grätzel, F. De Angelis, *Nano Lett.* **2014**, *14*, 3608.
- [51] M. R. Filip, G. E. Eperon, H. J. Snaith, F. Giustino, *Nat. Commun.* **2014**, *5*, 5757.
- [52] G. E. Eperon, S. D. Stranks, C. Menelaou, M. B. Johnston, L. M. Herz, H. J. Snaith, *Energy Environ. Sci.* **2014**, *7*, 982.
- [53] C. C. Boyd, R. Cheacharoen, T. Leijtens, M. D. McGehee, *Chem. Rev.* **2019**, *119*, 3418.
- [54] S. Kundu, T. L. Kelly, *EcoMat* **2020**, *2*.
- [55] M. K. Gangishetty, R. W. J. Scott, T. L. Kelly, *Nanoscale* **2016**, *8*, 6300.
- [56] L. Ling, S. Yuan, P. Wang, H. Zhang, L. Tu, J. Wang, Y. Zhan, L. Zheng, *Adv. Funct. Mater.* **2016**, *26*, 5028.
- [57] M. Lv, X. Dong, X. Fang, B. Lin, S. Zhang, X. Xu, J. Ding, N. Yuan, *RSC Adv.* **2015**, *5*, 93957.
- [58] X. Gong, M. Li, X.-B. Shi, H. Ma, Z.-K. Wang, L.-S. Liao, *Adv. Funct. Mater.* **2015**, *25*, 6671.
- [59] N. Adhikari, A. Dubey, E. A. Gaml, B. Vaagensmith, K. M. Reza, S. A. A. Mabrouk, S. Gu, J. Zai, X. Qian, Q. Qiao, *Nanoscale* **2016**, *8*, 2693.
- [60] H. Gao, C. Bao, F. Li, T. Yu, J. Yang, W. Zhu, X. Zhou, G. Fu, Z. Zou, *ACS Appl. Mater. Interfaces* **2015**, *7*, 9110.
- [61] H. Zhou, Q. Chen, G. Li, S. Luo, T. Song, H.-S. Duan, Z. Hong, J. You, Y. Liu, Y. Yang, *Science* **2014**, *345*, 542.
- [62] C.-G. Wu, C.-H. Chiang, Z.-L. Tseng, Md.K. Nazeeruddin, A. Hagfeldt, M. Grätzel, *Energy Environ. Sci.* **2015**, *8*, 2725.
- [63] A. Solanki, S. S. Lim, S. Mhaisalkar, T. C. Sum, *ACS Appl. Mater. Interfaces* **2019**, *11*, 25474.
- [64] J. Yang, B. D. Siempelkamp, D. Liu, T. L. Kelly, *ACS Nano* **2015**, *9*, 1955.
- [65] J. A. Christians, P. A. Miranda Herrera, P. V. Kamat, *J. Am. Chem. Soc.* **2015**, *137*, 1530.
- [66] A. M. A. Leguy, Y. Hu, M. Campoy-Quiles, M. I. Alonso, O. J. Weber, P. Azarhoosh, M. van Schilfgaarde, M. T. Weller, T. Bein, J. Nelson, P. Docampo, P. R. F. Barnes, *Chem. Mater.* **2015**, *27*, 3397.
- [67] M. Koehl, M. Heck, S. Wiesmeier, J. Wirth, *Sol. Energy Mater. Sol. Cells* **2011**, *95*, 1638.
- [68] P. Holzhey, M. Saliba, *J. Mater. Chem. A* **2018**, *6*, 21794.
- [69] Q. Wang, B. Chen, Y. Liu, Y. Deng, Y. Bai, Q. Dong, J. Huang, *Energy Environ. Sci.* **2017**, *10*, 516.
- [70] A. M. Askar, G. M. Bernard, B. Wiltshire, K. Shankar, V. K. Michaelis, *J. Phys. Chem. C* **2017**, *121*, 1013.
- [71] J. Schlipf, L. Bießmann, L. Oesinghaus, E. Berger, E. Metwalli, J. A. Lercher, L. Porcar, P. Müller-Buschbaum, *J. Phys. Chem. Lett.* **2018**, *9*, 2015.
- [72] D. Li, S. A. Bretschneider, V. W. Bergmann, I. M. Hermes, J. Mars, A. Klasen, H. Lu, W. Tremel, M. Mezger, H.-J. Butt, S. A. L. Weber, R. Berger, *J. Phys. Chem. C* **2016**, *120*, 6363.
- [73] W.-C. Lin, H.-Y. Chang, K. Abbasi, J.-J. Shyue, C. Burda, *Adv. Mater. Interfaces* **2017**, *4*, 1600673.
- [74] Z. Song, N. Shrestha, S. C. Watthage, G. K. Liyanage, Z. S. Almutawah, R. H. Ahangarnejhad, A. B. Phillips, R. J. Ellington, M. J. Heben, *J. Phys. Chem. Lett.* **2018**, *9*, 6312.
- [75] J. Yang, Z. Yuan, X. Liu, S. Braun, Y. Li, J. Tang, F. Gao, C. Duan, M. Fahlman, Q. Bao, *ACS Appl. Mater. Interfaces* **2018**, *10*, 16225.
- [76] N. Grossiord, J. M. Kroon, R. Andriessen, P. W. M. Blom, *Org. Electron.* **2012**, *13*, 432.
- [77] S. Savagatrup, A. D. Printz, T. F. O'Connor, A. V. Zaretski, D. Rodriguez, E. J. Sawyer, K. M. Rajan, R. I. Acosta, S. E. Root, D. J. Lipomi, *Energy Environ. Sci.* **2015**, *8*, 55.
- [78] Y. Liu, S. Li, Y. Jing, L. Xiao, H. Zhou, *Acta Chim. Sin.* **2022**, *80*, 993.
- [79] F. Cao, P. Zhang, H. Sun, M. Wang, L. Li, *Nano Res.* **2022**, *15*, 8955.
- [80] E. Aktas, N. Rajamanickam, J. Pascual, S. Hu, M. H. Aldama, D. Di Girolamo, W. Li, G. Nasti, E. Martínez-Ferrero, A. Wakamiya, E. Palomares, A. Abate, *Commun. Mater.* **2022**, *3*, 104.
- [81] L. E. Mundt, L. T. Schelhas, *Adv. Energy Mater.* **2020**, *10*, 1903074.
- [82] J. M. Howard, R. Lahoti, M. S. Leite, *Adv. Energy Mater.* **2020**, *10*, 1903161.
- [83] S. Béchu, M. Ralaizarisoa, A. Etcheberry, P. Schulz, *Adv. Energy Mater.* **2020**, *10*, 1904007.
- [84] G. Delport, S. Macpherson, S. D. Stranks, *Adv. Energy Mater.* **2020**, *10*, 1903814.
- [85] M. Kodur, R. E. Kumar, Y. Luo, D. N. Cakan, X. Li, M. Stuckelberger, D. P. Fenning, *Adv. Energy Mater.* **2020**, *10*, 1903170.
- [86] S. P. Harvey, J. Messinger, K. Zhu, J. M. Luther, J. J. Berry, *Adv. Energy Mater.* **2020**, *10*, 1903674.
- [87] T. Kirchartz, J. A. Márquez, M. Stolterfoht, T. Unold, *Adv. Energy Mater.* **2020**, *10*, 1904134.
- [88] K. Miyano, M. Yanagida, Y. Shirai, *Adv. Energy Mater.* **2020**, *10*, 1903097.
- [89] T. J. Savenije, D. Guo, V. M. Caselli, E. M. Hutter, *Adv. Energy Mater.* **2020**, *10*, 1903788.
- [90] Y. Zhou, H. Sternlicht, N. P. Padture, *Joule* **2019**, *3*, 641.
- [91] F. Zhang, S. H. Silver, N. K. Noel, F. Ullrich, B. P. Rand, A. Kahn, *Adv. Energy Mater.* **2020**, *10*, 1903252.
- [92] D. P. Fenning, P. Schulz, S. D. Stranks, *Adv. Energy Mater.* **2020**, *10*, 2001812.
- [93] X. Meng, X. Tian, S. Zhang, J. Zhou, Y. Zhang, Z. Liu, W. Chen, *Sol. RRL* **2022**, *6*, 2200280.
- [94] Y. Zhen, F. Zhang, H. Liu, Y. Yan, X. Li, S. Wang, *J. Mater. Chem. C* **2022**, *10*, 9953.
- [95] D. Abbaszadeh, G. A. H. Wetzel, N. Y. Doumon, P. W. M. Blom, *J. Appl. Phys.* **2016**, *119*, 095503.

- [96] Y. Cui, Y. Xu, H. Yao, P. Bi, L. Hong, J. Zhang, Y. Zu, T. Zhang, J. Qin, *J. Ren, Adv. Mater.* **2021**, *33*, 2102420.
- [97] M. Li, W. Zha, Y. Han, B. Liu, Q. Luo, C.-Q. Ma, *Org. Electron.* **2021**, *96*, 106257.
- [98] M. Shi, T. Wang, Y. Wu, R. Sun, W. Wang, J. Guo, Q. Wu, W. Yang, J. Min, *Adv. Energy Mater.* **2021**, *11*, 2002709.
- [99] Y. Qin, N. Balar, Z. Peng, A. Gadisa, I. Angunawela, A. Bagui, S. Kashani, J. Hou, H. Ade, *Joule* **2021**, *5*, 2129.
- [100] Q. Zhu, J. Xue, L. Zhang, J. Wen, B. Lin, H. B. Naveed, Z. Bi, J. Xin, H. Zhao, C. Zhao, *Small* **2021**, *17*, 2007011.
- [101] H. Xu, Y. Miao, N. Wei, H. Chen, Z. Qin, X. Liu, X. Wang, Y. Qi, T. Zhang, Y. Zhao, *Adv. Energy Mater.* **2022**, *12*, 2103151.
- [102] P. Hang, J. Xie, C. Kan, B. Li, Y. Zhang, P. Gao, D. Yang, X. Yu, *Adv. Mater.* **2021**, *33*, 2006910.
- [103] Y. Liang, P. Song, H. Tian, C. Tian, W. Tian, Z. Nan, Y. Cai, P. Yang, C. Sun, J. Chen, *Adv. Funct. Mater.* **2022**, *32*, 2110139.
- [104] Y. Zhao, T. Heumueller, J. Zhang, J. Luo, O. Kasian, S. Langner, C. Kupfer, B. Liu, Y. Zhong, J. Elia, A. Osset, J. Wu, C. Liu, Z. Wan, C. Jia, N. Li, J. Hauch, C. J. Brabec, *Nat. Energy* **2021**, *7*, 144.
- [105] L. Lanzetta, T. Webb, N. Zibouche, X. Liang, D. Ding, G. Min, R. J. E. Westbrook, B. Gaggio, T. J. Macdonald, M. S. Islam, S. A. Haque, *Nat. Commun.* **2021**, *12*, 2853.
- [106] S. Chen, X. Xiao, H. Gu, J. Huang, *Sci. Adv.* **2021**, *7*, eabe8130.
- [107] F. Aiello, S. Masi, *Nanomaterials* **2021**, *11*, 2024.
- [108] M. K. Singh, A. Singh, in *Characterization of Polymers and Fibres*, Elsevier, Amsterdam **2022**, pp. 321–339.
- [109] N. Y. Doumon, The Degradation of Organic Solar Cells: From Chemistry to Device Physics Through Materials, **2019**.
- [110] N. Y. Doumon, G. Wang, X. Qiu, A. J. Minnaard, R. C. Chiechi, L. J. A. Koster, *Sci. Rep.* **2019**, *9*, 4350.
- [111] N. Y. Doumon, G. Wang, R. C. Chiechi, L. J. A. Koster, *J. Mater. Chem. C* **2017**, *5*, 6611.
- [112] S. Masi, A. Rizzo, F. Aiello, F. Balzano, G. Uccello-Barretta, A. Listorti, G. Gigli, S. Colella, *Nanoscale* **2015**, *7*, 18956.
- [113] E. Hassanabadi, M. Latifi, Gualdrón-Reyes, F. Andrés, S. Masi, S. J. Yoon, M. Poyatos, B. Julián-López, I. Mora-Seró, *Nanoscale* **2020**, *12*, 14194.
- [114] A. A. M. Brown, T. J. N. Hooper, S. A. Veldhuis, X. Y. Chin, A. Bruno, P. Vashishtha, J. N. Tey, L. Jiang, B. Damodaran, S. H. Pu, S. G. Mhaisalkar, N. Mathews, *Nanoscale* **2019**, *11*, 12370.
- [115] Y. Chen, S. R. Smock, A. H. Flintgruber, F. A. Perras, R. L. Brutchey, A. J. Rossini, *J. Am. Chem. Soc.* **2020**, *142*, 6117.
- [116] P. B. Raja, K. R. Munusamy, V. Perumal, M. N. M. Ibrahim, in *Nano-Bioremediation : Fundamentals and Applications* (Eds: H.M.N. Iqbal, M. Bilal, T. A. Nguyen), Elsevier, Amsterdam **2022**, pp. 57–83.
- [117] R. L. Hadimani, in *Magnetic Nanostructured Materials* (Eds: A. A. El-Gendy, J. M. Barandiarán, R. L. Hadimani), Elsevier, Amsterdam **2018**, pp. 269–294.
- [118] S. K. Gupta, L. S. Pali, A. Garg, *Sol. Energy* **2019**, *178*, 133.
- [119] A. Weu, R. Kumar, J. F. Butscher, V. Lami, F. Paulus, A. A. Bakulin, Y. Yaynzo, *Adv. Funct. Mater.* **2020**, *30*, 1907432.
- [120] N. A. Tegegne, H. Wendimu, Z. Abdissa, W. Mammo, M. R. Andersson, F. G. Hone, D. M. Andoshee, O. Olaoye, G. Bosman, *J. Mater. Sci. Mater. Electron.* **2020**, *31*, 21303.
- [121] M. A. Islam, H. Mohafez, K. Sobayel, S. F. Wan Muhammad Hatta, A. K. M. Hasan, M. U. Khandaker, Md Akhtaruzzaman, G. Muhammad, N. Amin, *Nanomaterials* **2021**, *11*, 3463.
- [122] M. Qin, J. Cao, T. Zhang, J. Mai, T.-K. Lau, S. Zhou, Y. Zhou, J. Wang, Y.-J. Hsu, N. Zhao, *Adv. Energy Mater.* **2018**, *8*, 1703399.
- [123] A. Binek, F. C. Hanusch, P. Docampo, T. Bein, *J. Phys. Chem. Lett.* **2015**, *6*, 1249.
- [124] T. M. Koh, K. Fu, Y. Fang, S. Chen, T. C. Sum, N. Mathews, S. G. Mhaisalkar, P. P. Boix, T. Baikie, *J. Phys. Chem. C* **2014**, *118*, 16458.
- [125] C. C. Stoumpos, C. D. Malliakas, M. G. Kanatzidis, *Inorg. Chem.* **2013**, *52*, 9019.
- [126] J. S. Yun, J. Kim, T. Young, R. J. Patterson, D. Kim, J. Seidel, S. Lim, M. A. Green, S. Huang, A. Ho-Baillie, *Adv. Funct. Mater.* **2018**, *28*, 1705363.
- [127] B. Kim, M. Kim, J. H. Lee, S. I. Seok, *Adv. Sci.* **2020**, *7*, 1901840.
- [128] A. Mei, Y. Sheng, Y. Ming, Y. Hu, Y. Rong, W. Zhang, S. Luo, G. Na, C. Tian, X. Hou, Y. Xiong, Z. Zhang, S. Liu, S. Uchida, T.-W. Kim, Y. Yuan, L. Zhang, Y. Zhou, H. Han, *Joule* **2020**, *4*, 2646.
- [129] M. Stolterfoht, C. M. Wolff, J. A. Márquez, S. Zhang, C. J. Hages, D. Rothhardt, S. Albrecht, P. L. Burn, P. Meredith, T. Unold, *Nat. Energy* **2018**, *3*, 847.
- [130] V. Sarritzu, N. Sestu, D. Marongiu, X. Chang, S. Masi, A. Rizzo, S. Colella, F. Quochi, M. Saba, A. Mura, G. Bongiovanni, *Sci. Rep.* **2017**, *7*, 44629.
- [131] M. Tebyetekerwa, J. Zhang, Z. Xu, T. N. Truong, Z. Yin, Y. Lu, S. Ramakrishna, D. Macdonald, H. T. Nguyen, *ACS Nano* **2020**, *14*, 14579.
- [132] Q. Yang, K. Wang, H. Yu, X. Zhu, C. Han, L. Deng, H. Yang, F. Zhao, X. Sun, Q. Zhang, B. Hu, *Org. Electron.* **2018**, *62*, 203.
- [133] Y. Cai, Z. Zhang, Y. Zhou, H. Liu, Q. Qin, X. Lu, X. Gao, L. Shui, S. Wu, J. Liu, *Electrochim. Acta* **2018**, *261*, 445.
- [134] C. M. Wolff, F. Zu, A. Paulke, L. P. Toro, N. Koch, D. Neher, *Adv. Mater.* **2017**, *29*, 1700159.
- [135] F. Staub, H. Hempel, J.-C. Hebig, J. Mock, U. W. Paetzold, U. Rau, T. Unold, T. Kirchartz, *Phys. Rev. Appl.* **2016**, *6*, 044017.
- [136] D. Bi, C. Yi, J. Luo, J.-D. Décoppet, F. Zhang, S. M. Zakeeruddin, X. Li, A. Hagfeldt, M. Grätzel, *Nat. Energy* **2016**, *1*, 1.
- [137] K.-N. Zhang, Z.-N. Jiang, T. Wang, J.-W. Qiao, L. Feng, C.-C. Qin, H. Yin, S.-K. So, X.-T. Hao, *Nano Energy* **2021**, *79*, 105513.
- [138] L. Duan, M. Guli, Y. Zhang, H. Yi, F. Haque, A. Uddin, *Energy Technol.* **2020**, *8*, 1901401.
- [139] L. Duan, Y. Zhang, M. He, R. Deng, H. Yi, Q. Wei, Y. Zou, A. Uddin, *ACS Appl. Mater. Interfaces* **2020**, *12*, 27433.
- [140] E. V. Péan, S. Dimitrov, C. S. De Castro, M. L. Davies, *Phys. Chem. Chem. Phys.* **2020**, *22*, 28345.
- [141] K.-N. Zhang, X.-Y. Du, Z.-H. Chen, T. Wang, Z.-Q. Yang, H. Yin, Y. Yang, W. Qin, X.-T. Hao, *Adv. Energy Mater.* **2022**, *12*, 2103371.
- [142] C. A. R. Perini, E. Rojas-Gatjens, M. Ravello, A. Castro-Mendez, J. Hidalgo, Y. An, S. Kirm, B. Lai, R. Li, C. Silva-Acuña, J. Correa-Baena, *Adv. Mater.* **2022**, *34*, 2204726.
- [143] P. Guo, Q. Ye, C. Liu, F. Cao, X. Yang, L. Ye, W. Zhao, H. Wang, L. Li, H. Wang, *Adv. Funct. Mater.* **2020**, *30*, 2002639.
- [144] A. Weu, J. A. Kress, F. Paulus, D. Becker-Koch, V. Lami, A. A. Bakulin, Y. Yaynzo, *ACS Appl. Energy Mater.* **2019**, *2*, 1943.
- [145] X. Yi, C. H. Y. Ho, B. Gautam, L. Lei, A. H. Chowdhury, B. Bahrami, Q. Qiao, F. So, *J. Mater. Chem. C* **2020**, *8*, 16092.
- [146] R. Guo, D. Han, W. Chen, L. Dai, K. Ji, Q. Xiong, S. Li, L. K. Reb, M. A. Scheel, S. Pratap, N. Li, S. Yin, T. Xiao, S. Liang, A. L. Oechsle, C. L. Weindl, M. Schwartzkopf, H. Ebert, P. Gao, K. Wang, M. Yuan, N. C. Greenham, S. D. Stranks, S. V. Roth, R. H. Friend, P. Müller-Buschbaum, *Nat. Energy* **2021**, *6*, 977.
- [147] S. Anjusree, K. R. Arya, B. C. Das, *Roy. Soc. Chem. Adv.* **2020**, *10*, 24882.
- [148] X. Song, Y. Song, H. Xu, S. Gao, Y. Wang, J. Li, J. Hai, W. Liu, W. Zhu, *Adv. Energy Mater.* **2022**, 2203009.
- [149] D. Kim, M. Ahmadi, *ACS Appl. Mater. Interfaces* **2021**, *13*, 35133.
- [150] C. Ma, F. T. Eickemeyer, S.-H. Lee, D.-H. Kang, S. J. Kwon, M. Grätzel, N.-G. Park, *Science* **2023**, *379*, 173.
- [151] A. Mahmood, J.-L. Wang, *Sol. RRL* **2020**, *4*, 2000337.

- [152] D. Liang, C. Dong, L. Cai, Z. Su, J. Zang, C. Wang, X. Wang, Y. Zou, Y. Li, L. Chen, *Small* **2021**, *17*, 2100972.
- [153] W. Huang, F. Huang, E. Gann, Y.-B. Cheng, C. R. McNeill, *Adv. Funct. Mater.* **2015**, *25*, 5529.
- [154] S. Mukherjee, J. K. Streit, E. Gann, K. Saurabh, D. F. Sunday, A. Krishnamurthy, B. Ganapathysubramanian, L. J. Richter, R. A. Vaia, D. M. DeLongchamp, *Nat. Commun.* **2021**, *12*, 4896.
- [155] W. Zhu, G. Li, S. Mukherjee, N. E. Powers-Riggs, L. O. Jones, E. Gann, R. J. Kline, A. Herzing, J. L. Logsdon, L. Flagg, C. L. Stern, R. M. Young, K. L. Kohlstedt, G. C. Schatz, D. M. DeLongchamp, M. R. Wasielewski, F. S. Melkonyan, A. Faccetto, T. J. Marks, *Energy Environ. Sci.* **2023**, *16*, 1234.
- [156] A. Mohammed, A. Abdullah, in *Proc. of 2018 Int. Conf. on Hydraulics and Pneumatics – HERVEX*, **2018**.
- [157] M. Jiang, H.-F. Zhi, B. Zhang, C. Yang, A. Mahmood, M. Zhang, H. Y. Woo, F. Zhang, J.-L. Wang, Q. An, *ACS Energy Lett.* **2023**, *8*, 1058.
- [158] J. Hidalgo, A. Castro-Méndez, J. Correa-Baena, *Adv. Energy Mater.* **2019**, *9*, 1900444.
- [159] R. C. Masters, Q. Wan, Y. Zhang, M. Dapor, A. M. Sandu, C. Jiao, Y. Zhou, H. Zhang, D. G. Lidzey, C. Rodenburg, *Sol. Energy Mater. Sol. Cells* **2017**, *160*, 182.
- [160] P. Tyagi, T. W. David, V. D. Stoichkov, J. Kettle, *Solar Energy* **2019**, *193*, 12.
- [161] Z. Song, A. Abate, S. C. Watthage, G. K. Liyanage, A. B. Phillips, U. Steiner, M. Graetzel, M. J. Heben, in *IEEE 43rd Photovoltaic Specialists Conference (PVSC)*, IEEE, Piscataway, NJ **2016**, p. 1202.
- [162] E. J. Juarez-Perez, L. K. Ono, M. Maeda, Y. Jiang, Z. Hawash, Y. Qi, *J. Mater. Chem. A* **2018**, *6*, 9604.
- [163] T. S. Glen, N. W. Scarratt, H. Yi, A. Iraqi, T. Wang, J. Kingsley, A. R. Buckley, D. G. Lidzey, A. M. Donald, *Sol. Energy Mater. Sol. Cells* **2015**, *140*, 25.
- [164] What is Transmission Electron Microscopy? **2016**, News-Medical.net (accessed: January, 2023).
- [165] J. Zhao, X. Liu, in *Reference Module in Earth Systems and Environmental Sciences*, Elsevier, Amsterdam **2022**, p. B9780128229743000000.
- [166] J. Liu, S. Johnston, S. P. Harvey, D. Albin, P. Hacke, M. Al-Jassim, in *IEEE 7th World Conf. on Photovoltaic Energy Conversion (WCPEC) (A Joint Conference of 45th IEEE PVSC, 28th PVSEC & 34th EU PVSEC)*, IEEE, Piscataway, NJ **2018**, pp. 3281–3284.
- [167] Y. Li, W. Zhou, Y. Li, W. Huang, Z. Zhang, G. Chen, H. Wang, G.-H. Wu, N. Rolston, R. Vila, W. Chiu, Y. Cui, *Joule* **2019**, *3*, 2854.
- [168] M. Scimeca, S. Bischetti, H. K. Lamsira, R. Bonfiglio, E. Bonanno, *Eur. J. Histochem.* **2018**.
- [169] G. Divitini, S. Cacovich, F. Matteocci, L. Cinà, A. Di Carlo, C. Ducati, *Nat. Energy* **2016**, *1*, 15012.
- [170] Y. K. Penke, G. Anantharaman, J. Ramkumar, K. K. Kar, *ACS Appl. Mater. Interfaces* **2017**, *9*, 11587.
- [171] S. Zhang, L. Li, A. Kumar, in *Materials Characterization Techniques*, Chemical Rubber Company Press **2008**.
- [172] J. I. J. Choi, M. E. Khan, Z. Hawash, K. J. Kim, H. Lee, L. K. Ono, Y. Qi, Y.-H. Kim, J. Y. Park, *J. Mater. Chem. A* **2019**, *7*, 20760.
- [173] J. Kettle, Z. Ding, M. Horie, G. C. Smith, *Org. Electron.* **2016**, *39*, 222.
- [174] I. S. Zhidkov, D. W. Boukhvalov, A. F. Akbulatov, L. A. Frolova, L. D. Finkelstein, A. I. Kukharenko, S. O. Cholakh, C.-C. Chueh, P. A. Troshin, E. Z. Kurmaev, *Nano Energy* **2021**, *79*, 105421.
- [175] S. Shah, R. Biswas, T. Koschny, V. L. Dalal, in *IEEE 44th Photovoltaic Specialist Conference (PVSC)*, IEEE, Piscataway, NJ **2017**, 1350.
- [176] N. Arobi, S. M. Amir-Al Zumahi, K. Ibrahim, M. M. Rahman, M. K. Hossain, M. M. Rahman Bhuiyan, H. Kabir, A. Amri, M. A. Hossain, F. Ahmed, *J. Solid State Chem.* **2021**, *298*, 122137.
- [177] R. Kalthoum, M. Ben Bechir, A. Ben Rhaiem, M. H. Dhaou, *Opt. Mater.* **2022**, *125*, 112084.
- [178] A. Kirakosyan, M.-G. Jeon, L. Li, J. Choi, *Appl. Surf. Sci.* **2021**, *566*, 150691.
- [179] D. Yerezhep, Z. Omarova, A. Aldiyarov, A. Shinbayeva, N. Tokmoldin, *Molecules* **2023**, *28*, 1288.
- [180] Z. Guo, Z. Wu, Y. Chen, S. Wang, W. Huang, *J. Mater. Chem. C* **2022**, *10*, 13611.
- [181] Z. Yang, B. H. Babu, S. Wu, T. Liu, S. Fang, Z. Xiong, L. Han, W. Chen, *Sol. RRL* **2020**, *4*, 1900257.
- [182] B. Walker, H. Choi, J. Y. Kim, *Curr. Appl. Phys.* **2017**, *17*, 370.
- [183] J. J. Internmann, K. Yao, Y.-X. Li, H.-L. Yip, Y.-X. Xu, P.-W. Liang, C.-C. Chueh, F.-Z. Ding, X. Yang, X. Li, *Adv. Funct. Mater.* **2014**, *24*, 1465.
- [184] C. Huang, S. Shi, H. Yu, *ACS Energy Lett.* **2021**, *6*, 3464.
- [185] B. Arredondo, M. B. Martín-López, B. Romero, R. Vergaz, P. Romero-Gómez, J. Martorell, *Sol. Energy Mater. Sol. Cells* **2016**, *144*, 422.
- [186] A. F. Akbulatov, L. A. Frolova, M. P. Griffin, I. R. Gearba, A. Dolocan, D. A. Vanden Bout, S. Tsarev, E. A. Katz, A. F. Shestakov, K. J. Stevenson, P. A. Troshin, *Adv. Energy Mater.* **2017**, *7*, 1700476.
- [187] Z. Ma, R. Yu, Z. Xu, G. Wu, H. Gao, R. Wang, Y. Gong, J. Yang, Z. Tan, *Small* **2022**, *18*, 2201820.
- [188] R. He, X. Huang, M. Chee, F. Hao, P. Dong, *Carbon Energy* **2019**, *1*, 109.
- [189] X. Wen, Y. Zhang, G. Xie, R. Rausch, N. Tang, N. Zheng, L. Liu, F. Würthner, Z. Xie, *Adv. Funct. Mater.* **2022**, *32*, 2111706.
- [190] J. Ning, Y. Zhu, Z. Hu, Y. Shi, M. U. Ali, J. He, Y. He, F. Yan, S. Yang, J. Miao, H. Meng, *Adv. Funct. Mater.* **2020**, *30*, 2000837.
- [191] K. Domanski, E. A. Alharbi, A. Hagfeldt, M. Grätzel, W. Tress, *Nat. Energy* **2018**, *3*, 61.
- [192] J. Kong, S. Song, M. Yoo, G. Y. Lee, O. Kwon, J. K. Park, H. Back, G. Kim, S. H. Lee, H. Suh, K. Lee, *Nat. Commun.* **2014**, *5*, 5688.
- [193] W. Zhou, S. Chen, Y. Zhao, Q. Li, Y. Zhao, R. Fu, D. Yu, P. Gao, Q. Zhao, *Adv. Funct. Mater.* **2019**, *29*, 1809180.
- [194] H. Back, G. Kim, H. Kim, C.-Y. Nam, J. Kim, Y. R. Kim, T. Kim, B. Park, J. R. Durrant, K. Lee, *Energy Environ. Sci.* **2020**, *13*, 840.
- [195] X. Du, T. Heumueller, W. Gruber, O. Almora, A. Classen, J. Qu, F. He, T. Unruh, N. Li, C. J. Brabec, *Adv. Mater.* **2020**, *32*, 1908305.
- [196] I. M. Asuo, D. Gedamu, N. Y. Doumon, I. Ka, A. Pignolet, S. G. Cloutier, R. Nechache, *Mater. Adv.* **2020**, *1*, 1866.
- [197] G. Grancini, C. Roldán-Carmona, I. Zimmermann, E. Mosconi, X. Lee, D. Martineau, S. Narbey, F. Oswald, F. De Angelis, M. Graetzel, M. K. Nazeeruddin, *Nat. Commun.* **2017**, *8*, 15684.
- [198] H.-H. Huang, H. Tsai, R. Raja, S.-L. Lin, D. Ghosh, C.-H. Hou, J.-J. Shyue, S. Tretiak, W. Chen, K.-F. Lin, *ACS Energy Lett.* **2021**, *6*, 3376.
- [199] N. Y. Doumon, L. J. A. Koster, *Sol. RRL* **2019**, *3*, 1800301.
- [200] X. Du, X. Li, Q. Chen, H. Lin, S. Tao, *J. Phys. Conf. Ser.* **2020**, *1549*, 042015.
- [201] Y. Zhao, Z. Wu, X. Liu, Z. Zhong, R. Zhu, J. Yu, *J. Mater. Chem. C* **2021**, *9*, 13972.
- [202] A. Mahapatra, N. Parikh, P. Kumar, M. Kumar, D. Prochowicz, A. Kalam, M. M. Tavakoli, P. Yadav, *Molecules* **2020**, *25*, 2299.
- [203] M. Sajedi Alvar, P. W. M. Blom, G.-J. A. H. Wetzel, *Nat. Commun.* **2020**, *11*, 4023.
- [204] W. Yang, W. Wang, Y. Wang, R. Sun, J. Guo, H. Li, M. Shi, J. Guo, Y. Wu, T. Wang, G. Lu, C. J. Brabec, Y. Li, J. Min, *Joule* **2021**, *5*, 1209.
- [205] N. Y. Doumon, M. V. Dryzhov, F. V. Houard, V. M. Le Corre, A. Rahimi Chatri, P. Christodoulis, L. J. A. Koster, *ACS Appl. Mater. Interfaces* **2019**, *11*, 8310.
- [206] D. Bartesaghi, I. del C. Pérez, J. Kniepert, S. Roland, M. Turbiez, D. Neher, L. J. A. Koster, *Nat. Commun.* **2015**, *6*, 7083.
- [207] D. Shi, V. Adinolfi, R. Comin, M. Yuan, E. Alarousu, A. Buin, Y. Chen, S. Hoogland, A. Rothenberger, K. Katsiev, Y. Losovyj, X. Zhang,

- P. A. Dowben, O. F. Mohammed, E. H. Sargent, O. M. Bakr, *Science* **2015**, 347, 519.
- [208] M. I. Saidaminov, A. L. Abdelhady, B. Murali, E. Alarousu, V. M. Burlakov, W. Peng, I. Dursun, L. Wang, Y. He, G. Maculan, A. Goriely, T. Wu, O. F. Mohammed, O. M. Bakr, *Nat. Commun.* **2015**, 6, 7586.
- [209] L. Lee, J. Baek, K. S. Park, Y.-E. Lee, N. K. Shrestha, M. M. Sung, *Nat. Commun.* **2017**, 8, 15882.
- [210] Q. Dong, Y. Fang, Y. Shao, P. Mulligan, J. Qiu, L. Cao, J. Huang, *Science* **2015**, 347, 967.
- [211] Y.-X. Chen, Q.-Q. Ge, Y. Shi, J. Liu, D.-J. Xue, J.-Y. Ma, J. Ding, H.-J. Yan, J.-S. Hu, L.-J. Wan, *J. Am. Chem. Soc.* **2016**, 138, 16196.
- [212] V. M. Le Corre, E. A. Duijnstee, O. El Tambouli, J. M. Ball, H. J. Snaith, J. Lim, L. J. A. Koster, *ACS Energy Lett.* **2021**, 6, 1087.
- [213] E. A. Duijnstee, J. M. Ball, V. M. Le Corre, L. J. A. Koster, H. J. Snaith, J. Lim, *ACS Energy Lett.* **2020**, 5, 376.
- [214] E. A. Duijnstee, V. M. Le Corre, M. B. Johnston, L. J. A. Koster, J. Lim, H. J. Snaith, *Phys. Rev. Appl.* **2021**, 15, 014006.
- [215] H. Sun, S. Wang, S. Qi, P. Wang, R. Li, B. Shi, Q. Zhang, Q. Huang, S. Xu, Y. Zhao, X. Zhang, *Adv. Funct. Mater.* **2021**, 2213913.
- [216] Z. Song, A. Abate, S. C. Watthage, G. K. Liyanage, A. B. Phillips, U. Steiner, M. Graetzel, M. J. Heben, *Adv. Energy Mater.* **2016**, 6, 1600846.
- [217] E. von Hauff, D. Klotz, *J. Mater. Chem. C* **2022**, 10, 742.
- [218] A. Guerrero, J. Bisquert, G. Garcia-Belmonte, *Chem. Rev.* **2021**, 121, 14430.
- [219] E. Osorio, J. G. Sánchez, L. N. Acquaroli, M. Pacio, J. Ferré-Borrull, J. Pallarès, L. F. Marsal, *ACS Omega* **2017**, 2, 3091.
- [220] N. Elgrishi, K. J. Rountree, B. D. McCarthy, E. S. Rountree, T. T. Eisenhart, J. L. Dempsey, *J. Chem. Educ.* **2018**, 95, 197.
- [221] C. Yang, A. Tang, F. Teng, K. Jiang, *Acta Phys-Chim. Sin.* **2018**, 34, 1197.
- [222] M. Salerno, S. Dante, *Materials* **2018**, 11, 951.
- [223] W. Melitz, J. Shen, A. C. Kummel, S. Lee, *Surf. Sci. Rep.* **2011**, 66, 1.
- [224] E. M. Lanzoni, T. Gallet, C. Spindler, O. Ramírez, C. K. Boumenou, S. Siebentritt, A. Redinger, *Nano Energy* **2021**, 88, 106270.
- [225] J. S. Yun, J. Seidel, J. Kim, A. M. Soufiani, S. Huang, J. Lau, N. J. Jeon, S. I. Seok, M. A. Green, A. Ho-Baillie, *Adv. Energy Mater.* **2016**, 6, 1600330.
- [226] Z. Kang, H. Si, M. Shi, C. Xu, W. Fan, S. Ma, A. Kausar, Q. Liao, Z. Zhang, Y. Zhang, *Sci. China Mater.* **2019**, 62, 776.
- [227] L. Hu, Y. Jiang, L. Sun, C. Xie, F. Qin, W. Wang, Y. Zhou, *J. Phys. Chem. Lett.* **2021**, 12, 2607.
- [228] M. Azzouzi, P. Calado, A. M. Telford, F. Eisner, X. Hou, T. Kirchartz, P. R. F. Barnes, J. Nelson, *Sol. RRL* **2020**, 4, 1900581.
- [229] A. Foertig, A. Baumann, D. Rauh, V. Dyakonov, C. Deibel, *Appl. Phys. Lett.* **2009**, 95, 052104.
- [230] O. J. Sandberg, K. Tvingstedt, P. Meredith, A. Armin, *J. Phys. Chem. C* **2019**, 123, 14261.
- [231] A. Pockett, H. K. H. Lee, B. L. Coles, W. C. Tsoi, M. J. Carnie, *Nanoscale* **2019**, 11, 10872.
- [232] B. Rivkin, P. Fassl, Q. Sun, A. D. Taylor, Z. Chen, Y. Vaynzof, *ACS Omega* **2018**, 3, 10042.
- [233] J. H. Lee, I. S. Jin, Y. W. Noh, S. H. Park, J. W. Jung, *ACS Sustain. Chem. Eng.* **2019**, 7, 17661.
- [234] M. Kim, N. Ahn, D. Cheng, M. Xu, S.-Y. Ham, X. Pan, S. J. Kim, Y. Luo, D. P. Fenning, D. H. S. Tan, M. Zhang, G. Zhu, K. Jeong, M. Choi, Y. S. Meng, *ACS Energy Lett.* **2021**, 6, 3530.
- [235] Z. Dang, Y. Luo, Y. Xu, P. Gao, X.-S. Wang, *Nano Futures* **2021**, 5, 032001.
- [236] H. Sun, G. W. P. Adhyaksa, E. C. Garnett, *Adv. Energy Mater.* **2020**, 10, 2000364.
- [237] F. Babbe, C. M. Sutter-Fella, *Adv. Energy Mater.* **2020**, 10, 1903587.
- [238] A. Generosi, M. Guaragno, Q. Zhu, A. Proust, N. T. Barrett, L. Tortech, B. Paci, *Symmetry* **2020**, 12, 1240.
- [239] J.-Y. Ma, J. Ding, H.-J. Yan, D. Wang, J.-S. Hu, *ACS Appl. Mater. Interfaces* **2019**, 11, 21627.
- [240] F. Silvestri, A. Generosi, M. Guaragno, V. R. Albertini, C. Ferrero, G. Susanna, F. Brunetti, I. Davoli, B. Paci, *J. Mater. Res.* **2017**, 32, 1969.
- [241] A. M. Montgomery, N. Y. Doumon, C. Torrence, L. T. Schelhas, J. S. Stein, in *Metal Halide Perovskite Solar Modules: The Challenge of Upscaling and Commercializing this Technology*, Springer International Publishing, Cham **2023**.
- [242] R. A. Kerner, P. Schulz, J. A. Christians, S. P. Dunfield, B. Dou, L. Zhao, G. Teeter, J. J. Berry, B. P. Rand, *APL Mater.* **2019**, 7, 041103.
- [243] M. Günther, D. Blätte, A. L. Oechsle, S. S. Rivas, A. A. Yousefi Amin, P. Müller-Buschbaum, T. Bein, T. Ameri, *ACS Appl. Mater. Interfaces* **2021**, 13, 19072.
- [244] D. Li, C.-S. Chen, Y.-H. Wu, Z.-G. Zhu, W. Y. Shih, W.-H. Shih, *ACS Omega* **2020**, 5, 18013.
- [245] G. Zhang, J. Zhang, Z. Yang, Z. Pan, H. Rao, X. Zhong, *Adv. Mater.* **2022**, 34, 2206222.
- [246] K. Suchan, J. Just, P. Becker, E. L. Unger, T. Unold, *J. Mater. Chem. A* **2020**, 8, 10439.
- [247] M. M. Mandoc, F. B. Kooistra, J. C. Hummelen, B. de Boer, P. W. M. Blom, *Appl. Phys. Lett.* **2007**, 91, 263505.



Souk Yoon Kim is a Ph.D. student in the Materials Science and Engineering Department at Pennsylvania State University (Penn State), USA. He received his B. Eng. in 2020 and M. Eng. in 2022 from Pukyong National University (PKNU), Republic of Korea. He worked as a student researcher at the Korea Institute of Materials Science (KIMS). His research interests include new-generation photovoltaic materials such as organic, perovskite, and hybrid semiconductor materials and underlying device performance and degradation mechanisms.



Cyril Chu Fubin Kumachang received his B.Sc. in physics with a minor in electronics in 2017 from the University of Buea, Cameroon. In 2021, he obtained his M.Sc. in materials science and engineering from the African University of Science and Technology, Abuja-Nigeria. He is a Ph.D. student in materials science and engineering at Pennsylvania State University, USA. His research explores stability and performance issues in organic/inorganic perovskite solar cells.



Nutifafa Y. Doumon is an assistant professor at the Pennsylvania State University (Penn State). He is a Virginia S. and Philip L. Walker Faculty Fellow in materials science and engineering. He holds a Ph.D. in applied physics and an M.Sc. in nanoscience from the University of Groningen, the Netherlands. In 2011, he obtained his M.Sc. in theoretical physics from AUST-Abuja after a B.Sc. in physics in 2009 from the University of Ghana, Legon. His research interests are organic, polymer, and perovskite photovoltaic and optoelectronic device characterization, stability, and reliability testing. Before joining Penn State, he worked at the National Renewable Energy Laboratory in Golden, Colorado, USA.